Universität Stuttgart
Institut für Kernenergetik und
Energiesysteme

Improvement of Quench Front Modelling for Thermohydraulic System Codes

Christophe J. L. D‘Alessandro

Juli 2020 **IKE 2-162**

Universität Stuttgart
Institut für Kernenergetik und
Energiesysteme

Improvement of Quench Front Modelling for Thermohydraulic System Codes

von der Fakultät Energie-, Verfahrens- und Biotechnik der Universität Stuttgart zur Erlangung der Würde eines Doktor-Ingenieurs (Dr.-Ing.) genehmigte Abhandlung

vorgelegt von

Dipl.-Ing. Christophe Jean Lino D‘Alessandro

geboren in Mont-Saint-Martin, Frankreich

Hauptberichter:

Prof. Dr.-Ing. Jörg Starflinger

Mitberichter:

Prof. Dr.-Ing. Marco K. Koch

Tag der Einreichung: 02.10.2019

Tag der mündlichen Prüfung: 19.06.2020

ISSN 0173 - 6892

Juli 2020 **IKE 2-162**

Erklärung über die Eigenständigkeit

Ich versichere, dass ich die vorliegende Arbeit

„Improvement of Quench Front Modelling for Thermohydraulic System Codes"

selbstständig verfasst und keine anderen als angegebenen Quellen und Hilfsmittel benutzt habe. Fremde Quellen und Gedanken sind als solche kenntlich gemacht.

Declaration of Authorship

I hereby certify that the dissertation

„Improvement of Quench Front Modelling for Thermohydraulic System Codes"

is my own work. Ideas from other sources have been otherwise indicated clearly in the work.

In München, den 09.08.2019 Christophe D'Alessandro

Preamble

This thesis presents a further development of COCOMO-3D, code developed by the Institute of Nuclear Technology and Energy Systems (Institut für Kernenergetik und Energiesysteme, IKE), achieved in the frame of my scientist activity at the IKE between 2013 and 2018.

First of all, I'm very grateful to Prof. Dr.-Ing. Jörg Starflinger, Head of the IKE, for giving me this opportunity and also for his supervision as Doktorvater and continuous encouragements to bring this work to a happy end. I want to express my gratitude to Prof. Dr.-Ing. Marco K. Koch, Head of the group for "Plant Simulation and Safety" (PSS) at the Ruhr-University Bochum (RUB), for reviewing this thesis as second corrector and committee member at the defence, and also Univ.-Prof. Dr. Andreas Kronenburg, Head of the Institute for Combustion Technology, for being part of the examination committee as chairman. Moreover, I must thank them again as well as Ms. Maria Vencia (IKE) for their understanding and efforts regarding the organisation of the defence under the unusual circumstances related to the COVID-19 pandemic. Of course, many thanks to Dr.-Ing. Michael Buck, Head of the division of "Reactor safety and environment" at the IKE, for always providing the technical supports necessary to the completion of the present work, for sharing his deep knowledge, and most of all for giving me the chance to take part in international projects. Here, I want to thank the European Commission as well as the German Federal Ministry for Economic Affairs and Energy for supporting the CESAM and MSKRS projects respectively, and making the achievement of this thesis possible. I'd like also to thank in particular my co-workers Ailine and Corbinian for the pleasant atmosphere and funny talks we had in the office. But also, more generally, I want to greet ALL the IKE-colleagues (I cannot mention each of them here, lest I forget someone) for the great moments spent together, may they be inside or outside the IKE, which made this time of my life in Stuttgart so unique. Last but not least, I have to deeply thank my friends on either side of the Rhine, my family, and more especially my parents for supporting me as best they could, as I was going through very tough times and struggling like never before.

To conclude, it was a long but unforgettable time, which was also very instructive in many ways… as you read these lines, time is still running, but new friendships and nice memories remain.

Munich, in July 2020 Christophe D'Alessandro

Abstract

The accident of Fukushima in Japan in March 2011 highlighted the need of further research on severe accidents and on the prediction capabilities of current integral system codes. The present work deals with simulation of quenching of hot particles bed, which may form in the core from the melting and fragmentation of core components during a severe accident. The coolability of hot debris bed, still generating decay heat and threatening to re-melt, is a key-issue in terms of severe accident management. Codes that are supposed to be used as decision-making tools have to be able to calculate accident sequences quickly and accurately enough. For this reason, the computation domain is typically coarsely discretized, yielding large mesh cells (mesh size > 20 cm).

The capabilities of COCOMO-3D regarding simulations of quenching of hot debris bed is first assessed against experiments such as DEBRIS and PEARL, or by simulating the quenching of a reactor-scale debris bed, on which larger mesh cells can be generated like for integral codes. The latter simulation with large cells yields strong computation instabilities, due to the fact that two-phase cells, represented as a homogeneous water-steam mixture, are no longer representative of the real topology.

Therefore, a new method is developed in order to track and reconstruct the quench front in an unstructured meshing evolving with time. Additionally, the mass, momentum and energy conservation equations for water and steam have to be locally adapted in order to take into account the moving quench front. Moreover, the present work proposes a method to reproduce the geometry of the debris bed domain, since a coarse meshing cannot reproduce pre-defined bed geometries properly, i.e. without smearing of the boundaries.

The new modelling is verified against base cases that are analytically solvable. Finally, the capability of simulating with coarse meshing (and large cells), quickly and without any instabilities, was assessed by repeating the reactor-scale simulations.

Kurzfassung

Der Unfall von Fukushima in Japan im März 2011 hat deutlich gemacht, dass weitere Untersuchungen zu schweren Unfällen und zur Vorhersagefähigkeit aktueller integraler Systemcodes erforderlich sind. Die vorliegende Arbeit beschäftigt sich mit der Simulation des Wiederflutens eines heißen Partikelbetts, das sich im Kern durch Schmelzen und Fragmentieren von Kernstrukturen und -materialen während eines schweren Unfalls bilden kann. Die Kühlbarkeit eines heißen Schüttbetts, das immer noch Nachzerfallswärme erzeugt und es zu erneutem Aufschmelzen kommen kann, ist ein Schlüsselthema im Hinblick auf das Management schwerer Unfälle. Codes, die als Entscheidungshilfe dienen sollen, müssen in der Lage sein, Unfallfolgen schnell und genau genug zu berechnen. Aus diesem Grund wird die Berechnungsdomäne typischerweise grob diskretisiert, was große Maschenzellen (Zellengröße > 20 cm) ergibt.

Die Fähigkeiten von COCOMO-3D hinsichtlich der Simulationen des Wiederflutens eines heißen Schüttbetts werden zunächst anhand von Experimenten wie DEBRIS und PEARL oder durch Simulation des Wiederflutens eines reaktorgroßen Schüttbetts, für das größere Maschenzellen wie bei Integralcodes generiert werden können, ausgewertet. Solche Simulation mit großen Zellen führt zu starken Recheninstabilitäten, da diese Zellen, die als homogene zweiphasige Kontrollvolumina dargestellt werden, nicht mehr repräsentativ für die reale Topologie sind.

Deshalb wurde eine neue Methode entwickelt um die Quenchfront in einem zeitabhängigen unstrukturierten Netz zu verfolgen und zu rekonstruieren. Hierzu müssen die Massen-, Impuls- und Energieerhaltungsgleichungen für Wasser und Dampf lokal angepasst werden, um das Voranschreiten der Quenchfront zu berücksichtigen. Darüber hinaus wird in der vorliegenden Arbeit auch ein Verfahren zur Reproduktion der Geometrie der Schüttbettdomäne vorgeschlagen, da eine grobe Vernetzung keine vordefinierte Schüttbettgeometrie richtig reproduzieren kann, ohne die Grenzen zu verzerren. Die neue Modellierung wird gegen Basisfälle verifiziert, die analytisch lösbar sind. Abschließend wurde die Fähigkeit zur schnellen und instabilitätsfreien Simulation mit grober Vernetzung, bzw. mit großen Zellen, durch Wiederholung der Simulation des Quenchens eines reaktorgroßen Schüttbetts bewertet.

Nomenclature

a	m^2/m^3	interfacial area concentration
A	m^2	Surface area
c	m	Centroid position
c_p	J/(kg K)	isobaric heat capacity
CVF	m^3/m^3	Volume fraction of the quenched sub-cell over the whole cell
D	m	diameter
e	J/kg	specific internal energy
g	m/s^2	gravitational acceleration
h	$W/(m^2 K)$	heat transfer coefficient
i	J/kg	specific enthalpy
K	$kg/(m^3 s)$	friction coefficient
m	kg	mass
$\dot{m}$	kg/s	mass flux
$\vec{n}$	m	Normal vector
p	Pa	pressure
P	W/kg	Power density
$\dot{q}$	W/kg	specific power
Q	W/m^3	heat flux density
r	m	radial coordinate
R	m	radius
s	m^3/m^3	saturation, fraction of fluid in porous space
S	m^2	surface
t	s	time

T	K	temperature
$\vec{u}$	m/s	- orthogonal structured meshing: x-component of the velocity $\vec{w}$ - unstructured meshing: velocity component normal to the surface
$\vec{v}$	m/s	- orthogonal structured meshing: z-component of the velocity $\vec{w}$ - unstructured meshing: velocity component tangent to the surface (also denoted $\vec{ut}$)
V	m^3	volume
$\vec{w}$	m/s	velocity
x	m	x-coordinate
z	m	z or axial coordinate

Greek symbols

ε	m^3/m^3	porosity
Γ	$kg/(m^3\ s)$	mass transfer rate, evaporation rate
η	Pa s	dynamic viscosity
κ	m^2	permeability
λ	W/(mK)	heat conductivity
μ	m	passability
ρ	kg/m^3	density
σ	N/m	surface tension

Indices

A	annular flow regime
b	boundary
B	bubble, bubbly
BST	bubbly / slug transition

c	capillary
cond	conduction
conv	convection
dn	quenched lower sub-cell (“down”)
eff	effective
evap	evaporation
f	face
FB	film boiling
g	gas
GC	gas continuous regime
HB	high void bubbly flow regime
i	Radial index in *structured* meshing, or spatial index in *unstructured* meshing
ini	initial
j	Axial index in *structured* meshing
k	Phase k (gas, liquid or solid)
l	liquid
LB	low void bubbly flow regime
LC	liquid continuous regime
LGT	liquid / gas transition
lam	laminar
mo	momentum
NB	nucleate boiling
old	Previous time step
P	particles

QF	quench front
rel	relative
sat	saturation, gas/liquid interface
s	solid, particles
S	slug flow
SAT	slug / annular transition
trans	transition
turb	turbulent
up	upper sub-cell unquenched

Mathematical symbols

∂	partial derivative
Δ	difference
∇	Nabla operator, gradient or divergence
$\vec{\cdot}$	Vector

Dimensionless numbers

Ja	Jacob number, $\mathrm{Ja} = \frac{c_P \cdot \Delta T}{\Delta i}$
Nu	Nusselt number, $\mathrm{Nu} = \frac{h \cdot D}{\lambda}$
Pr	Prandtl number, $\mathrm{Pr} = \frac{\eta \cdot c_P}{\lambda}$
Re	Reynolds number, $\mathrm{Re} = \frac{w \cdot \rho \cdot D}{\eta}$

Table of figures

figure 1 : (a) loss of geometry integrity, (b) in-core molten pool formation, (c) in-vessel debris bed formation 4
figure 2 : ex-vessel debris bed formation 5
figure 3 : (a) in-core debris bed, (b) melting of debris 6
figure 4 : ASTEC simulation of KONVOI core degradation: (left) core during dewatering, (right) core uncovered, heat-up of fuel rods 13
figure 5 : overview of the present work structure 16
figure 6 : axial temperature and heat flux profiles along the debris bed during quenching - boiling regimes defined in COCOMO-3D 27
figure 7 : structured staggered grid of the standard version of COCOMO-3D 29
figure 8 : unstructured meshing obtained from the structured grid (figure 7) 32
figure 9 : definition of the normal vector of the face common to two cells and projected distance between two centroids 33
figure 10 : resolution pattern of the current version of COCOMO-3D 38
figure 11 : representation of the different zones of the quench region, for a dry particle bed flooded from the bottom (referring to [51]); s_g being the void fraction in pores 40
figure 12 : DEBRIS test facility (from [45]) 41
figure 13 : DEBRIS quench-test, with bottom gravity-driven injection 42
figure 14 : axial quench front progression in DEBRIS (Tini = 400°c; gravity-driven injection) 44
figure 15 : axial quench front progression in DEBRIS (Tini = 400°c; fixed injection) 45
figure 16 : gas pressure in debris bed at elevation 320 mm (Tini = 400°c; fixed injection) 46
figure 17 : mass of steam generated over the whole quenching (Tini = 400°c; fixed injection) 46
figure 18 : gas pressure in debris bed at elevation 320 mm (Tini = 400°c; gravity-driven injection) 47
figure 19 : mass of steam generated over the whole quenching (Tini = 400°c; gravity-driven injection) 48
figure 20 : mass of water injected over the whole quenching (Tini = 400°c; gravity-driven injection) 48
figure 21: schematic view of the PEARL facility 49
figure 22 : set-up of heat-up, bed temperature and water injection 50
figure 23 : quench front progression in PEARL PA-2 test and with COCOMO 52
figure 24 : quench front progression calculated by COCOMO, for case PA-0, PA-1, PA-4 and PA-5 (fine meshing) 53
figure 25 : reflooding time vs. initial temperature (constant injection rate) 54
figure 26 : reflooding time vs. injection rate (constant initial temperature) 54
figure 27 : quench front progression calculated by COCOMO for cases PA-0, PA-1, PA-4 and PA-5 (coarse meshing) 55

figure 28 : quench front progression and generated mass of steam obtained with different axial discretizations 56
figure 29 : mass of water injected over the whole quenching (gravity-driven injection) 57
figure 30 : (a) quench front progression and (b) generated mass of steam obtained with 6 and 90 cells for porosities of 30%, 40% and 45% 58
figure 31 : (a) quench front progression and (b) generated mass of steam obtained with 6 and 90 cells for particle sizes of 2.0, 2.9 and 5.0 mm 59
figure 32 : (a) quench front progression and (b) generated mass of steam obtained with 6 and 90 cells for system pressures of 1, 3 and 5 bar 59
figure 33 : (a) quench front progression and (b) generated mass of steam obtained with 6 and 90 cells for debris bed height of 1.5, 2.0 and 3.0 m 60
figure 34 : two-phase flow representation in current COCOMO-3D meshing vs. reality 60
figure 35 : cell liquid fraction vs. (a) pressure vs. (b) liquid velocity for coarse meshing 61
figure 36 : cell liquid fraction vs. (a) pressure vs. (b) liquid velocity for fine meshing 62
figure 37 : dimensions and positions of the studied cells (studied cells in grey) 63
figure 38 : modelling of a conical debris bed in COCOMO-3D (yellow line: user-defined geometry) 65
figure 39: 2D-example of cells intersected by the bed boundaries 68
figure 40 : process of bed boundary reconstruction 68
figure 41 : reconstruction of an heap-like bed in COCOMO-3D (left: vertical section through the centre of bed; right: horizontal section at the base of bed) 69
figure 42 : illustration of (a) piecewise constant and (b) stair-stepped methods 70
figure 43 : illustrations of (a) plic reconstruction and (b) its resulting discontinuities 71
figure 44 : illustration of (a) isosurface and (b) equisurface reconstructions 72
figure 45 : illustration of the isotherm reconstruction method 72
figure 46 : temperature gradient at the interface by using the isotherm reconstruction method 73
figure 47 : standard isosurface reconstruction vs. current reconstruction method 75
figure 48 : procedure of the quench front reconstruction 76
figure 49 : control volume with moving boundary 78
figure 50 : quadrilateral grid cell at two successive time points 79
figure 51 : volume swept by the quench front during Δt and the associated velocities 80
figure 52 : pressure gradient at the quench front 83
figure 53 : illustration of 1D sub-cell / cell merging 94
figure 54 : illustration of 2D merging sub-cell / next neighbour cell 94
figure 55 : resolution pattern of the revised version of COCOMO-3D 97
figure 56 : 1D simulation of flooding of a 2 m-high debris bed (injection: 2 kg/s) 100
figure 57 : progression and velocity of the reconstructed quench front (m_{inj} = 2 kg/s) 101
figure 58 : progression and velocity of the reconstructed quench front (m_{inj} = 5 kg/s) 101
figure 59 : progression and velocity of the reconstructed quench front (hydrostatic head = 2.0 m) 103

figure 60 : progression and velocity of the reconstructed quench front (hydrostatic head = 5.0 m) 103
figure 61 : progression and velocity of the reconstructed quench front (T_s^0 = 700 K).....107
figure 62 : progression and velocity of the reconstructed quench front (T_s^0 = 1500 K).....107
figure 63 : visualisation of 1D liquid fraction distribution (left) and temperature profile (right) at the end of the quenching of a 700 K debris bed.....108
figure 64 : visualisation of 1D liquid fraction distribution (left) and temperature profile(right), during the quenching of a reactor-scale debris bed 109
figure 65 : progression of the reconstructed quench front and associated steam generation in reactor-scale debris bed (hydrostatic head = 6.0 m) 110
figure 66 : pressure evolution during the quenching at different elevations, with the new (left) and old (right) COCOMO-3D 111
figure 67 : mass of water injected over the whole quenching in reactor-scale debris bed (hydrostatic head = 6.0 m) 112
figure 68 : (left) quench front progression and (right) generated mass of steam obtained with 3 and 60 cells for system pressures of 1 bar, 3 bar and 5 bar, with the new modelling.....113
figure 69 : (left) quench front progression and (right) generated mass of steam obtained with 3 and 60 cells for porosities of 30%, 40% and 45%, with the new modelling 113
figure 70 : progression of the reconstructed quench front in reactor-scale debris bed (hydrostatic head = 3.0 m) 114
figure 71 : velocities on orthogonal structured grid (radial) 126
figure 72 : velocities on orthogonal structured grid (axial).....127
figure 73 : velocities on unstructured grid.....128
figure 74 : axial quench front progression in debris (gravity-driven injection) 139
figure 75 : gas pressure in debris bed at elevation 320 mm (gravity-driven injection).....139
figure 76 : mass of steam generated over the whole quenching (gravity-driven injection) 139
figure 77 : averaging of the variable ψ at a node (yellow point) on a uniform orthogonal grid ..140
figure 78 : averaging of the variable ψ at a node (yellow point) on an irregular grid.....141

Table of contents

1 Introduction 1
1.1 Research on reactor safety 2
1.1.1 Phenomenology 3
1.1.2 Experimental programs 7
1.1.3 Severe accident codes 11
1.2 Objectives 14
2 COCOMO-3D Modelling 17
2.1 General 17
2.2 Modelling 18
2.2.1 Mass conservation 19
2.2.2 Momentum conservation 19
2.2.3 Energy balance 24
2.3 Discretization 28
2.3.1 Structured meshing (standard) 28
2.3.2 Unstructured meshing 31
2.4 Resolution scheme 35
3 Validation 39
3.1 Quench front definition 39
3.2 Simulation of DEBRIS 40
3.2.1 DEBRIS test facility 40
3.2.2 Reproduction of DEBRIS with COCOMO-3D 43
3.2.3 Simulation results 43
3.2.4 Sensitivity analysis regarding the meshing of the debris bed domain 44
3.3 Simulations of the PEARL experiments 48
3.3.1 PEARL facility 49
3.3.2 Test conduct 49
3.3.3 COCOMO-3D input 50
3.3.4 PEARL vs. COCOMO results 51
3.4 Simulation of reactor-scale debris bed 56
3.5 Identification of the problem 60
4 New models for reconstruction of bed geometry and quench front 67

4.1 General 67
4.2 Debris bed reconstruction 67
4.3 Quench front reconstruction 70
4.3.1 Existing tracking methods 70
4.3.2 Quench front tracking 74
4.4 Adaptation of conservation laws with respect to moving boundaries 77
4.4.1 Spatial conservation law 77
4.4.2 Formulation of the quench front velocity 79
4.4.3 Resolution of the momentum conservation equations at the quench front 82
4.4.4 Determination of the new grid geometry 86
4.4.5 Modification of conservation equations to take into account moving cell faces 87
4.4.6 Resolution of the conservation equation system 91
4.5 The new general algorithm 92
4.5.1 Initialization of the grid 92
4.5.2 Resolution pattern 95
5 Applications 98
5.1 Model verification 99
5.1.1 Quench front progression by constant bottom-flooding 99
5.1.2 Quench front progression by gravity-driven injection 101
5.1.3 Quenching of hot debris bed and steam generation 104
5.2 Reactor scale 108
6 Conclusion 115
7 References 118
8 Appendices 125

1 Introduction

Worldwide, approximately 2441 TWh of electrical energy is produced by nuclear power plants (NPP), representing about 14% of the global electric energy production. In overall 448 reactors can be inventoried in the world. To this day, France is the country that relies the most on nuclear energy, with 58 reactors, generating 71.6% of its whole electricity production (in 2017) [1]. The reason of this particular interest for nuclear technology in energy production is namely that nuclear energy can be considered as sustainable and clean. Indeed, compared to fossil energy (i.e. coal, petroleum and natural gas), it requires a small amount of fuel to generate a huge amount of thermal (and then electrical) energy, that is CO_2-free. Despite all the advantages regarding the environment and production costs, the further use of nuclear energy is still contested due to the potential risk of severe accident in nuclear reactors and also its impact on the environment and the population. Concerns from the public about nuclear energy came mostly from the accidents of Three Mile Island (1979) [2] and Chernobyl (1986) [3]. These accidents revealed weaknesses of the emergency system and a lack of knowledge as for the counter-measures to adopt. As a response, research campaigns were launched in order to understand better the main phenomena occurring during an accident. Finally the accident of Fukushima Daiichi (2011) [4] highlighted the need for clear emergency measures and reopened the discussion on the thread of nuclear energy. For this reason, reactor safety and severe accident management are of main importance. Although emergency measures were designed in order to prevent a severe accident, a 0%-risk of accident can never be ensured. Hence, parallel to prevention measures, severe accidents must be investigated in order to propose mitigation measures. In the critical case the core cannot be sufficiently cooled anymore, the final aim is to stop the progression of the accident and therefore to limit the release of radioactive source terms in the environment.

In order to minimize the risk of accident and its impact, nuclear power plants are designed following the Defense-in-depth philosophy [5]. This principle can be categorized into five levels. The first three levels aim the normal operating state of plant, by a reliable and robust installation, as well as prevention of accidents, by regulation and control systems, ensuring a sufficient heat removal in order to protect the core integrity. If an accident is initiated in spite of all the

emergency measures, the reactor is automatically shut down by inserting absorber rods in the core. However, fission products in the rods are still generating decay heat that must be evacuated by a constant water supply in order to avoid a core heat-up. This is ensured by the reactor core cooling system (RCS). In the very unlikely case of a RCS failure, due to unforeseen events for which the plant was not designed, the core can quickly heat up and be damaged. In that case, prevention measures are of no more use. It is then commonly referred to a "beyond design basis accident" (BDBA). Henceforth, one has to follow the two last levels of the defence-in-depth, consisting in counter-measures to prevent, or mitigate, (if prevention is also no longer possible) any fission products release into the environment. To achieve this the integrity of the three confinement barriers (rods, primary circuit and containment) must be kept intact. The barriers are namely threatened by the heat-up of the fuel rod, the mass of molten material (corium) in the reactor pressure vessel (RPV) which can damage the vessel, and also by the presence of hydrogen, which can explode at any time. In order to choose the adequate counter-measures, one must refer to the Severe Accident Management Guidelines (SAMGs), which have been updated in Germany since the Fukushima accident [6,7].

1.1 Research on reactor safety

The nuclear accidents highlighted the need for a better understanding of the phenomena that may occur in a BDBA. Unlike in design basis accidents (DBA), where operators must basically refer to the foreseen emergency procedures proper to each NPP type, BDBA are far more complex, since not only thermo-hydraulics, but also mechanical and chemical phenomena have to be considered at the same time. It makes the course of the accidents as well as the impact of operator actions hard to predict. Computer codes are used in order to improve the SAMGs by analysing the effectiveness of cooling measures and all the processes that may happen during the core degradation up to its aftermath. However, reliable predictions require a very sound description of each physical process. For this purpose, the main processes (heat transfers, oxidation, free convection in molten material, rod deformation, etc.) were identified and were separately investigated through various experimental programs worldwide, in order to find out correlations being able to simulate every aspect of core degradation. Nevertheless, some complex phenomena

are currently still not fully understood, or not satisfactory modelled in codes and are still under study; such as the modelling of two-phase flow in a severely degraded core (bed of particles), which is the topic of the present work.

Before going into more details about actual code issues, the different phases of a severe accident and their corresponding phenomena must be explained. More details can be found in reference books [6,8]. A severe accident results namely from a strong loss of coolant (LOCA: loss of coolant accident) in the primary side, for instance due to a leakage in the circuit. The lack of cold water lead to core heat-up, that can accelerate the evaporation and after a certain time begins to uncover the reactor.

1.1.1 Phenomenology

The generated steam can oxidize the uncovered part of the fuel cladding made of Zircaloy (Zirconium alloy). This chemical reaction generates hydrogen. Of course, the oxidation rate is strongly dependent on the composition of zirconium alloy and on the temperature. Since oxidation is an exothermal reaction, it contributes also to the heat-up of the core. Moreover, the oxidation rate increases with the temperature. Once the core temperature exceeds 1500 K, the heat-up due to the accelerating oxidation process becomes considerable (generated heat from oxidation can even be as high as three times the decay heat, once the cladding temperature reaches 1800 K) [6], until the cladding starts melting (melting temperature ~ 2100 K) [9,10]. Typical control rods in pressurized water reactors (PWR), made of AIC (silver, indium and cadmium), start melting at lower temperatures (at around 1100 K), but are enclosed in steel cladding, which are themselves contained in Zircaloy guiding tubes. The melting of the two latter structures occurs by 1500 K as steel and Zircaloy interact into a eutectic melt. After the loss of integrity of the guide tube and the cladding, the eutectic melt may interact with the molten absorber material [11]. As for boiling water reactors (BWR), B_4C-control blades melt at higher temperatures (around 2700 K), but undergo interaction with steel cladding already at lower temperatures like for PWR absorber rods. Depending on the control rod materials and its cladding, hydrogen may also be released by their oxidation. Besides molten control rod material (typically in top region of the core) can relocate by candling in lower colder region and solidify;

nevertheless eutectic reaction can also take place when entering in contact with fuel cladding [12], like already mentioned above. This eutectic reaction may change locally the physical properties of the cladding, such as its melting temperature. The fuel itself UO_2 starts melting at 3100 K, though it can melt earlier, at lower temperature, if its melting temperature changes due to a eutectic reaction with the Zircaloy cladding [13]. In addition, the fuel tubes undergo strong mechanical stresses: on one hand the thermal expansion of cladding makes the tube fragile, and on the other hand the overpressure inside the tube due to the fission gas leads to a so-called ballooning of the tube (see Figure 1 (a)). Under this mechanical deformation, tubes may creep already at low temperature (at around 1000 K) [6].

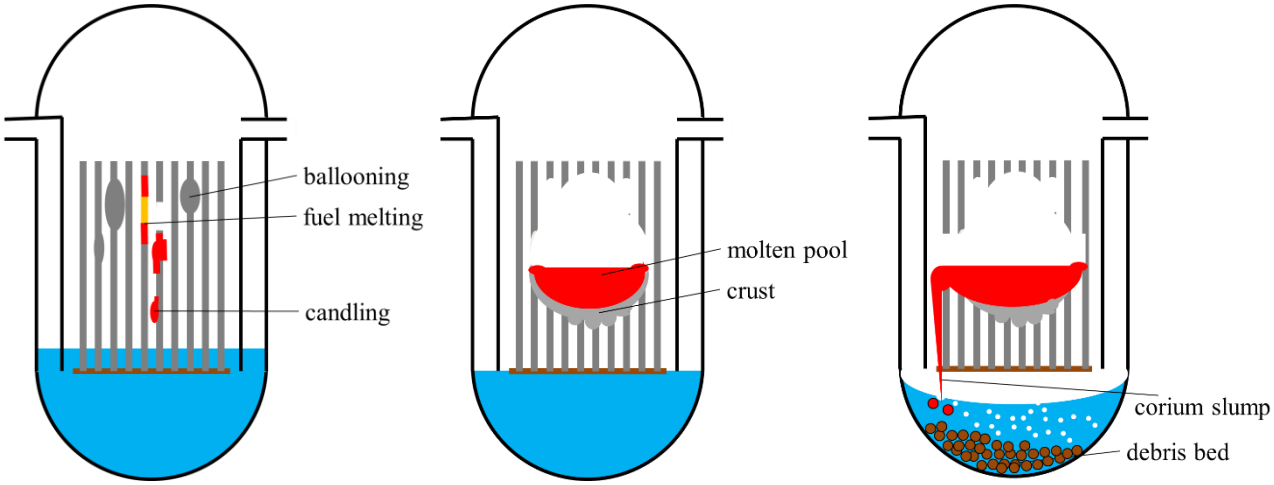

Figure 1 : (a) Loss of geometry integrity, (b) In-core molten pool formation, (c) In-vessel debris bed formation

The molten mixture resulting from the melting of the core components and structures is commonly called 'corium'. Corium contains mainly UO_2 (fuel), Zr and ZrO_2 (tubes) as well as stainless steel (from structures). The precise composition of corium depends strongly on the course of the accident and on the reactor type. Like mentioned above, corium relocates downwards in colder regions, where it can solidify again. This re-solidified material may form some blockages, preventing water to access and cool degraded regions. Moreover the accumulation of corium on the solidified crust can form a molten pool in the core regions (see Figure 1 (b)), hardly coolable because of its very high temperature and its surface/volume ratio [6]. In addition corium may also fragment into small particles when interacting with water [6]

(residual or injected water). Packed together, the settled particles form a so-called “debris bed”, which can be considered as a solid porous region. Later on corium slumps into the lower plenum (see Figure 1 (c)) and can fragment again into debris because of residual water [14]. Fission products still generate decay heat inside particles. If the decay heat in the debris bed is not sufficiently removed, the debris may heat up and re-melt, forming a new molten pool, jeopardizing the vessel lower head [15]. Lower head rupture occurs either by erosion of the vessel wall by hot corium, or also by mechanical deformation due to the mass of corium and the primary circuit pressure [6]. In some reactor the in-vessel melt retention (IVMR) concept is applied [16] (for example, in the Westinghouse concept AP600 and AP1000), where the vessel lower head is immersed into a flooded cavity, ensuring an external cooling of the vessel wall.

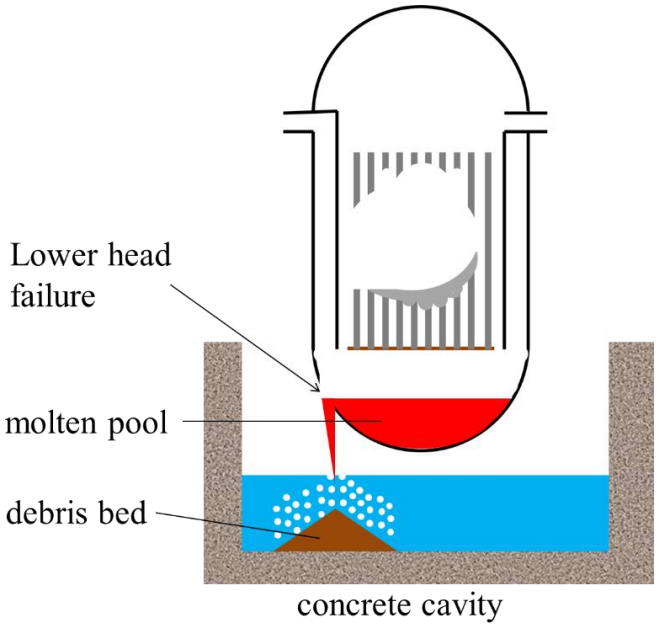

Figure 2 : Ex-vessel debris bed formation

As the RPV fails, molten material slumps into the cavity and attacks cavity concrete (Molten Core Concrete Interaction: MCCI) [6]. This interaction weakens the cavity and can besides generate incondensable gases that are then released in the containment; some of them are a real hazard for the NPP, such as hydrogen. In some NPPs, the safety guidelines recommend to flood the cavity, so that the slumping corium fragment into particles and form a debris bed in the cavity, as depicted on Figure 2; much easier to cool than a molten pool. Depending on the depth of the water pool in the cavity, the size of the corium jet and its temperature [14,17], the debris

bed will have different geometries and particle size repartition. Another concept to deal with ex-vessel molten material is the core catcher [18] planned for the EPR in Flamanville, France. Basically, the molten material does not slump into the above mentioned cavity, but along a channel towards a chamber, where it will spread, changing its surface/volume ratio. The corium flow turns into a thin film in the core catcher, more favourable for cooling. In the COMET concept [19], the bottom of cavity consists of a concrete sacrificial layer. Once this layer is eroded by molten material, cold water is released from the bottom through channels under the sacrificial layer. The upwards water ingression from the bottom provokes corium solidification and debris formation.

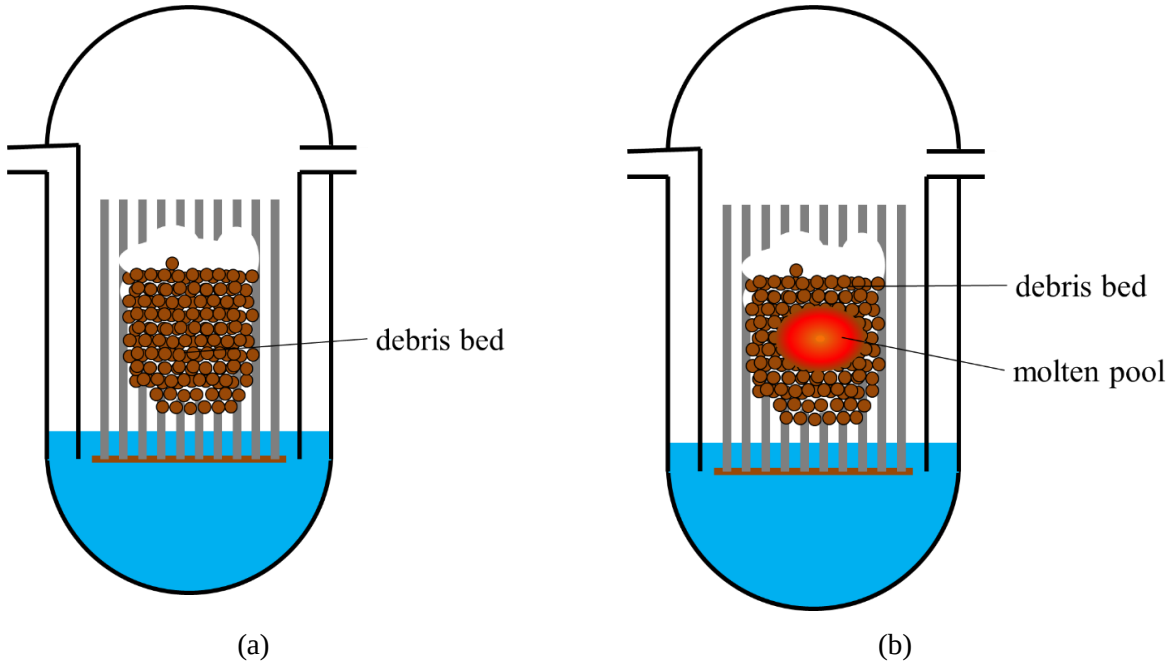

Figure 3 : (a) In-core debris bed, (b) Melting of debris

As already mentioned, water injection remains one of the main mitigation measures. Though a late injection may induce further oxidation from the instantaneously evaporated water, this measure is advantageous in general. The more intact the core geometry, the higher the success of the reflooding and the chance to stop the progression of the accident. The different flow regimes occurring during reflooding has been already well-investigated for intact and slightly degraded cores, namely by Ishii, De Jarlais and Obot [20–22]. The coolability is then mostly influenced by the degradation state of the core, the rod temperature (resulting from the decay heat) and the water injection rate and position [23]. On the other hand, if cool water is supplied at a relatively

early stage regarding the degradation state (before any formation of molten pool), molten material may fragment into particulate debris, as well as some hot solid structures due to thermal shock. These particles have to be cooled down to prevent their re-melting and the formation of a molten pool within the debris bed itself, as depicted on Figure 3. Therefore, the coolability of debris beds is a key-issue still under research, for it depends on many parameters such as the bed geometry, the particles size or even the injection position. The next section is dedicated to the experiments related to the debris bed issue.

1.1.2 Experimental programs

While the present work will focus more on the simulation of hot debris bed quenching, it is still worth to give an overview of the different studies on debris bed formation, since the geometry as well as the particle size and form are decisive parameters in terms of coolability. Main outcomes from experiments on debris bed coolability are summarized afterwards.

During the last decades corium jet fragmentation and debris settling were strongly investigated. Particle size and form play a major role on the local porosity, and thus on the flow behaviour. Moreover, corium is not necessarily totally fragmented when slumping into water, and very hot particles may re-melt locally and consolidate, yielding some compact and impervious zones. All these aspects have to be considered when analysing the coolability of a particle bed.

Corium fragmentation was namely investigated under variation of different parameters (pressure, water depth, water temperature, molten material mass etc.) by Magallon [14] in FARO and KROTOS test facilities. It was observed that compact agglomerations (impervious zones, already mentioned above, called ‘cake’) were formed, when the water depth was smaller than the break-up length of the melt jet (i.e. the melt jet has not enough time to fragment entirely). The cake is generally covered by debris. Particle size repartition was also analysed: average sizes were in the range 2.6 – 4.8 mm. Moreover, steam explosion could have also been observed, but only in one test (test L-33). Molten jet break-up was also experimented by Spencer et al. in the CCM-2 – CCM-6 [17] test facilities. These tests address the chemical processes as well as the particle size

repartition like in the previous experiments; but additionally, porosity was also measured, and was in the range 0.39 – 0.65.

The PREMIX experiments [24] performed by FZK reproduced similar tests to FARO, except that simulant was used for molten material (Al_2O_3). Like in FARO, a cake was formed. Some of the Al_2O_3 debris created in PREMIX were then used at the University of Stuttgart, namely in the DEBRIS facility [25] to assess the cooling behaviour with such particles.

The DEFOR facility [26] was designed to study the phenomena involved in the formation of debris beds during the release of melt in water pools. The principle of the experiment is similar to FARO, except that simulant materials with lower melting temperature were used and that the experiments were carried out at ambient pressure. Here was also concluded that the chances that the debris reach the bed in a liquid state is higher as the depth of the pool decreases. But even so, the resulting intense evaporation led to a better homogenization of the debris and to melt spreading over the floor, thus yielding a larger settling area.

Regarding the debris bed coolability, two kinds of experiments were carried out: dryout investigation in a water-filled debris bed, and analysis of the quenching of a hot dry debris bed.

Dryout is mainly related to long-term cooling of a water-filled debris bed, which generates decay heat. The major issue here is to evaluate the dryout heat flux (DHF), which is the maximum heat flux that can be removed under steady state conditions from the debris bed, without apparition of any dry spot inside the bed. If the generated heat flux exceeds the maximal removable heat flux, then zones inside the bed will dry up. These dry zones may heat up and re-melt later on. The DHF depends on several parameters, such as the water injection configuration, the porosity, the particles diameter, the pressure.

From Hofmann [27,28], Atkhen and Berthoud [29], and Rashid [30], it was found that the DHF obtained by bottom injection (gravity-driven; from a water column as high as the bed) was typically more than twice higher than by top-injection, since top-flooding yields a counter-current flow; the generated steam flows upwards, against the water flow, reducing water ingression into the bed, which lead to dryout when no water can ingress anymore.

Thakre et al. [31] investigated several bed configurations under different injection conditions. It came out that multidimensional bed geometries, such as heap-like bed, improve the coolability because of the lateral flows.

In STYX test (from Lindholm et al. [32]) and DEBRIS (Rashid et al. [25], Kulkarni et al [33]) were used debris with irregular shaped, which can be considered as more realistic. These particles were first produced and provided by fuel-coolant interaction experiments (based on FARO for STYX, particles from PREMIX for DEBRIS). Outcomes of STYX were namely used to determine which averaging method is the most appropriate to calculate the effective diameter of debris for a locally well-mixed bed with particles of different sizes. It was concluded that the best results are obtained between "number density"-weighted and "surface area"-weighted average diameter (see Appendix-A). With DEBRIS, tests on boiling and dryout were carried out by varying the particle bed inventory, the system pressure and the injection modus (Schäfer et al. [34,35]). Boiling tests were used to assess interfacial friction model inside the bed. Dryout tests were processed with monodispersed beds as well as with polydispersed beds, and also with several injection conditions (top- or/and bottom-flooding, or via a central perforated downcomer). After a further technical development of the DEBRIS facility, Leininger [36–38] analysed into more details the physical processes and the influence of boundary conditions on DHF, and showed namely that the porosity plays a significant role on the coolability. The lower the porosity, the higher the pressure gradient, which reduces the mass flow rates and so the coolability. For top-flooding, it was noticed that the dryout starts at the top of the bed and then propagates downwards. As for the bottom-flooding configuration, the dryout could be observed at the bottom of the bed, as soon as the evaporation rate exceeds the water injection rate.

In the COOLOCE experiment Takasuo et al. [39,40] investigated the influence of the geometry and of multidimensional inflow upon the coolability. For this purpose, two different geometries were considered: conical and cylindrical (evenly distributed, purely top-flooded). For the same bed height, the conical bed showed a better coolability than the cylindrical bed, due to the surface of the cylindrical bed open to lateral infiltration. However, for a same diameter and volume, the cylindrical bed (consequently smaller than the conical bed) presented a better coolability, meaning that the bed height plays a role on the coolability but also may compensate the positive effect of lateral water ingression.

Coolability of hot and dry debris beds depends on the parameters mentioned above, but also on the initial temperature of the particles. The quenching tests focus mainly on “if” and “how fast” debris bed can be fully flooded and cooled down to saturation conditions before it has any chance to heat up. Many experiments were dedicated to that issue.

Valuable data on progression of quench front and the subsequent steam production were already obtained by Tutu et al. [41]; a constant mass rate of cold water was injected from the bottom. A major finding was the heat flux profile in the quench region with respect to the injection mass rate. A slow injection yields a thin quench region, and thus a plateau-like axial heat flux profile; while a larger mass rate provokes a thicker quench region, and thus peaks in the axial heat flux profile. Similar observations were made in the PRELUDE experiments (Repetto et al. [42,43]) performed by IRSN (Institut de Radioprotection et de Sûreté Nucléaire); which assumed that it was due to multidimensional effects.

More recently IRSN designed the PEARL facility [44], enabling quenching tests at larger scale and checked the impact of a by-pass surrounding the particle bed upon the liquid and gas flow patterns. The quenching was observed for different initial bed temperatures, injection rates (from the bottom) and pressures. Like in previous experiments the reflooding time seems to be proportional to the initial bed temperature, but tends to decrease with higher injection velocity up to a lower limit. This is due to a limitation of the pressure gradient inside the main bed, because of the presence of the by-pass. Indeed, steam tends to drag water into the by-pass, limiting the cooling of the bed.

However, most of these experiments were achieved with a fix injection rate. In reactor case, water accesses the degraded core region, i.e. debris bed, by the water collector (downcomer). In other words, the water flow is not really determined by the pump rate, but rather by the hydrostatic head of the water column in the downcomer. Quenching process of a hot cylindrical debris bed by a lateral water column was addressed in the DEBRIS experiments (Rashid et al. [45]). The injection being gravity-driven, the water inflow is determined not only by the hydrostatic head but also by the feedback of the phenomena occurring within the bed during the quenching, i.e. the pressure build-up due to friction with water and steam, as well as between the phases themselves. Like for fixed injection rates, it was observed that the higher the initial particles temperature is the slower the quench front progresses through the bed. Leininger [46]

performed tests on the DEBRIS facility (though with different debris sorts) at several system pressures, and came to the conclusion that the higher the pressure is the slower the quench front progresses.

Tung and Dhir [47] have investigated the quenching behaviour in radially and axially stratified beds (layers with different porosities) by bottom or top-flooding. In case of top-flooding the quenching process is governed by steam friction (steam flows upwards against water). The quenching may last longer, if a layer with a lower permeability lays on the bed. Under top-flooding conditions, it was also noticed that water flowed downwards faster near the wall because in that region the permeability may be larger (so-called “wall effect”). Moreover, this behaviour was confirmed in the test with radial stratification.

Top-flooding was also investigated by Schäfer et al. [34]. It came out that the quench front reached the bottom of the bed through individual flow streaks (path where water could easily ingress; due to a local lower temperature or a larger permeability, etc.), which was also observed in some experiments of Ginsberg [48] and Cho et al [49,50] in the 80’s. Once the water reached the bottom, a quench front may progress upwards to cool the remaining superheated regions. This phenomenon was also observed and analysed into more details in DEBRIS by Leininger [51], where the injected water flowing downwards though streaks formed a water pool at the bottom. The level of the pool continuously raised, cooling the remaining hot regions of the bed. The dissipated heat flux density from the top-flooding quenching was in good agreement with the one already found in the frame of the dryout test. Like for bottom-quenching, the reflooding time appeared to be proportional to the initial bed temperature, but is of course longer than for bottom-quenching, due to the resulting counter-current flow configuration (occurring between steam and liquid).

1.1.3 Severe accident codes

In order to develop SAMGs, numerical tools are very valuable. Experiments, such as the ones presented above, provide a useful database to support the modelling of these severe accident codes. From experimental data, new empirical correlations can be established, and the already

implemented models can also be validated separately. In order to perform reliable risk analyses, codes must first be capable of giving good predictions of accident sequences. Hence, codes must be thoroughly assessed. However, risk-analysis and SAMGs development are not the only applications. Some codes are foreseen to be used as computational aid for operators, namely as decision-making tools in emergency cases. As a matter of fact, these codes are supposed to be accurate enough, but also reasonably simplified in order to carry out fast calculations. They should predict the events before they actually happen in the reality. It usually requires also a coarse discretization of the reactor domain.

Two categories of severe accident codes must be distinguished. From one side, integral codes simulate the whole nuclear power plant and are able to compute a whole accident sequence from its initiation till source term release into the environment. However, the representation of all the relevant physical phenomena (in-vessel, ex-vessel and in containment) has to be simplified. From the other side, separate effect codes focus only on specific phenomena or group of correlated phenomena; moreover, these codes are often coupled with integral codes as modules.

The French-German integral code ASTEC (Accident Source Term Evaluation Code) is the European reference for severe accident simulation [52]. It is jointly developed by IRSN and GRS (Gesellschaft für Anlagen- und Reaktorsicherheit), and lately assessed and improved by several European partners in the frame of the CESAM project [53]. ASTEC has a modular structure. Each module, which can also be run in stand-alone modus, addresses a specific part (and its associated phenomena) of the NPP, such as the reactor pressure vessel, the primary and secondary circuits, the containment, and so on. One of these modules, ICARE, developed as part of the stand-alone code ICARE-CATHARE (IRSN, France), is dedicated to the processes occurring in the reactor vessel during the normal operating state as well as core degradation till vessel failure. ASTEC was designed in order to perform SAMGs analysis, like lately in the work of Gómez-García-Toraño [54], but also emergency calculations. For this kind of computations, a coarse discretization of the core domain is generated (cell size typically ~ 20 cm) [54,55]. For instance, Figure 4 shows a typical visualization of a KONVOI-reactor input reproduced with ASTEC. The 3.9 m-high core has been discretized into approximately 10 cells axially (cell size ~ 40 cm).

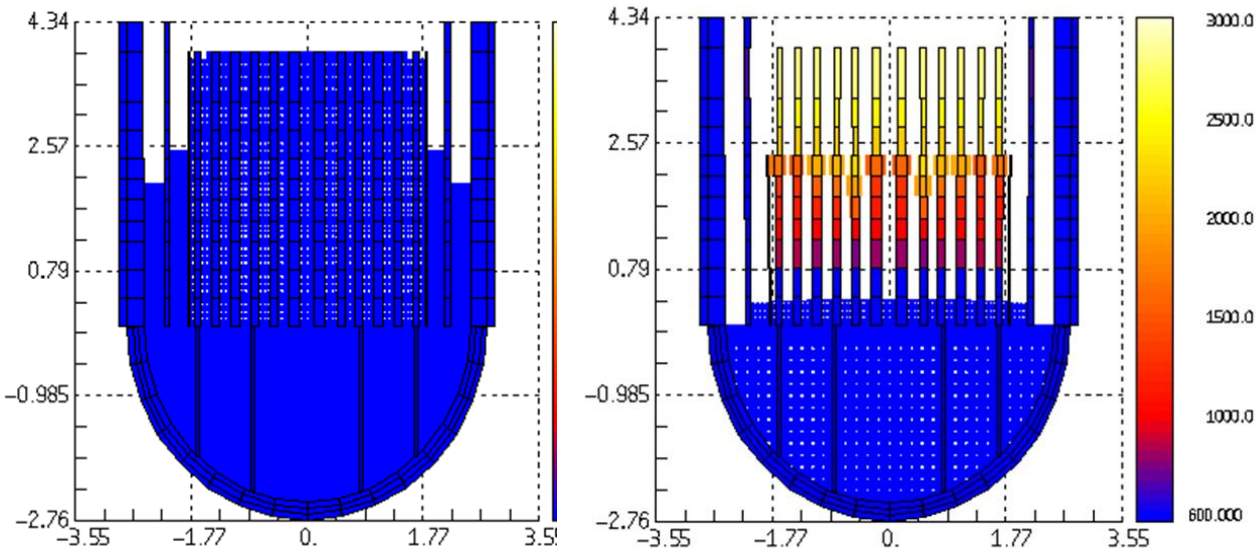

Figure 4 : ASTEC simulation of KONVOI core degradation: (left) core during dewatering, (right) core uncovered, heat-up of fuel rods

Similarly to Gómez-García-Toraño [54], Trometer [56] studied SAMGs and coolability of a degraded KONVOI reactor with the code ATHLET-CD. The German code ATHLET-CD (Analysis of Thermal-hydraulics of Leaks and Transients- Core Degradation) was developed by GRS, in cooperation with IKE. Like ASTEC, ATHLET-CD is a modular system and simulates normal operation of nuclear power plant as well as severe accidents [57]. In ATHLET-CD, the module MEWA (Melt and Water) [58] addresses the specific issue of debris bed coolability; while the code JEMI (jet fragmentation and Premixing) [59] focusses on molten jet fragmentation and debris settling, i.e. debris bed formation. Coupled together these two modules compose the code COCOMO-3D (Corium Coolability Model 3D), also developed by IKE. In the past, COCOMO-3D development focussed on the modelling of frictions, namely interfacial friction between steam and water, and also on the 3D extension of the code in order to deal with multidirectional effects (Hartmann et al. [60]) (e.g. for bed presenting an irregular geometry, non-symmetrical, like a heap-like bed against cavity wall). Currently, further development of the code is performed on the issue of settling of debris and prediction of debris bed formation, (Hilali et al. [61]) as well as self-levelling phenomena (Hilali et al. [62]).

1.2 Objectives

Water injection has been clearly depicted as the most relevant safety measure. The mechanisms involved during the reflooding of a quasi-intact core are to date well understood. Nevertheless, research on the reflooding of a severely degraded core, under the form of a debris bed, is still underway due to the complexity of the physical phenomena occurring in porous media. Hot debris beds are far more difficult to cool down and may re-melt into a molten pool, endangering the RPV integrity. Therefore, it is crucial that integral codes provide reliable simulations regarding the quenching of debris bed, in order to predict the success or the failure of the SAMGs. In addition, unlike common CFD codes, some integral codes (like ASTEC) were designed to be used as decision-making tools, which required a simplified representation of the physics as well as a coarse meshing, allowing for fast predictions and risk-analysis.

The goal of the present work is to improve the modelling of the quenching of hot particle bed, to be used in severe accident codes for emergency applications, i.e. designed for coarse numerical discretization. The work will be performed with the in-house code COCOMO-3D, dedicated to the specific issue of two-phase flow in porous media. From the outcomes of the COCOMO-3D investigations, suggestions will be made regarding the integration into integral codes in general.

In the next chapter (chapter 2), the actual modelling of two-phase flow in COCOMO-3D is presented. It details the system of conservation equations (mass, momentum and energy balance) for liquid, gas and solid, including all the relevant correlations involved in quenching processes, such as friction models and boiling regimes. As a matter of fact, the presence of pores implies an adapted representation of the friction between the solid phase and the fluid. Moreover, friction between gas and liquid should be also taken into account. As for the heat transfers between each phase, they are strongly dependent on the local boiling regime, mostly defined by the local temperature and liquid fraction. Afterwards it will be showed how all these equations are discretized on the structured meshing of the standard version of COCOMO-3D, or also on an unstructured meshing. The capabilities of the actual standard (thus, generating a regular structured meshing) version of COCOMO-3D in computing quenching of hot debris bed, applying a coarse meshing, is tested in the 3rd chapter. In order to validate COCOMO-3D, reference quenching experiments, such as DEBRIS and PEARL, are simulated, and the results

compared to the experimental outcomes. Focus is set on the one-dimensional quench front progression, but also on the 2D behaviour of the flow pattern (for PEARL). But, most of all, sensitivity analysis on the effect of discretization is carried out, since the final goal of this chapter is to evaluate the capability of COCOMO-3D in dealing with coarse meshing. In addition, in order to assess quenching simulations with cells as large as the ones generated in severe accident codes like ASTEC, quenching simulations of a reactor-scale debris bed are performed. Eventually, the whole chapter reveals a need to improve the modelling of the quench front itself, more precisely to detect and reconstruct the quench front, to better treat the thermo-hydraulics locally. The reconstruction issue, when using a coarse meshing, may also concern the debris bed geometry, which may lead to numerical errors due to overestimations of the exchange area, if not correctly reproduced. Hence, in the 4th chapter, a method to reproduce the debris bed geometry is developed. However, this kind of methods generates irregular cells, which necessarily requires the use of an unstructured meshing. For this reason, the present work could only go on with the unstructured version of COCOMO-3D (not the standard one). Detection and reconstruction of the quench front is more difficult than a basic geometry reconstruction, since it depends on physical parameters and evolves with time. After discussing pros and cons of existing reconstruction methods, the most appropriate method, for our specific case of quench front, is selected. Subsequently, the necessary local modifications of the conservation equations are deduced. The 4th chapter ends with a presentation of the new resolution scheme and of the implementation of the whole process (detection, reconstruction and resolution of the equation system). The implemented method is finally tested in the 5th chapter, by confronting it to simple cases as well as to the reactor-scale case that was presented in the 3rd chapter. On the results of the latter chapter, recommendations to upgrade the quenching modelling of severe accident codes will be concluded. The main steps of the present work are summarized on Figure 5.

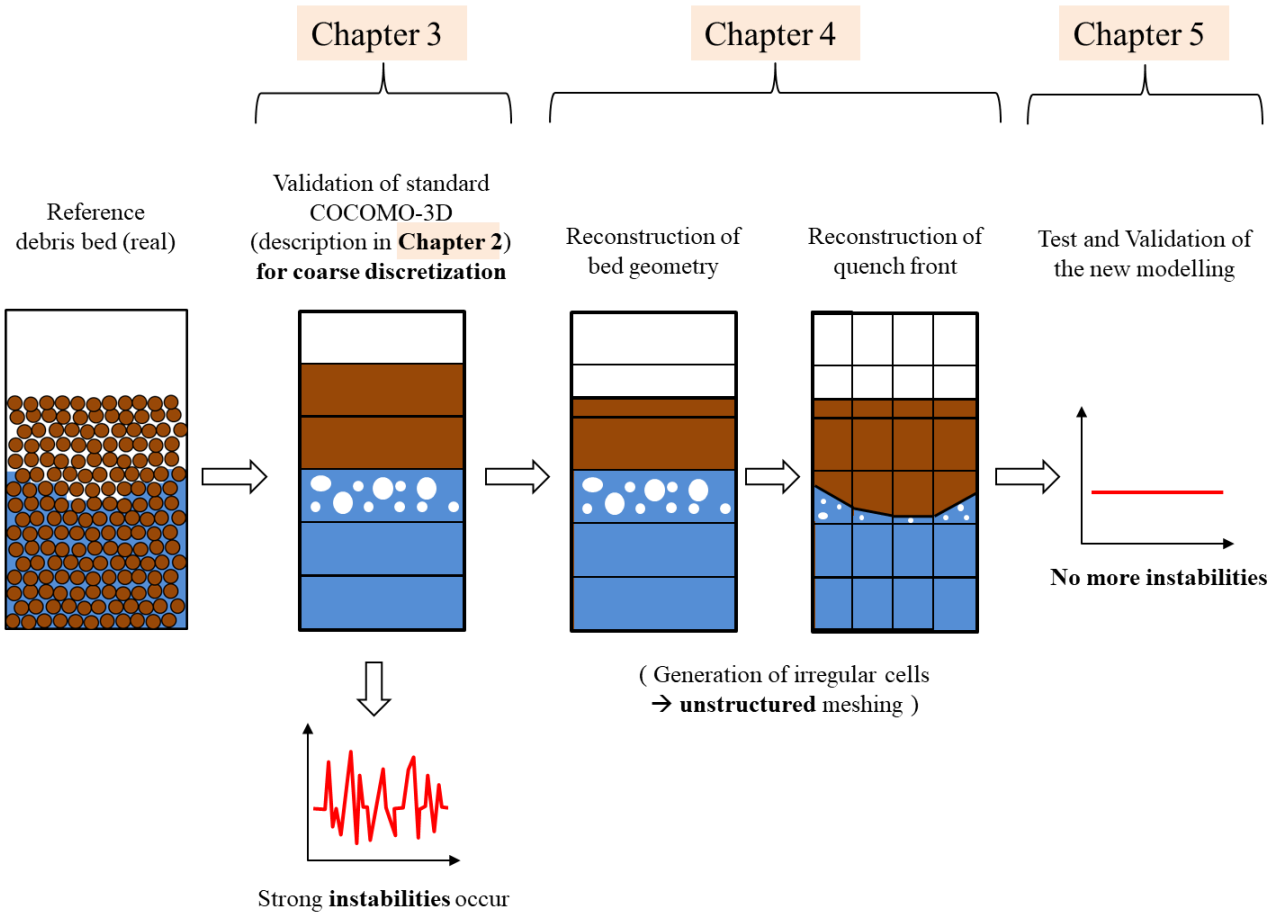

Figure 5 : Overview of the present work structure

2 COCOMO-3D Modelling

In this chapter the modelling of two-phase flow in COCOMO-3D is presented, as well as its implementation in the code. Since it is of particular importance for the understanding of the work, the resolution pattern of the system of equation will be also explained in detail. Afterwards, validation simulations on quenching will highlight the weaknesses of the current modelling, when it comes to calculation in emergency cases.

2.1 General

Debris bed coolability is a special problem of two-phase flow in a porous medium applied to accidents in nuclear power plants. During the cooling process water and steam may coexist, namely in boiling zones, where evaporation takes place. Water and steam present different flow patterns. For instance, by injecting water from the top of a debris bed, water flows downwards, while the steam, induced by the evaporation of the injected water, naturally flows upwards by buoyancy; so-called “counter-current” configuration. Inversely, by injecting water from the bottom, both water and steam will flow upwards; so-called “co-current” flows. In the counter-current case, water undergoes more friction with steam, i.e. pressure loss, than in co-current case. Friction between the two phases is a determinant process, and should better be explicitly taken into account by an appropriate model, in order to obtain realistic predictions from simulations. As a matter of fact, since the models of interfacial friction involve velocity difference between both phases, steam velocity must be distinguished from water velocity; i.e. they should be computed separately. In some models, water and steam are locally considered as a homogenous mixture, characterized by a mean velocity. In the specific case of two-phase flows in debris bed, this approach provides unsatisfactory results, as it was the case of an anterior version of the ASTEC code (v2.1.0) [63].

2.2 Modelling

In COCOMO-3D, each phase, i.e. liquid (water), gas (vapour) or solid (particles), is considered as a continuum. Each continuum is governed by the conservation equations for mass, momentum and energy. In the present study, the debris bed is assumed to be a fixed medium, in which liquid and gas flow through. Therefore, concerning the solid phase, only the energy conservation equation really plays a role; since there is no mass transport. Moreover, the gaseous phase covers not only steam, but also non-condensable gases, which can result from chemical reactions. Chemical reactions are though beyond the scope of the present work, henceforth only steam will be addressed when referring to the gaseous phase.

The solid continuum is namely characterized by the debris bed porosity ε, which is the fraction occupied by pores in a given control volume V. Volume fractions of gas and liquid are defined through their respective saturation denoted s_g and s_l, being basically the volume fraction in the porous space, such that:

$$s_l + s_g = 1 \tag{2-1}$$

Then the volume fractions of the solid, gas and liquid phases in a control volume can be defined as follows:

$$\frac{V_s}{V} = 1 - \varepsilon\,;\ \frac{V_g}{V} = s_g\varepsilon\,;\ \frac{V_l}{V} = s_l\varepsilon \tag{2-2}$$

With V_s, V_g and V_l, respectively the volume of solid, gas and liquid in the whole control volume V, such that:

$$V=V_s + V_l + V_g.$$

Additional specific parameters for a debris bed are also its permeability κ and passability μ, which will be used in the computation of the pressure losses in momentum balance equations. They describe the ability of water in penetrating into the debris bed, with regard of the local porosity and particle size (diameter D_p); thus, accounting for the extension or reduction of the flow path. κ and μ (2-3) were formerly determined by Ergun [64] for single phase flowing through a porous medium.

$$\kappa = \frac{\varepsilon^3 D_p^2}{150 \cdot (1-\varepsilon)^2}, \qquad \mu = \frac{\varepsilon^3 D_p}{1.75 \cdot (1-\varepsilon)} \tag{2-3}$$

For the case of two-phase flow, relative permeability ($\kappa_{rel,l}$, $\kappa_{rel,g}$) and passability ($\mu_{rel,l}$, $\mu_{rel,g}$) of each phase were introduced. Their computation will be developed in section 2.2.2.

2.2.1 Mass conservation

The mass conservation equations for steam and liquid, denoted with the indices *g* and *l* respectively, are expressed in (2-4) and (2-5), where $\Gamma^{evap}$is the mass transfer rate due to evaporation (when positive) or condensation (when negative). As a matter of fact, when positive, it appears as a steam source in the gas equation and as a corresponding water loss in the liquid equation. $\vec{w}$ is the phase velocity, and thus the second term of the left side of the equation expresses the gradient of the phase mass flow. ρ_g and ρ_l are the gas and liquid densities respectively.

$$\frac{\partial}{\partial t}\left(\varepsilon s_g \rho_g\right) + \nabla \cdot \left(\rho_g \varepsilon s_g \overrightarrow{w_g}\right) = \Gamma^{evap} \tag{2-4}$$

$$\frac{\partial}{\partial t}\left(\varepsilon s_l \rho_l\right) + \nabla \cdot \left(\rho_l \varepsilon s_l \overrightarrow{w_l}\right) = -\Gamma^{evap} \tag{2-5}$$

2.2.2 Momentum conservation

In the momentum conservation equations, convective terms and time derivative (both, derivatives of velocities) are neglected, since in porous medium friction forces are dominant, as well as the pressure gradient and the weight. When the fluid velocity is low (*Re << 1*) [65], the inertial term can be also neglected.

$$K_{gs}\overrightarrow{u_g} + \frac{K_{gl}}{s_g}\left(\overrightarrow{w_g} - \overrightarrow{w_l}\right) = -\nabla p_g + \rho_g \vec{g} \tag{2-6}$$

$$K_{ls}\vec{u_l} - \frac{K_{gl}}{s_l}\left(\vec{w_g} - \vec{w_l}\right) = -\nabla p_l + \rho_l \vec{g} \tag{2-7}$$

It can be assumed that liquid and steam pressures, p_l and p_g, are the same if capillary forces are neglected. However, if particles are very small (< 1mm), capillary forces have to be considered. In that case p_l and p_g are different and can be related to each other, taking into account the capillary pressure p_c:

$$p_l = p_g - p_c \tag{2-8}$$

Further information about the calculation of the capillary pressure can be found in MEWA-documentation [66]. The first term of the left side of the equations (2-6) and (2-7) represents the friction between fluid and the solid phase. K_{gs} and K_{ls} are the friction coefficients between steam/water and particles. In COCOMO-3D, the interfacial friction is explicitly modelled through the second term of the left side of the equation.

The friction models can be presented as an adaptation of Ergun's law, addressing originally single-phase flow, for two-phase flow in porous medium. The friction coefficients are assumed to have a laminar (viscous friction term) and a turbulent (inertial term) part, like shown below:

$$K_{gs} = K_{gs}^{lam} + K_{gs}^{turb}\left|\vec{w_g}\right|, \qquad K_{ls} = K_{ls}^{lam} + K_{ls}^{turb}\left|\vec{w_l}\right|, \qquad K_{gl} = K_{gl}^{lam} + K_{gl}^{turb}\left|\vec{w_g} - \vec{w_l}\right| \tag{2-9}$$

Concerning K_{gs} and K_{ls}, the components K^{lam} and K^{turb} can also be expressed as functions of relative permeability and relative passability respectively, as follows:

$$K_{gs} = \frac{\varepsilon s_g \eta_g}{\kappa \kappa_{rel,g}} + \frac{\varepsilon^2 s_g^2 \rho_g}{\mu \mu_{rel,g}}\left|\vec{w_g}\right|, \qquad K_{ls} = \frac{\varepsilon s_l \eta_l}{\kappa \kappa_{rel,l}} + \frac{\varepsilon^2 s_l^2 \rho_l}{\mu \mu_{rel,l}}\left|\vec{w_l}\right| \tag{2-10}$$

Therefore, only models for κ_{rel} and μ_{rel} are required for the calculation of K_{gs} and K_{ls}, since all the other parameters are known. However, K_{gl} cannot be developed that easily and needs a more sophisticated correlation.

For the calculation of the friction coefficients K_{gs}, K_{ls} and K_{gl}, several models are available from prior investigations. In general, they are classified into two groups: without or with consideration

of interfacial friction. Among the models that do not consider explicitly friction between water and steam ($K_{gl} = 0$), Lipinski [67], Reed [68] and Hu and Theofanous [69] are often mentioned; they are based on an extension of the Ergun's law. For an explicit consideration of the interfacial friction, one can refer to models like those of Schulenberg and Müller [70] or also Tung and Dhir [71]. The latter model presents the advantages to take into account the local flow regime (annular flow, slug flow, high and low void bubbly flow). In COCOMO-3D a modified version of the Tung and Dhir model implemented by Schmidt [72] is available. This version might able to deal with very small particles and with top-flooding; since the original model typically overestimates the friction between phases in counter-current configuration. Comparisons of the different methods are summarized in the work of Rahman [73]. Calculations in the present work were run with the modified version of Tung and Dhir.

As mentioned, in the modified Tung and Dhir model, the friction coefficients are computed depending on the flow regime. The void fraction (i.e. gas saturation) is taken as criterion to distinguish the different regimes, as shown in Table 1.

In the modified Tung and Dhir model, relative permeabilities and passabilities for gas/particle drag for the liquid continuous region (LC) become:

$$\kappa_{\mathrm{rel,g}}^{\mathrm{LC}} = \mathrm{s_g^3}\,, \qquad \mu_{\mathrm{rel,g}}^{\mathrm{LC}} = \mathrm{s_g^3}$$

and for the gas continuous region (GC):

$$\kappa_{\mathrm{rel,g}}^{\mathrm{GC}} = \mathrm{s_g^2}\,, \qquad \mu_{\mathrm{rel,g}}^{\mathrm{GC}} = \mathrm{s_g^2}$$

In the transition between liquid continuous and gas continuous region (LGT), the gas/particle friction coefficient is obtained by interpolation between the coefficients of the respective regime,

$$\mathrm{K_{gs}^{LGT}} = [1 - \mathrm{W}(\mathrm{s_g}, 0.6, \pi\sqrt{2}/6)] \cdot \mathrm{K_{gs}^{LC}} + \mathrm{W}(\mathrm{s_g}, 0.6, \pi\sqrt{2}/6) \cdot \mathrm{K_{gs}^{GC}} \qquad (2\text{-}11)$$

using the weighting function *W*:

$$\mathrm{W}(\mathrm{s}, \mathrm{s_{min}}, \mathrm{s_{max}}) = 3 \cdot \left(\frac{\mathrm{s} - \mathrm{s_{min}}}{\mathrm{s_{max}} - \mathrm{s_{min}}}\right)^2 - 2 \cdot \left(\frac{\mathrm{s} - \mathrm{s_{min}}}{\mathrm{s_{max}} - \mathrm{s_{min}}}\right)^3$$

However, the liquid/particle drag is independent of the flow regime. The proposed relative permeabilities and passabilities are

$$\kappa_{rel,l} = s_l^2 , \qquad \mu_{rel,l} = s_l^5$$

As for the formulation of the interfacial friction for the bubbly and slug flow, coefficients are

$$K_{gl}^{LB} = K_{gl,TD}^{LB} \cdot \min\left(1, \frac{D_p}{1.2\cdot 10^{-2} m}\right); \; K_{gl}^{HB} = K_{gl,TD}^{HB} \cdot \min\left(1, \frac{D_p}{1.2\cdot 10^{-2} m}\right)$$

$$K_{gl}^{S} = K_{gl,TD}^{S} \cdot \min\left(1, \frac{D_p}{1.2 \cdot 10^{-2} m}\right) \tag{2-12}$$

Table 1 : Validity range of the flow regimes

Continuum	**Flow regime**	**Gas saturation (s_g) validity range**
Liquid *(LC)*	Low void bubbly *(LB)*	$s_g \leq s_{g,0}$ with $s_{g,0} = \max\left\{0, \frac{\pi}{3} \cdot \frac{(1-\varepsilon)}{\varepsilon} \cdot \gamma \cdot (1+\gamma) \cdot [6\beta - 5 \cdot (1+\gamma)]\right\}$ and $\gamma = \frac{D_B}{D_P}$, $D_B = 1.35\sqrt{\frac{\sigma}{g(\rho_l - \rho_g)}}$, $\beta = \left(\frac{\pi\sqrt{2}}{6(1-\varepsilon)}\right)^{\frac{1}{3}}$
	High void bubbly *(HB)*	$s_{g,0} < s_g \leq s_{g,1}$ with $s_{g,1} = \min\left\{s_{g,1TD}, \left(\frac{D_P - D_{P0}}{1.35\cdot 10^{-2}\, m}\right)^3 + s_{g,1TD}\right\}$ and $s_{g,1TD} = \min\{0.3, 0.6 \cdot (1-\gamma)^2\}$, $D_{P0} = 1.2 \cdot 10^{-2}$
	Transition bubbly-slug *(BST)*	$s_{g,1} < s_g \leq \min\left\{\frac{\pi}{6}, \left(\frac{D_P - D_{P0}}{1.35 \cdot 10^{-2}\, m}\right)^3 + \frac{\pi}{6}\right\}$
	Slug *(S)*	$\min\left\{\frac{\pi}{6}, \left(\frac{D_P - D_{P0}}{1.35 \cdot 10^{-2}\, m}\right)^3 + \frac{\pi}{6}\right\} < s_g \leq \min\left\{0.6, \left(\frac{D_P - D_{P0}}{1.35 \cdot 10^{-2}\, m}\right)^3 + 0.6\right\}$
Transition *(LGT)*	Transition slug-annular *(SAT)*	$\min\left\{0.6, \left(\frac{D_P - D_{P0}}{1.35 \cdot 10^{-2}\, m}\right)^3 + 0.6\right\} < s_g \leq \min\left\{\frac{\pi\sqrt{2}}{6}, \left(\frac{D_P - D_{P0}}{1.35 \cdot 10^{-2}\, m}\right)^3 + \frac{\pi\sqrt{2}}{6}\right\}$
Gas *(GC)*	Annular *(A)*	$s_g > \min\left\{\frac{\pi\sqrt{2}}{6}, \left(\frac{D_P - D_{P0}}{1.35 \cdot 10^{-2}\, m}\right)^3 + \frac{\pi\sqrt{2}}{6}\right\}$

With $K_{gl,TD}^{LB}$, $K_{gl,TD}^{HB}$ and $K_{gl,TD}^{S}$ the coefficients obtained by the original Tung and Dhir model,

$$\mathrm{K_{gl,TD}^{LB}} = 18 \cdot \mathrm{s_g} \cdot \mathrm{s_l} \cdot \frac{1+\gamma}{2} \cdot \ln\left(1+\frac{2}{\gamma}\right) \cdot \frac{\eta_l}{\mathrm{D_B^2}} \tag{2-13}$$

$$+0.34 \cdot \mathrm{s_g} \cdot \mathrm{s_l^5} \cdot \left[\frac{1+\gamma}{2} \cdot \ln\left(1+\frac{2}{\gamma}\right)\right]^2 \cdot \frac{\rho_l s_l + \rho_g s_g}{\mathrm{D_B}} \cdot |\overrightarrow{\mathrm{w_{rel}}}|$$

$$\mathrm{K_{gl,TD}^{HB}} = 18 \cdot \left[\mathrm{s_{g,0}} \cdot \frac{1+\gamma}{2} \cdot \ln\left(1+\frac{2}{\gamma}\right) + \mathrm{s_g} - \mathrm{s_{g,0}}\right] \cdot \mathrm{s_l} \cdot \frac{\eta_l}{\mathrm{D_B^2}} \tag{2-14}$$

$$+0.34 \cdot \left(\mathrm{s_{g,0}} \cdot \left[\frac{1+\gamma}{2} \cdot \ln\left(1+\frac{2}{\gamma}\right)\right]^2 + \mathrm{s_g} - \mathrm{s_{g,0}}\right) \cdot \mathrm{s_l^5} \cdot \frac{\rho_l s_l + \rho_g s_g}{\mathrm{D_B}} \cdot |\overrightarrow{\mathrm{w_{rel}}}|$$

$$\mathrm{K_{gl,TD}^{S}} = 5.21 \cdot \mathrm{s_g} \cdot \mathrm{s_l} \cdot \frac{\eta_l}{\mathrm{D_B^2}} + 0.92 \cdot \mathrm{s_g} \cdot \mathrm{s_l^5} \cdot \frac{\rho_l s_l + \rho_g s_g}{\mathrm{D_B}} \cdot |\overrightarrow{\mathrm{w_{rel}}}| \tag{2-15}$$

and for the annular flow

$$\mathrm{K_{gl}^{A}} = \mathrm{K_{gl,TD}^{A}} \cdot 0.25 \cdot \min\left(1, \left(\frac{\mathrm{d_p}}{0.3 \cdot 10^{-2} m}\right)^3\right) \tag{2-16}$$

With $K_{gl,TD}^{A}$ the coefficients obtained by the original Tung and Dhir model,

$$\mathrm{K_{gl,TD}^{A}} = \mathrm{K_{gs}^{GC}} \cdot \mathrm{s_l} \tag{2-17}$$

For the interfacial friction coefficients in the transition regions between the bubbly and slug flow regimes, as well as between the slug and annular flow regimes, a weighting between the respective regimes is applied:

$$\mathrm{K_{gl}^{BST}} = [1 - \mathrm{W}(\mathrm{s_g},\ \mathrm{s_{g,1}}, 0.3)] \cdot \mathrm{K_{gl}^{HB}} + \mathrm{W}(\mathrm{s_g},\ \mathrm{s_{g,1}}, 0.3) \cdot \mathrm{K_{gl}^{S}} \tag{2-18}$$

$$\mathrm{K_{gl}^{SAT}} = [1 - \mathrm{W}(\mathrm{s_g}, 0.6, \pi\sqrt{2}/6)] \cdot \mathrm{K_{gl}^{S}} + \mathrm{W}(\mathrm{s_g}, 0.6, \pi\sqrt{2}/6) \cdot \mathrm{K_{gl}^{A}} \tag{2-19}$$

2.2.3 Energy balance

Regarding now the energy balance, the three phases are assumed to be in thermal non-equilibrium; i.e. particles, water and steam have different temperatures. Subsequently, thermal exchanges between phases must be considered. Energy conservation equations for solid, steam and water are expressed in (2-20), (2-21) and (2-22), ensuring the balance between the temporal variation of the specific internal energy (denoted e_s, e_g and e_l for the particles, steam and water) and the different heat exchanges involved.

$$\frac{\partial}{\partial t}\left((1-\varepsilon)\rho_s e_s\right) = \nabla\cdot\left(\lambda_s^{eff}\nabla T_s\right) + Q_{s,source} - Q_{s,sat} - Q_{s,g} - Q_{s,l} \tag{2-20}$$

$$\frac{\partial}{\partial t}\left(\varepsilon s_g \rho_g e_g\right) + \nabla\cdot\left(\varepsilon s_g \rho_g \overrightarrow{w_g} i_g\right) = \nabla\cdot\left(\lambda_g^{eff}\nabla T_g\right) + Q_{s,g} + Q_{l,g} + Q_{sat,g} + \Gamma^{evap} i_{g,sat} \tag{2-21}$$

$$\frac{\partial}{\partial t}\left(\varepsilon s_l \rho_l e_l\right) + \nabla\cdot\left(\varepsilon s_l \rho_l \overrightarrow{w_l} i_l\right) = \nabla\cdot\left(\lambda_l^{eff}\nabla T_l\right) + Q_{s,l} - Q_{l,g} + Q_{sat,l} - \Gamma^{evap} i_{l,sat} \tag{2-22}$$

The first term of the right-hand side of the solid equation (2-20) denotes the heat conduction (with the effective conductivity λ_s^{eff}). While $Q_{s,source}$ represents the generated heat source (e.g. decay heat inside particles due to fission products), $Q_{s,g}$, $Q_{s,l}$ and $Q_{s,sat}$ denote the volumetric heat flux from particles to the surrounding gas, water and steam-water interface, respectively. As a matter of fact, $Q_{s,g}$ and $Q_{s,l}$ must also appear in the gas and liquid equations. The second term of the left-hand side of gas and liquid equations is the enthalpy fluxes from mass transfer. Enthalpy flux from evaporation/condensation is obtained through the mass rate of generated steam Γ^{evap} (2-32), multiplied by the specific enthalpy at saturation point, denoted $i_{l,sat}$ for liquid and $i_{g,sat}$ for gas. Densities and the specific enthalpies are obtained from the water and steam properties package from ATHLET, as a function of the pressure and temperature. In order to close the problem, additional relations are necessary. Computation of heat transfer between phases is based on empirical correlations.

The boiling heat transfer is addressed by $Q_{s,sat}$, which is the heat from the particles to the water-steam interface. It has the following form:

$$\mathrm{Q_{s,sat}} = \mathrm{a_{s,sat}} \mathrm{h_{s,sat}} (\mathrm{T_s} - \mathrm{T_{sat}}) \tag{2-23}$$

With the interfacial area density:

$$\mathrm{a_{s,sat}} = \frac{6 \cdot (1-\varepsilon)}{\mathrm{D_p}} \left(= \frac{\text{solid fraction}}{\underbrace{\text{single particle volume}}_{\text{number of particles}}} \cdot \text{single particle surface area} \right)$$

The heat transfer coefficient $h_{s,sat}$ is given by correlations, with respect to the boiling regime (nucleate boiling, film boiling, transition), differing from the flow regimes mentioned in the previous section. Obviously boiling occurs only if the particle temperature T_s has reached the saturation temperature T_{sat}, otherwise pure liquid convection (heat flux from particles to liquid only) is considered. Two temperatures are defined in order to distinguish the different boiling regions: the minimal film boiling temperature T_{min}^{FB} and maximal nucleate boiling temperature T_{max}^{NB}. These temperatures are estimated as follows:

$$\mathrm{T_{min}^{FB}} = \mathrm{T_{sat}} + 100\ \mathrm{K}\,;\ \mathrm{T_{max}^{NB}} = \mathrm{T_{min}^{FB}} + 17\ \mathrm{K}$$

And the heat transfer coefficients are computed with respect to the following correlations:

- If $T_s \leq T_{min}^{FB}$, pure nucleate boiling (NB) is assumed. In that case, one refers to the Rohsenow's correlation [74] to compute $h_{s,sat}^{NB}$:

$$\mathrm{h_{s,sat}^{NB}} = \frac{\mathrm{c_{p,l}^3} \cdot \eta_\mathrm{l} \cdot (\mathrm{T_s} - \mathrm{T_{sat}})^2}{(\mathrm{i_{g,sat}} - \mathrm{i_{l,sat}})^2 \cdot (1.2 \cdot 10^{-2} \cdot \mathrm{Pr_l})^3 \cdot \sqrt{\frac{\mathrm{g_0} \cdot \sigma_\mathrm{l}}{\mathrm{g}(\rho_\mathrm{l} - \rho_\mathrm{g})}}} \tag{2-24}$$

  With $c_{p,l}$, the specific heat capacity, $\mathrm{g_0}$, the force conversion factor equal to 1.0 $\frac{\mathrm{kg \cdot m}}{\mathrm{N \cdot s^2}}$, and Pr_l, the Prandtl number of the liquid phase:

$$\mathrm{Pr_l} = \frac{\eta_\mathrm{l}\, \mathrm{c_{p,l}}}{\lambda_\mathrm{l}} \tag{2-25}$$

- If $T_s \geq T_{max}^{NB}$, pure film boiling (FB) is assumed. In that case, one refers to the Lienhard's correlation [75] to compute $h_{s,sat}^{FB}$:

$$\mathrm{h_{s,sat}^{FB}} = \frac{\mathrm{Nu_{s,sat}^{FB}}\,\lambda_g}{\mathrm{D_P}} \tag{2-26}$$

$Nu_{s,sat}^{FB}$, the Nusselt number being:

$$\mathrm{Nu_{s,sat}^{FB}} = 0.67 \cdot \left(\frac{\rho_g \cdot g \cdot (\rho_l - \rho_g) \cdot \Delta i'_{sat} \cdot D_P^3}{\lambda_g \cdot \eta_g \cdot (T_s - T_{sat})}\right)^{1/4} \tag{2-27}$$

With the modified latent heat $\Delta i'_{sat}$, which is a function of the Prandtl Pr_g and Jacob numbers *Ja*:

$$\Delta i'_{sat} = (i_{g,sat} - i_{l,sat}) \cdot \left[1 + \left(0.968 - \frac{0.163}{Pr_g}\right) \cdot Ja\right] \tag{2-28}$$

$$Ja = \frac{c_{p,g} \cdot (T_s - T_{sat})}{(i_{g,sat} - i_{l,sat})} \tag{2-29}$$

- The range defined by $T_{min}^{FB} < T_s < T_{max}^{NB}$ represents a transition regime (TB), a mix of nucleate and film boiling. The heat transfer coefficient $h_{s,sat}^{TB}$ is basically obtained by linear interpolation between the heat transfer coefficients of nucleate and film boiling:

$$\mathrm{h_{s,sat}^{TB}} = \left[1 - \frac{T_s - T_{min}^{FB}}{T_{max}^{NB} - T_{min}^{FB}}\right] \cdot \mathrm{h_{s,sat}^{NB}}\left(T_{min}^{FB}\right) + \left[\frac{T_s - T_{min}^{FB}}{T_{max}^{NB} - T_{min}^{FB}}\right] \cdot \mathrm{h_{s,sat}^{FB}}\left(T_{min}^{NB}\right) \tag{2-30}$$

The different boiling zones during the quenching of hot debris can be observed on Figure 6. This represents 2.0 m high debris bed quenched by bottom-flooding. The initial bed temperature was approximately 1400 °C. In this case, an injection rate of 6.5 kg/s/m² (50 kg/s in a cross section of 7.45 m²; bed radius = 1.54 m) was chosen, which is high enough to identify the boiling regions easily. With a lower injection rate, the zone boundaries would have been nearer to each other and hard to distinguish. Under boiling regime, to calculate the heat flux from liquid to interface $Q_{l,sat}$, one assumed that it corresponds to approximately 20% of the heat flux obtained with the heat transfer coefficient $h_{s,sat}$ (previously computed for the heat flux from particles to interface):

$$Q_{l,sat} = 0.2\, a_{s,sat} h_{s,sat} (T_l - T_{sat}) \quad (2\text{-}31)$$

For porous medium configuration, COCOMO-3D neglects $Q_{g,sat}$ and $Q_{l,g}$.

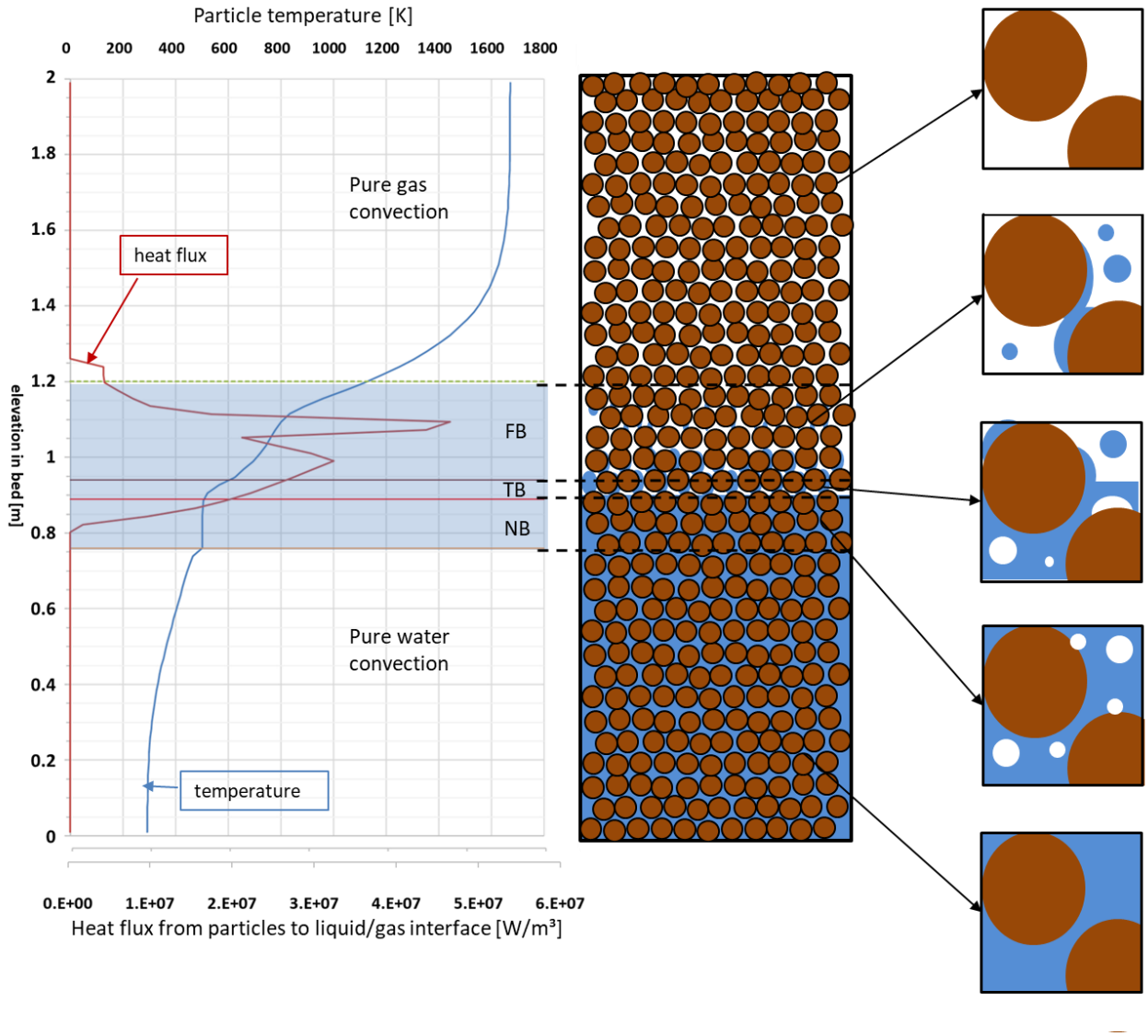

Figure 6 : Axial temperature and heat flux profiles along the debris bed during quenching - Boiling regimes defined in COCOMO-3D

From $Q_{s,sat}$ and $Q_{l,sat}$, one can estimate the evaporation rate Γ^{evap} given by:

$$\Gamma^{evap} = \frac{Q_{s,sat} + Q_{l,sat}}{i_{g,sat} - i_{l,sat}} \quad (2\text{-}32)$$

If water is subcooled ($T_l < T_{sat}$) and in sufficient quantity ($s_l > 0.3$), direct convective heat transfer from particles to liquid $Q_{s,l}$ is assumed. If superheated steam is in sufficient quantity ($s_g > 0.7$, i.e. $s_l < 0.3$), direct convective heat transfer from particles to steam $Q_{s,g}$ is assumed. As a matter of fact, heat transfer from particles to water and to steam cannot be present simultaneously. Their expression follows also the form of (2-23). More details about their computation are to be found in Appendix-F.

2.3 Discretization

2.3.1 Structured meshing (standard)

The basic meshing option in COCOMO-3D generates a regular orthogonal structured grid under cylindrical or Cartesian coordinates, following the staggered grid concept (see Figure 7). Scalar quantities, such as pressures, temperatures and volume fractions, are defined at cell centres, and represent properties of the whole control volume, i.e. cell. Vector quantities, like the velocity (and subsequently, mass flux and convective enthalpy fluxes) and conductive heat fluxes are computed at cell boundaries, i.e. cell faces. Cell centres are denoted by indices (*i,j*), where *i* is the index of the radial direction and *j* is the index of the axial direction, like shown on figure. Faces, on the left, right, bottom and top are denoted by "half" indices $\left(i-\frac{1}{2},j\right)$, $\left(i+\frac{1}{2},j\right)$, $\left(i,j-\frac{1}{2}\right)$ and $\left(i,j+\frac{1}{2}\right)$. COCOMO-3D allows also an azimuthal discretization of the computational domain. However, whereas the existence of a third axis must be kept in mind, no further development regarding the azimuthal discretization will be done in this chapter, for one reason: essentially 1D and 2D simulations will be performed throughout the present work, assuming that the forthcoming results and conclusions will be valid for 3D simulations too.

The implicit Euler's method is applied to discretize the conservation equations. The equation were spatially discretized by applying the finite volume method (see Patankar [76]). Time derivatives in the mass and energy equations are approximated by a first order backward difference. While mass (2-33)(2-34) and energy (2-40)(2-41)(2-42) equations address each cell, momentum conservation on the radial (2-36)(2-37) and axial (2-38)(2-39) direction must be

distinguished, since the axial direction accounts also for the gravity contribution. All quantities correspond to the current time level *t*, except the quantities with the index 'old', computed at the previous time level t^{old}.

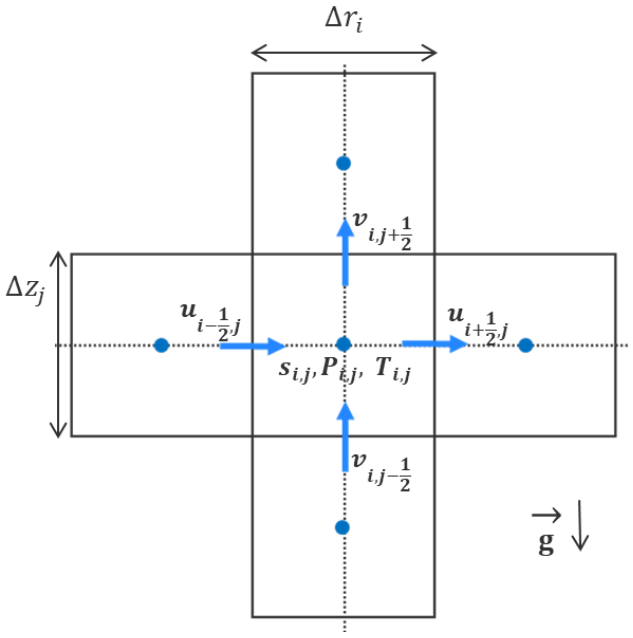

Figure 7 : structured staggered grid of the standard version of COCOMO-3D

The discretized form of the mass conservation equations, for gas and liquid, are given as follows:

$$V_{i,j}\frac{(\varepsilon s_g \rho_g)_{i,j} - (\varepsilon s_g \rho_g)^{old}_{i,j}}{\Delta t} = \dot{m}_{g,i-\frac{1}{2},j} - \dot{m}_{g,i+\frac{1}{2},j} + \dot{m}_{g,i,j-\frac{1}{2}} - \dot{m}_{g,i,j+\frac{1}{2}} + V_{i,j}\cdot\Gamma^{evap}_{i,j} \tag{2-33}$$

$$V_{i,j}\frac{(\varepsilon s_l \rho_l)_{i,j} - (\varepsilon s_l \rho_l)^{old}_{i,j}}{\Delta t} = \dot{m}_{l,i-\frac{1}{2},j} - \dot{m}_{l,i+\frac{1}{2},j} + \dot{m}_{l,i,j-\frac{1}{2}} - \dot{m}_{l,i,j+\frac{1}{2}} - V_{i,j}\cdot\Gamma^{evap}_{i,j} \tag{2-34}$$

With

$$\dot{m}_{k,I,J} = A_{I,J}\langle\rho_k\rangle_{I,J}\langle\varepsilon\rangle_{I,J}\langle s_k\rangle_{I,J}u_{k,I,J}\,, \tag{2-35}$$

for phase $k = g, l$; and indices $(I,J) = \left(i \pm \frac{1}{2}, j\right)$ in radial direction or $\left(i, j \pm \frac{1}{2}\right)$ in axial direction.

The radial discretization of the momentum conservations, for gas and liquid, yields:

$$\langle K_{gs}^{lam}\rangle_{i+\frac{1}{2},j}\, u_{g,i+\frac{1}{2},j} + \langle K_{gs}^{turb}\rangle_{i+\frac{1}{2},j}\, \langle|\overrightarrow{w_g}|\rangle_{i+\frac{1}{2},j}\, u_{g,i+\frac{1}{2},j} + \langle\frac{K_{gl}^{lam}}{s_g}\rangle_{i+\frac{1}{2},j}\left(u_{g,i+\frac{1}{2},j} - u_{l,i+\frac{1}{2},j}\right) + \langle\frac{K_{gl}^{turb}}{s_g}\rangle_{i+\frac{1}{2},j}\ \langle|\overrightarrow{w_g} - \overrightarrow{w_l}|\rangle_{i+\frac{1}{2},j}\left(u_{g,i+\frac{1}{2},j} - u_{l,i+\frac{1}{2},j}\right) = -\frac{p_{g,i+1,j} - p_{g,i,j}}{\frac{1}{2}(\Delta r_i + \Delta r_{i+1})} \quad (2\text{-}36)$$

$$\langle K_{ls}^{lam}\rangle_{i+\frac{1}{2},j}\, u_{l,i+\frac{1}{2},j} + \langle K_{ls}^{turb}\rangle_{i+\frac{1}{2},j}\, \langle|\overrightarrow{w_l}|\rangle_{i+\frac{1}{2},j}\, u_{l,i+\frac{1}{2},j} - \langle\frac{K_{gl}^{lam}}{s_l}\rangle_{i+\frac{1}{2},j}\left(u_{g,i+\frac{1}{2},j} - u_{l,i+\frac{1}{2},j}\right) - \langle\frac{K_{gl}^{turb}}{s_l}\rangle_{i+\frac{1}{2},j}\ \langle|\overrightarrow{w_g} - \overrightarrow{w_l}|\rangle_{i+\frac{1}{2},j}\left(u_{g,i+\frac{1}{2},j} - u_{l,i+\frac{1}{2},j}\right) = -\frac{p_{l,i+1,j} - p_{l,i,j}}{\frac{1}{2}(\Delta r_i + \Delta r_{i+1})} \quad (2\text{-}37)$$

With $\overrightarrow{w_g}\ (u_g, v_g)$ and $\overrightarrow{w_l}\ (u_l, v_l)$, the vector for gas and liquid velocity respectively. Information regarding the interpolation of their norms $\langle|\overrightarrow{w_g}|\rangle$ and $\langle|\overrightarrow{w_l}|\rangle$ can be found directly in Appendix-B. Quantities in brackets are quantities that requires to be interpolated, since they are not directly defined at the half position like $\left(i+\frac{1}{2}, j\right)$, but at centre of cells. Different interpolation methods exist: linear, geometrical or upwind (donor cell). Those are summarized in Appendix-C.

The axial discretization of the momentum conservation equations, for gas and liquid, yields:

$$\langle K_{gs}^{lam}\rangle_{i,j+\frac{1}{2}}\, u_{g,i,j+\frac{1}{2}} + \langle K_{gs}^{turb}\rangle_{i,j+\frac{1}{2}}\, \langle|\overrightarrow{w_g}|\rangle_{i,j+\frac{1}{2}}\, v_{g,i,j+\frac{1}{2}} + \langle\frac{K_{gl}^{lam}}{s_g}\rangle_{I,j+\frac{1}{2}}\left(v_{g,I,j+\frac{1}{2}} - v_{l,I,j+\frac{1}{2}}\right) + \langle\frac{K_{gl}^{turb}}{s_g}\rangle_{i,j+\frac{1}{2}}\ \langle|\overrightarrow{w_g} - \overrightarrow{w_l}|\rangle_{i,j+\frac{1}{2}}\left(v_{g,i,j+\frac{1}{2}} - v_{l,i,j+\frac{1}{2}}\right) = -\frac{p_{g,i,j+1} - p_{g,i,j}}{\frac{1}{2}(\Delta z_i + \Delta z_{i+1})} - g\cdot\langle\rho_g\rangle_{i,j+\frac{1}{2}}, \quad (2\text{-}38)$$

$$\langle K_{ls}^{lam}\rangle_{i,j+\frac{1}{2}}\, u_{l,i,j+\frac{1}{2}} + \langle K_{ls}^{turb}\rangle_{i,j+\frac{1}{2}}\, \langle|\overrightarrow{w_l}|\rangle_{i,j+\frac{1}{2}}\, v_{l,i,j+\frac{1}{2}} - \langle\frac{K_{gl}^{lam}}{s_l}\rangle_{i,j+\frac{1}{2}}\left(v_{g,i,j+\frac{1}{2}} - v_{l,i,j+\frac{1}{2}}\right) + \langle\frac{K_{gl}^{turb}}{s_l}\rangle_{i,j+\frac{1}{2}}\ \langle|\overrightarrow{w_g} - \overrightarrow{w_l}|\rangle_{i,j+\frac{1}{2}}\left(v_{g,i,j+\frac{1}{2}} - v_{l,i,j+\frac{1}{2}}\right) = -\frac{p_{l,i,j+1} - p_{l,i,j}}{\frac{1}{2}(\Delta z_i + \Delta z_{i+1})} - g\cdot\langle\rho_l\rangle_{i,j+\frac{1}{2}}, \quad (2\text{-}39)$$

The discretized forms of the energy conservation equations, for gas, liquid and solid are given below:

$$V_{i,j}\frac{\left(\varepsilon s_g \rho_g e_g\right)_{i,j} - \left(\varepsilon s_g \rho_g e_g\right)^{old}_{i,j}}{\Delta t} = \dot{q}_{g,i-\frac{1}{2},j} - \dot{q}_{g,i+\frac{1}{2},j} + \dot{q}_{g,i,j-\frac{1}{2}} - \dot{q}_{g,i,j+\frac{1}{2}} + V_{i,j}\left(Q_{s,g,i,j} + Q_{l,g,i,j} + Q_{sat,g,i,j} + \Gamma^{evap}_{i,j} i_{g,sat,i,j}\right) \quad (2\text{-}40)$$

$$V_{i,j}\frac{(\varepsilon s_l \rho_l e_l)_{i,j} - (\varepsilon s_l \rho_l e_l)^{old}_{i,j}}{\Delta t} = \dot{q}_{l,i-\frac{1}{2},j} - \dot{q}_{l,i+\frac{1}{2},j} + \dot{q}_{l,i,j-\frac{1}{2}} - \dot{q}_{l,i,j+\frac{1}{2}} + V_{i,j}\left(Q_{s,l,i,j} - Q_{l,g,i,j} + Q_{sat,l,i,j} - \Gamma^{evap}_{i,j} i_{l,sat,i,j}\right) \quad (2\text{-}41)$$

$$V_{i,j}\frac{\left((1-\varepsilon)\rho_s e_s\right)_{i,j} - \left((1-\varepsilon)\rho_s e_s\right)^{old}_{i,j}}{\Delta t} = \dot{q}^{cond}_{s,i-\frac{1}{2},j} - \dot{q}^{cond}_{s,i+\frac{1}{2},j} + \dot{q}^{cond}_{s,i,j-\frac{1}{2}} - \dot{q}^{cond}_{s,i,j+\frac{1}{2}} + V_{i,j}(Q_{s,source,i,j} - Q_{s,sat,i,j} - Q_{s,g,i,j} - Q_{s,l,i,j}) \quad (2\text{-}42)$$

Terms at cell faces such as $\dot{q}_{i-\frac{1}{2},j}$ encompass the convective enthalpy fluxes $\dot{q}^{conv}_{i-\frac{1}{2},j}$ related to the mass transport and the conductive fluxes $\dot{q}^{cond}_{i-\frac{1}{2},j}$:

$$\dot{q}_{i-\frac{1}{2},j} = \dot{q}^{conv}_{i-\frac{1}{2},j} + \dot{q}^{cond}_{i-\frac{1}{2},j} \quad (2\text{-}43)$$

Different options for the computation of these terms can be found in Appendix-E.

2.3.2 Unstructured meshing

A version of the MEWA module, using an unstructured staggered grid was developed by Hartmann [60]. The grid can be either automatically generated from a library package (meshing generator Pardiso by Intel) or transposed from a previously created structured meshing. In the latter case, the grid can be orthogonal and regular, like a structured grid, but will be defined and stored totally differently. In this version, all the existing nodes (i.e. cell vertices) are stored into a node list and are defined by their position (i.e coordinates). Cell faces are defined by their vertices and their edges, i.e. the junctions between vertices. Finally, control volumes are defined by the faces that bounded them. By generating from a structured grid, the computed coordinates of nodes, which are basically the intersections of grid lines, are simply copied and stored into the

node list. Vertices, edges, faces and cells are no more indexed by *(i,j)* but simply by a unique index number and stored respectively in a Vertex list *(Vertex1, Vertex2,…Vertexn)*, Edge list *(Edge1, Edge2,…Edgen)*, Face list *(Face1, Face2,…Facen)* and Cell list *(Cell1, Cell2,…Celln)*.

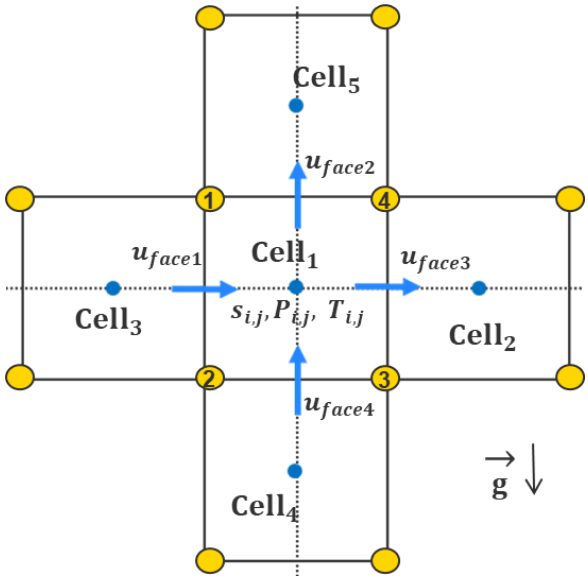

Figure 8 : unstructured meshing obtained from the structured grid (Figure 7)

In a general way, this kind of meshing enables the generation of irregular non-orthogonal grid. Benefits from this will be explained later on. Regarding irregular cells, one does not refer anymore to their cell centre, but rather to their centroid, that has to be found. Face normal, and so the associated velocity vectors, may also be directed in other direction than in the standard cylindrical/Cartesian axis directions. Therefore, the approach, seen in the previous section, for the calculation of the velocities, consisting in using two momentum equations for velocities in the radial and axial directions makes no sense, when using unstructured grid. Instead, only one momentum equation is required for each phase, depending on the normal of the face. This normal will namely determine the contribution of the gravity term. Another main difference for the equation discretization lays in the expression of the pressure gradient. In a structured grid, the pressure of each cell is defined at the centre. The pressure gradient between two cells being basically the ratio of the pressure difference on the distance of the cell centres. In a regular cylindrical grid, the axial or radial distance between two cell centres is very simple to determine. However in an unstructured grid, pressure gradients are harder to define. COCOMO-3D

considers then the pressure at the cell centroid. From this, the pressure gradient between two neighbour cells is considered as the ratio of the pressure difference on a projected distance perpendicular to the considered face, as depicted on Figure 9. In other words, centroid position, as well as face normal, are needed for the calculation of the pressure gradient.

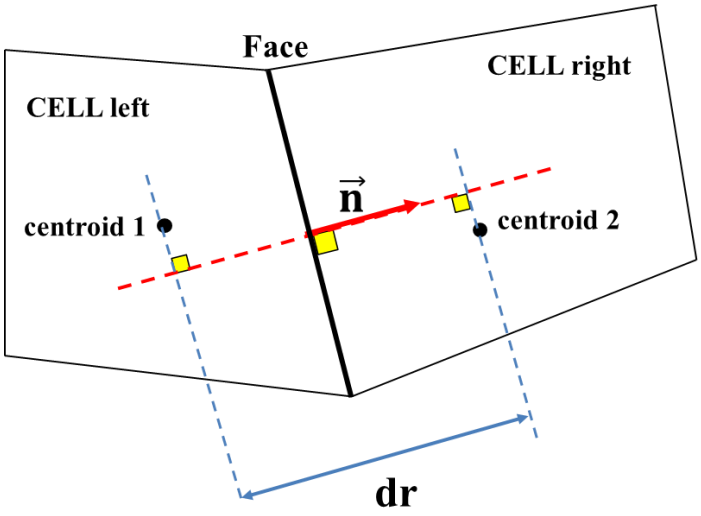

Figure 9 : Definition of the normal vector of the face common to two cells and projected distance between two centroids

For each cell *i*, the discrete mass conservation equations for gas and liquid have the following form:

$$V_i \frac{(\varepsilon s_g \rho_g)_i - (\varepsilon s_g \rho_g)^{old}{}_i}{\Delta t} = \sum_{j=0}^{\text{nbr of faces}} \dot{m}_{g,j} + V_i \cdot \Gamma_i^{evap} \tag{2-44}$$

$$V_i \frac{(\varepsilon s_l \rho_l)_i - (\varepsilon s_l \rho_l)^{old}{}_i}{\Delta t} = \sum_{j=0}^{\text{nbr of faces}} \dot{m}_{l,j} - V_i \cdot \Gamma_i^{evap} \tag{2-45}$$

With

$$\dot{m}_{k,j} = A_j \langle \rho_k \rangle_j \langle \varepsilon \rangle_j \langle s_k \rangle_j u_{k,j} \,, \tag{2-46}$$

for phase *k*= *g*,*l* and at the face *j*.

For each face j, the discretized momentum conservation equations for gas and liquid have the forms (2-47) and (2-48). p_{right} and p_{left} refers to the pressures of the cells having this face in common. By convention in COCOMO-3D, the cell that the face normal is pointing to, is defined as the "right" cell, while the other one is the "left" cell (see Figure 9)

$$\langle K_{gs}^{lam}\rangle_j\, u_{g,j} + \langle K_{gs}^{turb}\rangle_j \langle|\overrightarrow{w_g}|\rangle_j\, u_{g,j} + \langle\frac{K_{gl}^{lam}}{s_g}\rangle_j \left(u_{g,j} - u_{l,j}\right) + \langle\frac{K_{gl}^{turb}}{s_g}\rangle_j \ \langle|\overrightarrow{w_g} - \overrightarrow{w_l}|\rangle_j \left(u_{g,j} - u_{l,j}\right) = -\frac{p_{g,right} - p_{g,left}}{dr} - \vec{g}\cdot\vec{n}\cdot\langle\rho_g\rangle_j \tag{2-47}$$

$$\langle K_{ls}^{lam}\rangle_j\, u_{l,j} + \langle K_{ls}^{turb}\rangle_j \langle|\overrightarrow{w_l}|\rangle_j\, u_{l,j} - \langle\frac{K_{gl}^{lam}}{s_l}\rangle_j \left(u_{g,j} - u_{l,j}\right) - \langle\frac{K_{gl}^{turb}}{s_l}\rangle_j \ \langle|\overrightarrow{w_g} - \overrightarrow{w_l}|\rangle_j \left(u_{g,j} - u_{l,j}\right) = -\frac{p_{l,right} - p_{l,left}}{dr} - \vec{g}\cdot\vec{n}\cdot\langle\rho_l\rangle_j \tag{2-48}$$

Finally, for each cell *i*, the discretized energy conservation equations for gas and liquid have the following form:

$$V_i \frac{\left(\varepsilon s_g \rho_g e_g\right)_i - \left(\varepsilon s_g \rho_g e_g\right)^{old}{}_i}{\Delta t} = \sum_{j=0}^{\text{nbr of faces}} \dot{q}_{g,j} + V_i\left(Q_{s,g,i} + Q_{l,g,i} + Q_{sat,g,i} + \Gamma_i^{evap} i_{g,sat,i}\right) \tag{2-49}$$

$$V_i \frac{(\varepsilon s_l \rho_l e_l)_i - (\varepsilon s_l \rho_l e_l)^{old}{}_i}{\Delta t} = \sum_{j=0}^{\text{nbr of faces}} \dot{q}_{l,j} + V_i\left(Q_{s,l,i} - Q_{l,g,i} + Q_{sat,l,i} - \Gamma_i^{evap} i_{l,sat,i}\right) \tag{2-50}$$

$$V_i \frac{\left((1-\varepsilon)\rho_s e_s\right)_i - \left((1-\varepsilon)\rho_s e_s\right)^{old}{}_i}{\Delta t} = \sum_{j=0}^{\text{nbr of faces}} \dot{q}_{s,j}^{cond} + V_i(Q_{s,source} - Q_{s,sat} - Q_{s,g} - Q_{s,l}) \tag{2-51}$$

Computation of surface area and cell volume is not trivial, since the vertices of a face may be non-coplanar and so the face may be non-planar. An approximation of area and volume can be computed by triangulation. Details about the computation of surface area and cell volumes can be found in Appendix-D.

2.4 Resolution scheme

A deeper explanation of the resolution process is necessary before going any further in the work. The scheme Figure 10 summarizes the whole procedure during a time step Δt, between a previous time level t^{old} and the new time level *t*, in order to compute the unknowns of the system: gas and liquid velocities, gas pressure (from which liquid pressure can be directly deduced), liquid saturation (s_g being simply (1-s_l)) and finally the temperatures of the three phases.

Steam and water velocity are first calculated at each face of the whole computation domain, by solving the momentum conservation equations with the Newton's iteration method (see MEWA-documentation [66]). In order to solve the equations, values of quantities like the pressure, the saturation, the density, must be guessed. As initial guess, the values found during the resolution of the previous time level are used; since these values are still stored, and not overwritten yet.

Mass flows are derived from velocities. By integrating the mass flows at the boundaries of each cell, and adding the evaporation rate (also deduced from values computed during the previous time level) one estimates the mass residuum from the mass conservation equations. This residuum is the difference between the temporal mass variation and the mass variation yielded by the integration of mass flows. For example, for the gaseous phase:

$$\mathrm{Resi}_{\mathrm{g}}^{\mathrm{mass}} = \frac{\mathrm{m}_{\mathrm{g,i}} - \mathrm{m}_{\mathrm{g,i}}^{\mathrm{old}}}{\Delta \mathrm{t}} - \left(\sum_{\mathrm{j=0}}^{\mathrm{nbr\ of\ faces}} \dot{\mathrm{m}}_{\mathrm{g,j}} + \mathrm{V_i} \cdot \Gamma_{\mathrm{i}}^{\mathrm{evap}} \right) \tag{2-52}$$

m_i^{old} is basically the mass computed during the resolution of the previous time level. It should be stressed here that the mass of the new time level is not known yet and will be found iteratively. In other words, an initial guess is required for the value of m_i, too. As an initial guess for m_i, the mass computed during the resolution of the previous time level is taken again. Therefore, during the very first iteration of the whole resolution loop: $m_i - m_i^{old} = 0$.

The unknowns p_g and s_l must be calculated by solving the mass conservation equation for steam and water. That is, new steam pressure and liquid saturation must be found, such that the mass

residuum of steam and liquid are equal to 0, in order to respect the conservation law regarding the mass balance. However, pressure and saturation do not appear explicitly in the mass conservation equation. For this reason, mass flow must be first linearized with respect to pressure and saturation. Afterwards the system can be solved by applying the Newton's method. More details about the resolution methods are available in the MEWA documentation [66] or in the work of Buck [77].

From this, material properties, as well as steam and water mass, are updated. Thereafter velocities are also updated by solving again the momentum equations (analogue to the first step), but taking into account these newly updated quantities (new pressure, new volume fractions…). Subsequently, mass residuum for mass and steam can be newly estimated, using the re-calculated mass flows and the evaporation rate.

After having estimated all the heat transfers with the debris bed ($Q_{s,sat}, Q_{s,g}, Q_{s,l}$), as well as the conductive heat flow, and knowing the source term $Q_{s,source}$ from the setting of the boundary conditions, energy residuum of the solid phase can be calculated. This residuum is the difference between the temporal variation of the internal energy and the energy variation yielded by the integration of all the conductive and convective heat transfers, as well as all the volume related heat transfers, that is $Q_{s,sat}, Q_{s,g}$ and $Q_{s,l}$. $E_s^{old}$is the internal energy of the solid phase computed during the previous time level, while E_s is computed with the current mass (which is the same as the initial mass, because no mass transport is assumed for the solid phase) and the current specific internal energy e_s, which is function of the particle temperature. Of course, as an initial guess for E_s , the internal energy computed during the resolution of the previous time level is taken. Thus, during the first iteration of the resolution loop: $E_{s,i} - E_{s,i}^{old} = 0$.

$$\mathrm{Resi}_{\mathrm{s}}^{\mathrm{energy}} = \frac{\overbrace{(\mathrm{m_s e_s})_{\mathrm{i}}}^{E_{s,i}} - \overbrace{(\mathrm{m_s e_s})_{\mathrm{i}}^{\mathrm{old}}}^{\mathrm{E_{s,i}^{old}}}}{\Delta \mathrm{t}} - \left(\sum_{\mathrm{j}=0}^{\mathrm{nbr\ of\ faces}} \dot{\mathrm{q}}_{\mathrm{s,j}}^{\mathrm{cond}} + \mathrm{V_i}\left(\mathrm{Q_{s,source}} - \mathrm{Q_{s,sat}} - \mathrm{Q_{s,g}} - \mathrm{Q_{s,l}}\right) \right) \tag{2-53}$$

Similarly, energy residuum of steam and water are also estimated, taking into account all the volume related heat transfers, but also the enthalpy fluxes, yielded by the mass transport at the cell boundaries. Moreover, in order to avoid an accumulation of numerical error, the energy from the mass excess (mass residuum) is subtracted, as a numerical heat loss.

$$\mathrm{Resi}_g^{\mathrm{energy}} = \frac{\left(m_g e_g\right)_i - \left(m_g e_g\right)_i^{\mathrm{old}}}{\Delta t} - \left(\sum_{j=0}^{\text{nbr of faces}} \dot{q}_{g,j} + V_i\left(Q_{s,g,i} + Q_{l,g,i} + Q_{sat,g,i} + \Gamma_i^{\mathrm{evap}} i_{g,sat,i}\right) - \mathrm{Resi}_g^{\mathrm{mass}} i_{g,i} \right) \tag{2-54}$$

$$\mathrm{Resi}_l^{\mathrm{energy}} = \frac{\left(m_l e_l\right)_i - \left(m_l e_l\right)_i^{\mathrm{old}}}{\Delta t} - \left(\sum_{j=0}^{\text{nbr of faces}} \dot{q}_{l,j} + V_i\left(Q_{s,l,i} - Q_{l,g,i} + Q_{sat,l,i} - \Gamma_i^{\mathrm{evap}} i_{l,sat,i}\right) - \mathrm{Resi}_l^{\mathrm{mass}} i_{l,i} \right) \tag{2-55}$$

After having linearized these energy conservation equations with respect to the particle temperatures, steam temperature and water temperature, one can solve the system and find the unknowns: T_s, T_g and T_l. Afterwards, with these new temperatures, the materials properties can be updated again, as well as the mass.

The whole scheme is repeated until the values for pressures, volumes fractions, temperatures and mass converge, with a tolerance of 10^{-5} for each parameter. As soon as the convergence is reached, the obtained values can be stored as “old” values for the resolution of the next time level.

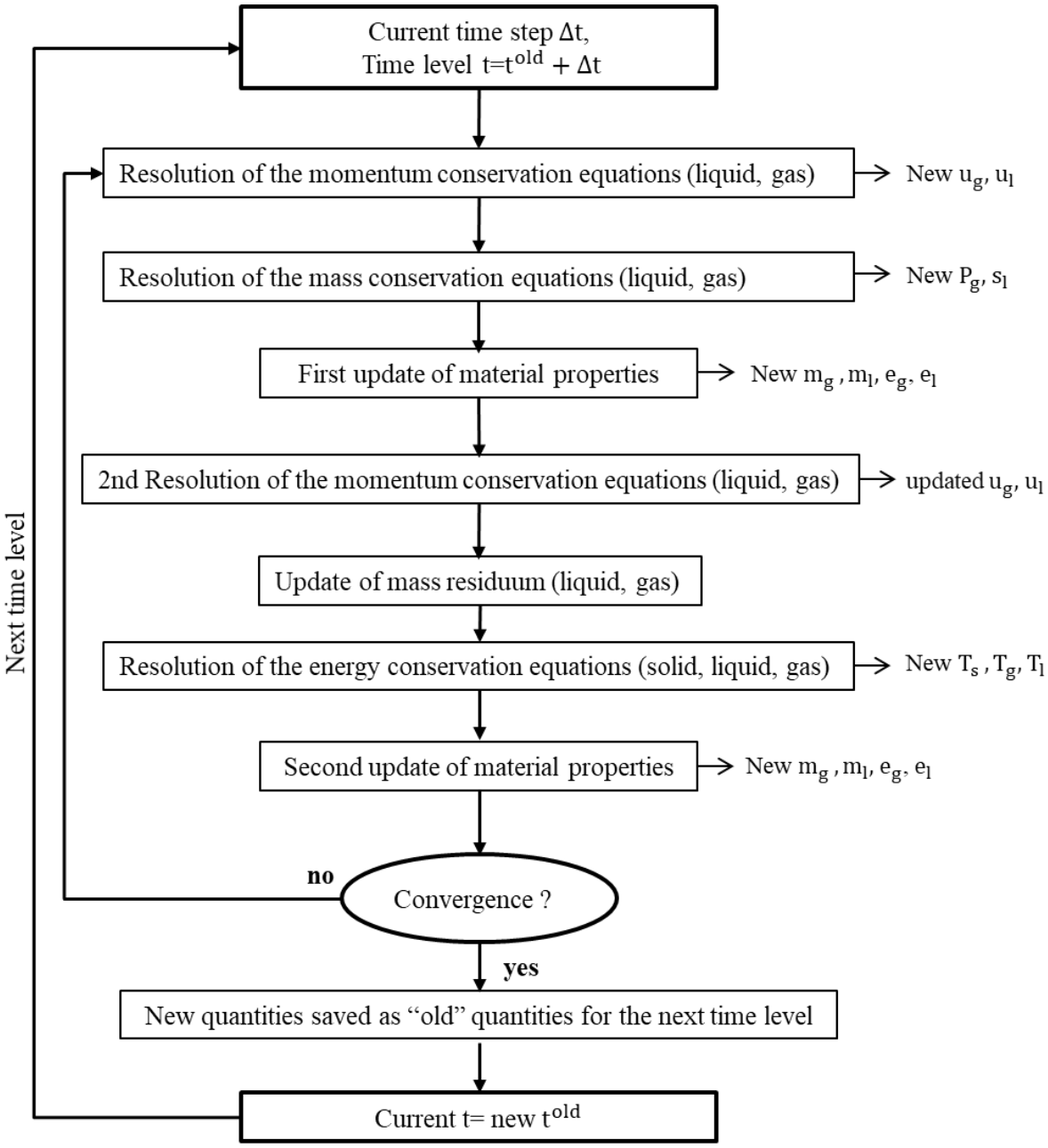

Figure 10 : Resolution pattern of the current version of COCOMO-3D

3 Validation

The modelling of COCOMO-3D was assessed against a validation matrix namely based on outcomes from COOLOCE and DEBRIS [58]. In the coming sections, COCOMO-3D capabilities are assessed, focusing mainly on the specific problem of bottom-flooding. First, an assessment based on a 1D simulation of the DEBRIS experiments (scaled down debris bed), featuring a fixed injection rate via a pump or a gravity-driven injection, will be presented. Secondly, 2D simulations of the large-scale facility PEARL will test the capability of COCOMO-3D in dealing with 2D-effects (PEARL is equipped with a by-pass). Then, the simulation of a much larger debris bed (reactor-scale) will enable the use of coarse meshing, yielding large cells typically used in integral codes such as ASTEC. But before showing any results, a definition of the quench front is needed.

3.1 Quench front definition

For his observation on the DEBRIS test facility, Leininger [51] depicted the quench region into four zones (see Figure 11), inspired from the representation of the work of Bachrata et al. [78]. The zones are separated by three fronts:

- The water front: where the bed temperature is at saturation. Under the water front is the bed slightly under the saturation, because of the presence of sub-cooled water. The flow is monophasic (water).
- The quench front: where the bed is slightly above T_{sat}, while the fluid is exactly at T_{sat}. in the zone between the quench front and the water front occurs a light nucleate boiling. A two-phase flow is considered.
- The flood front is reached, as void fraction is 1.0. Between the quench front and flood front, occur strong boiling processes, such as film boiling. Above the flood front, only super-heated steam is to be found; the flow is monophasic (steam).

If the injection flow is slow enough, zone 2 (on Figure 11) may be so thin that the quench front and the water front cannot be distinguished.

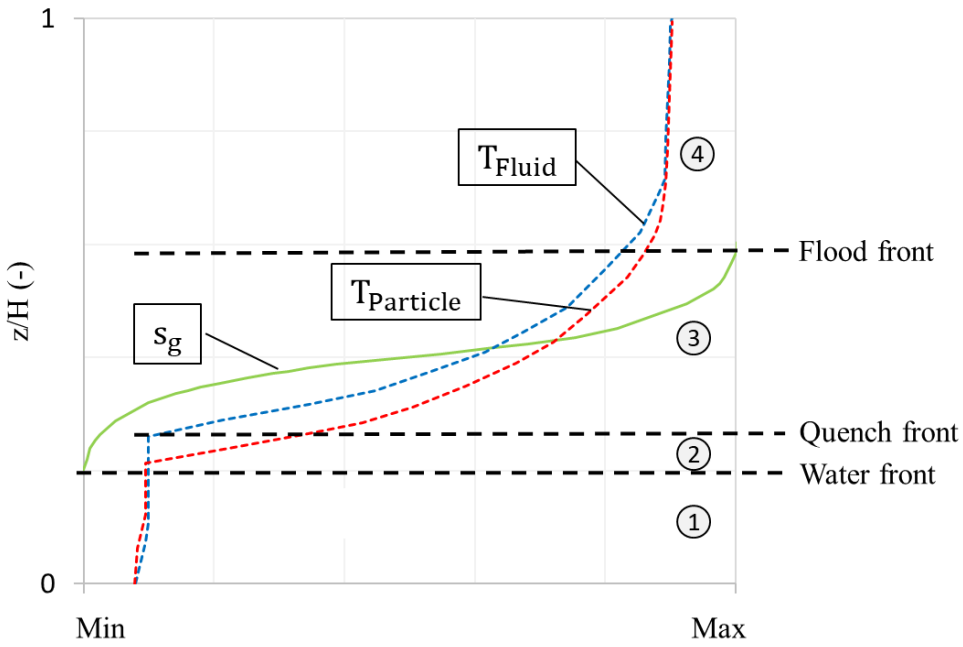

Figure 11 : Representation of the different zones of the quench region, for a dry particle bed flooded from the bottom (referring to [51]); s_g being the void fraction in pores

In the literature other partitioning of the zones of the quench region and of their limits may be found (for instance, in [78] and [43]), but generally the quench front is tracked through the local particle temperature, and thus located where particles are slightly above the saturation temperature. According to that, saturation temperature will be taken as reference for the tracking of the quench front in the present work.

3.2 Simulation of DEBRIS

3.2.1 DEBRIS test facility

A schematic view of the DEBRIS test facility can be seen on Figure 12 from the work of Rashid [45].

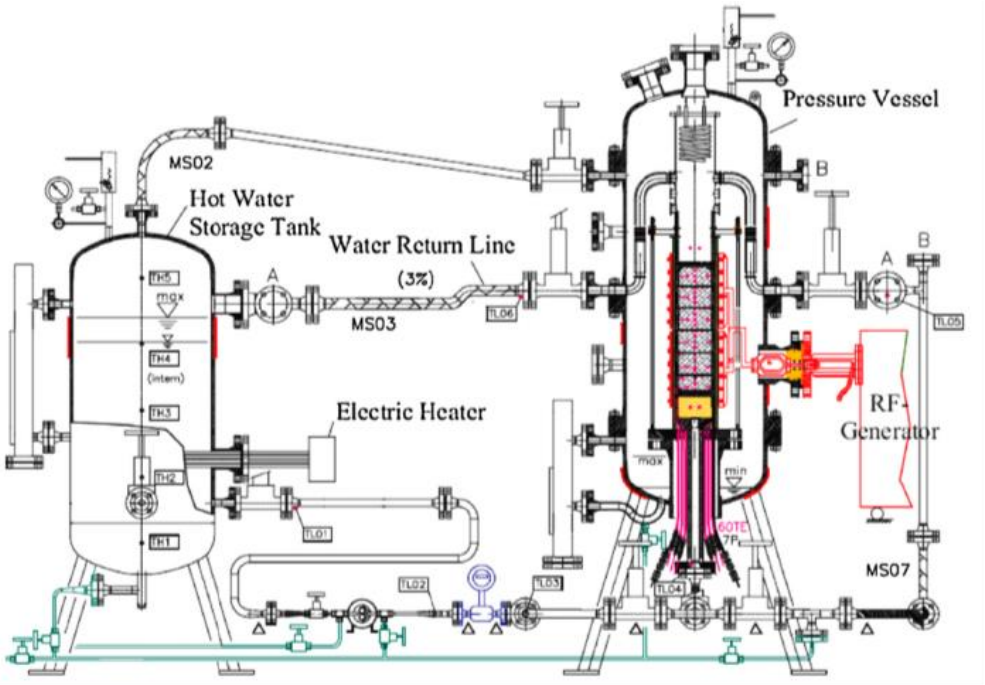

Figure 12 : DEBRIS test facility (from [45])

It consists in a particle bed contained in a crucible; the crucible is also enclosed in a pressurized vessel, which gave the possibility to carry out tests under different system pressures. The particle bed can be volumetrically heated via an oil-cooled two-winding induction coil onto the crucible. This induction coil is connected to an RF-generator (frequency: 200 kHz, nominal output power: 140 kW). Controlled water injection (setting of mass flow) can be ensured at the bottom or the top of the bed, with water coming from a tank connected to the vessel (tank on the left on Figure 12).The water supply allows also for submerging the bed entirely in order to carry out boiling tests. Moreover, one of the main features of this facility is the possibility to supply water by "gravity-driven" injection. In this case, the water is no longer defined by a fixed mass flow, but driven by the water head at the crucible inlet. This head is yielded by the water column, the height difference between the inlet elevation and the water level elevation inside the tank, (not the same tank, that the one used for fixed mass flow), like depicted on Figure 13.

The current work focuses on the quench test with bottom-injection only (top-flooding not activated). The crucible is the one depicted on Figure 13. As for the composition of debris bed, spherical particles made of stainless steel were used. The particles have different sizes, with respect to the following diameter distribution: 20% of 2 mm, 30% of 3 mm and 50% of 6 mm;

yielding an average porosity of 0.37. With this set of particles, a 640 mm-high polydispersed bed with an inner diameter of 150 mm is built inside the crucible. The system pressure in the crucible is set to 1 bar, and a pre-heating phase was initiated until the bed reaches temperatures in the range of 400-700°C. Once these initial temperatures are met, the cold water (20°C) is injected at the bottom by gravity with an initial hydrostatic head of 950 mm.

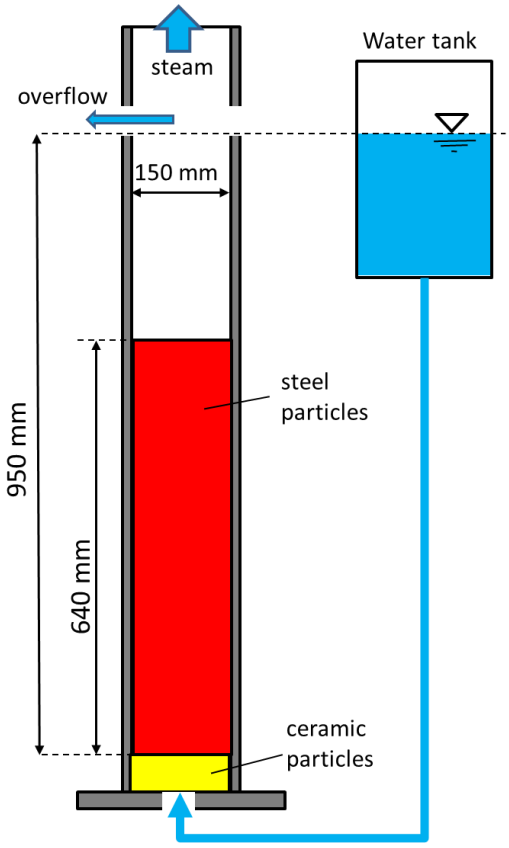

Figure 13 : DEBRIS quench-test, with bottom gravity-driven injection

Unlike injections with constant mass rates, this kind of injection depends on the pressure inside the bed, and so on the phenomena occurring in the bed during the quenching, i.e. frictions (inertial, viscous and interfacial) and boiling (steam generation, making the local steam fraction increase). Thus, the use of such tests allows for a more extensive assessment of the friction models. Thermocouples introduced in the pores along the bed height, in three radial regions (central, mid-radial and near the wall) gave information on the axial and radial temperature profile evolutions during the quenching and allowed for the tracking of the quench front.

3.2.2 Reproduction of DEBRIS with COCOMO-3D

The whole inner domain of the crucible (debris bed + region above and under the bed) was reproduced with the standard structured version of COCOMO-3D. The specific region corresponding to the debris bed was defined as a porous domain. The setting of the bed geometry was directly based on the experimental dimensions (height: 640 mm; radius: 75 mm). In the experiment it appeared that the quench front does not seem to be impacted by the so-called wall effect: the higher porosity at the wall vicinity as well as the heat loss through the wall that should occur in such configuration had a negligible effect on the water velocity. As a matter of fact, the quench front remained radially quite uniform. Subsequently it simplified the simulation in two ways. Firstly, the heat loss towards the vessel wall being negligible, reproduction of the crucible wall is not necessary. Secondly, the resulting uniform quench form reduces the study to a one-dimensional simulation. Thus, the bed is discretized axially only. From the particle size distribution, one can estimate the effective particle diameter. This parameter is namely important for the friction calculation. An effective diameter of 2.9 mm has been found by using the Ergun's law and measurements of the single phase pressure drop in the debris bed (approach exposed in the work of Rashid [79]). Concerning the gravity-driven injection, a constant hydrostatic head at the vessel inlet of 950 mm is assumed (tank section large enough and friction along the pipe between the tank and the crucible is neglected) throughout the quenching of the bed. Experimental porosity of 0.37 was applied to the bed domain. The water supply could have been defined by a pressure boundary condition ($P_{inlet} = 109908$ Pa) at the bottom, corresponding to a head of 950 mm, from which the water flow rate was deduced by COCOMO-3D. Otherwise, for former simulations with a fixed injection rate, the mass flow is set as boundary condition at the bottom of the bed.

3.2.3 Simulation results

An emphasis has been set on the quench front velocity within the bed, i.e. its progression. The Figure 14 shows the evolution of the quench front position in the test in which the bed was pre-heated up to 400°C and quenched by gravity-driven injection. The bed was discretized axially

into 12 cells (cell size ~ 5 cm). The blue curve represents the quench front progression of COCOMO-3D, while green dots represents the measures from the related test. In the experiment the bed gets fully quenched (i.e. the quench front reaches the highest bed elevation: z = 640 mm) after 200 s. COCOMO-3D shows a good agreement with the experiment, regardless of a discrepancy of around 40 s. The overestimation of the quench front velocity may be due to the fact that the friction in the junction, i.e. the pressure loss between the water tank and the vessel, was not taken into account in the calculation. Originally performed in the frame of a benchmark for the validation of the ASTEC v2.1.0 code (see [63]), these simulations stressed the necessity to use a model distinguishing the behaviour of steam from this of water regarding in particular the momentum conservation equation, and accounting explicitly for the interfacial friction. The previous model in ASTEC v2.1.0, which considered water and steam as a homogeneous mixture, accounted the momentum balance only for the mixture, yielding a mean velocity. This eventually predicted a significantly slower quenching process, most probably due to an overestimation of the frictions between the phases. It resulted in a full quenching of the bed after 600 s (i.e. 400 s longer than COCOMO-3D predictions).

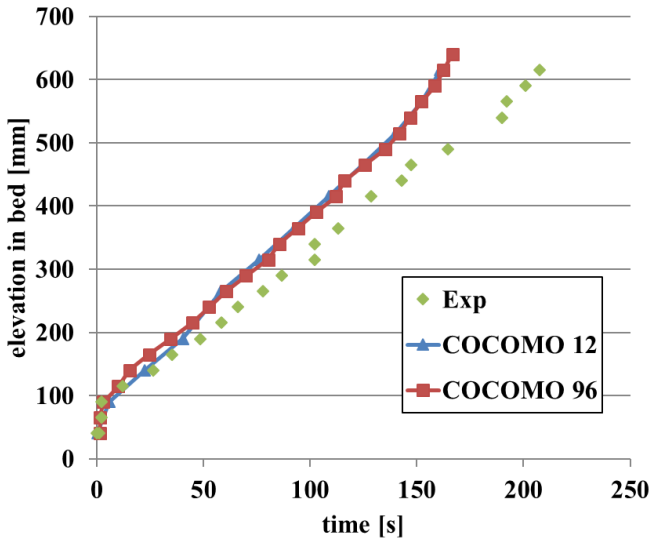

Figure 14 : Axial quench front progression in DEBRIS (T_{ini} = 400°C; gravity-driven injection)

3.2.4 Sensitivity analysis regarding the meshing of the debris bed domain

Preliminary simulations on the same facility were already performed with ASTEC v2.1.0 by D'Alessandro et al. [80], based on tests where the bed was quenched from the bottom by a

constant flow rate of cold water (tests performed by Rashid [79]). Several 1D calculations were carried out with different axial discretizations. It showed that the meshing has an impact on the local steam production, which affects directly the local void fraction and so the local pressure. Yet the overall steam generation throughout the quenching process did not seem to be affected. The modelling of COCOMO-3D leads to the same conclusion. Indeed, COCOMO outcomes (see Figure 15) shows clearly that the discretization barely affects the quench front progression; the blue (bed discretized into 12 cells) and red (bed discretized into 96 cells) curves are perfectly identical, whereas the local pressure throughout the whole quenching process seems definitely influenced by it. Gas pressure at the mid-height of the bed (at 320 mm elevation) is presented on Figure 16. One observes several peaks, which are all related to a strong production of steam. This occurs when water is entering a dry cell. As a consequence, one notices that the numbers of peaks on the graph corresponds to the number of cells. For instance, for the simulation with 12 cells, 12 peaks can be counted (blue curve). According to Figure 17, presenting the accumulation of the mass of steam generated during the quenching, these sudden and abrupt steam productions yield a step-like evolution of the overall steam production. Again, the number of steps matches with the number of cells. In spite of its effect on steam production, the discretization does not seem to impact the overall production of steam.

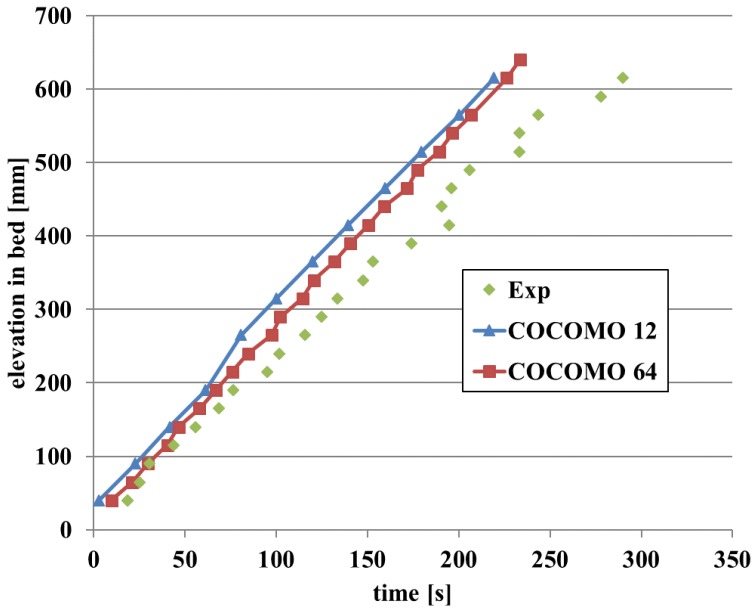

Figure 15 : Axial quench front progression in DEBRIS (T_{ini} = 400°C; fixed injection)

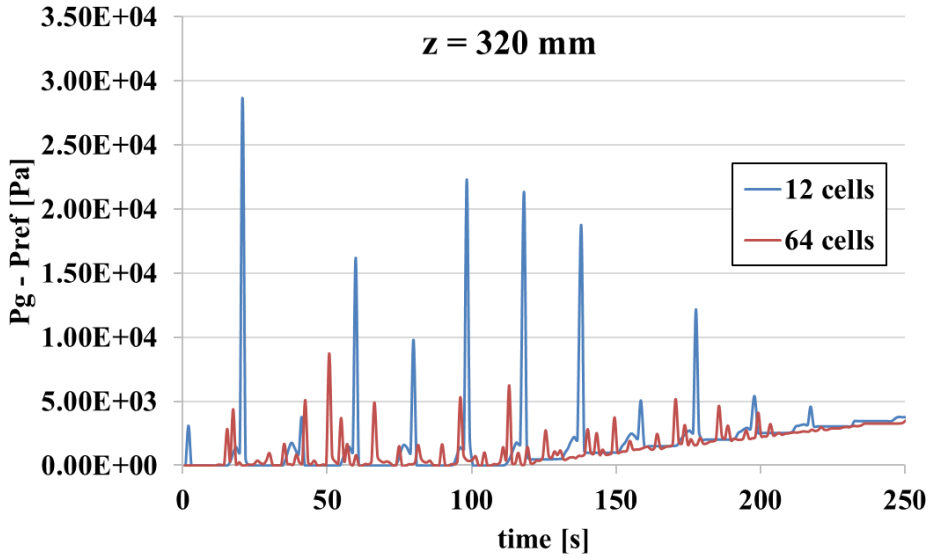

Figure 16 : Gas pressure in debris bed at elevation 320 mm (T_{ini} = 400°C; fixed injection)

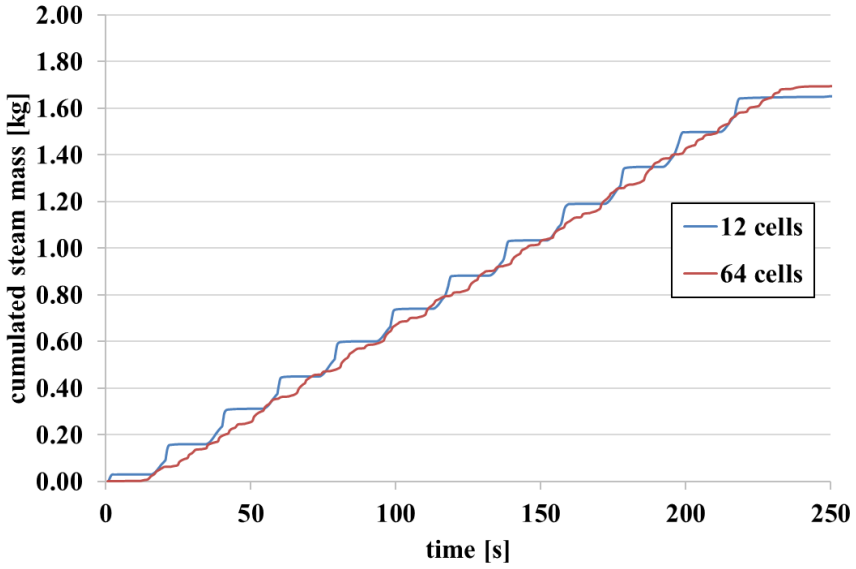

Figure 17 : mass of steam generated over the whole quenching (T_{ini} = 400°C; fixed injection)

When using a gravity-driven injection, the flow rate depends on the initial hydrostatic head, but also on the friction and pressure within the bed. As already mentioned above, for this kind of injection, not only the boundary conditions determine the flow rate calculation, but also the feedback from the processes occurring inside the bed during the quenching. It seems natural to think that the flow rate at the bed inlet should be affected by the meshing, since this flow rate depends on the local pressure in the bed. Surprisingly, Figure 14 shows that the quench front does not seem to be impacted that much by the meshing. While, according to Figure 18, the

simulations performed with a fine and coarse meshing predict different evolution of the local pressure, and so of the overall mass of injected water (Figure 20). It should be remarked that in the simulation with 12 cells, 50% less water was required to submerge the bed (totally reflooded after ~ 160 s) than in the simulation with 96 cells. It appears also that even the influence on water injection does not impact the steam generation in Figure 19. It may be due to the fact that the facility is scaled-down (bed is 64 cm-high) and the cells are still too small (~ 0.5 - 5.0 cm), to show any influence of the discretization. Results from the others DEBRIS simulations are in Appendix-G. At this point, it must be reminded that integral codes such as ASTEC may not consume too much CPU-time, especially when they are used as emergency tool. In such calculations, cells are typically bigger (in the order of 20 cm) than the ones generated in the presented DEBRIS test simulations.

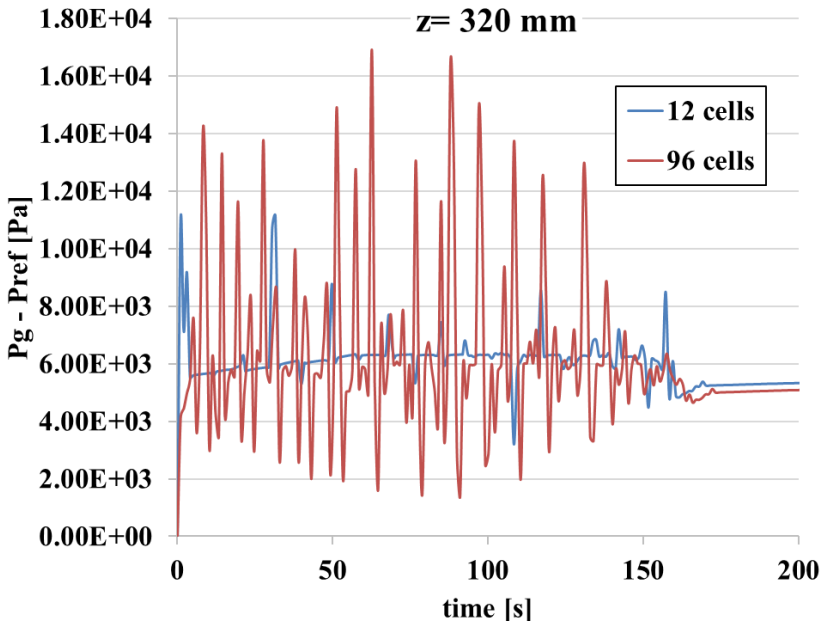

Figure 18 : Gas pressure in debris bed at elevation 320 mm (T_{ini} = 400°C; gravity-driven injection)

In the section 3.4, the sensitivity of the COCOMO-3D results regarding the meshing for a reactor-scale debris bed will be tested. Nevertheless, before that, capability of COCOMO-3D in reproducing multidimensional effects on a larger bed will be assessed based on the PEARL experiments.

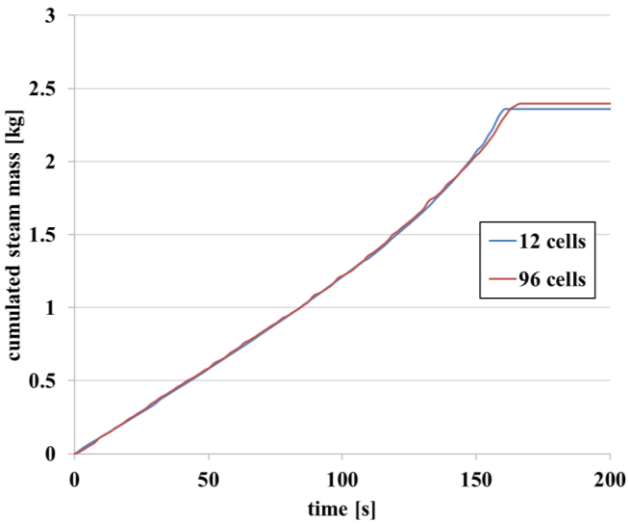

Figure 19 : mass of steam generated over the whole quenching (T_{ini} = 400°C; gravity-driven injection)

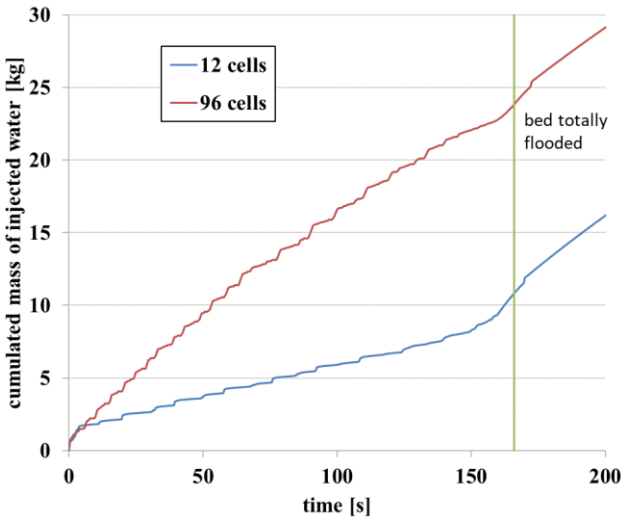

Figure 20 : mass of water injected over the whole quenching (T_{ini} = 400°C; gravity-driven injection)

3.3 Simulations of the PEARL experiments

COCOMO capabilities regarding the 2D behaviour of quenching has been confronted to the large scale experiment PEARL (Chikhi et al. [81,82]). PEARL has been designed and performed by IRSN Cadarache, France. It consists in a hot debris bed, surrounded by a by-pass region (region with a higher porosity). Cold water is injected from the bottom or the top, in order to cool down the debris bed and the by-pass. Quench front progression through the bed, as well as the steam production, was investigated. Moreover, a special emphasis has been set on the flow patterns of water and steam, which may be influenced by the presence of the by-pass under certain conditions.

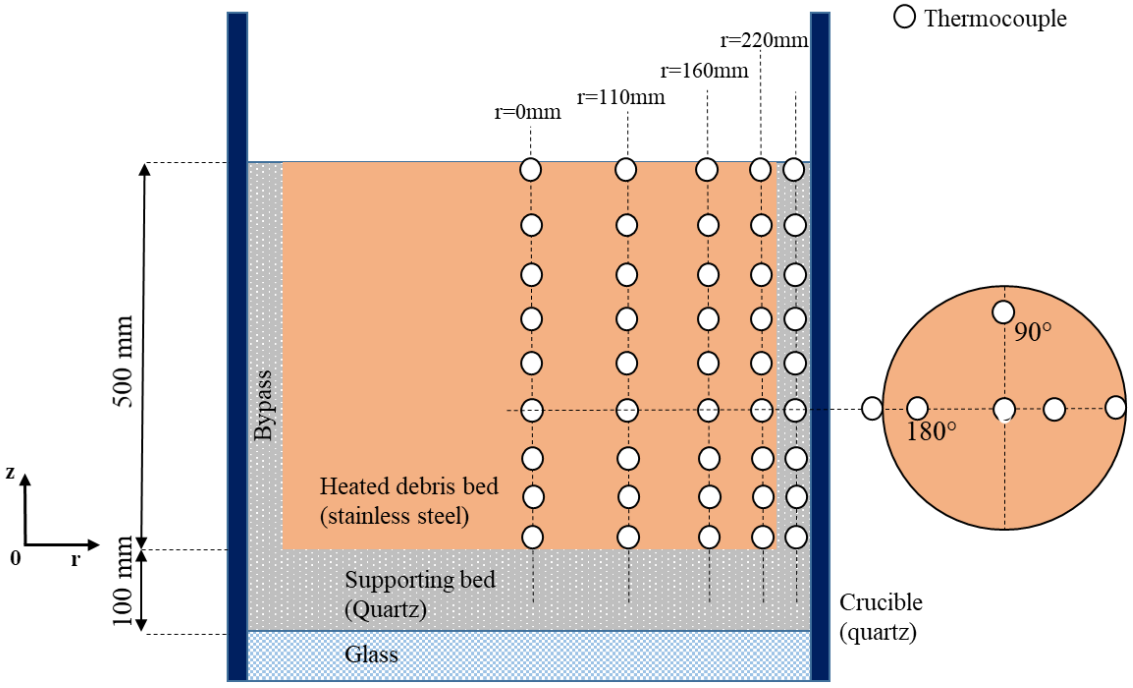

Figure 21: Schematic view of the PEARL facility

3.3.1 PEARL facility

The test section (Figure 21) is composed of a 2.6 m-long quartz tube, with an inner diameter of 540 mm, and thickness of 10 mm. Contained in the tube, the cylindrical debris bed is approximately 500 mm-high, with a diameter of 450 mm; it is made of 4 mm stainless steel balls that are heated by an induction coil linked to a high frequency generator. The bed is surrounded by the by-pass made of 8 mm quartz balls (yielding therefore a higher porosity). A 100 mm-high bed, consisting of quartz balls, is supporting the experimental debris bed, so that it is well positioned with respect to the induction coil position. The whole is enclosed in a pressurized containment. Pressures from 1 up to 10 bar can be set in the system. The bed is equipped with thermocouples at different radial, axial and azimuthal positions, as shown on Figure 21.

3.3.2 Test conduct

The quenching of the experimental bed has been performed under different initial bed temperatures, different system pressures and with different injection rates.

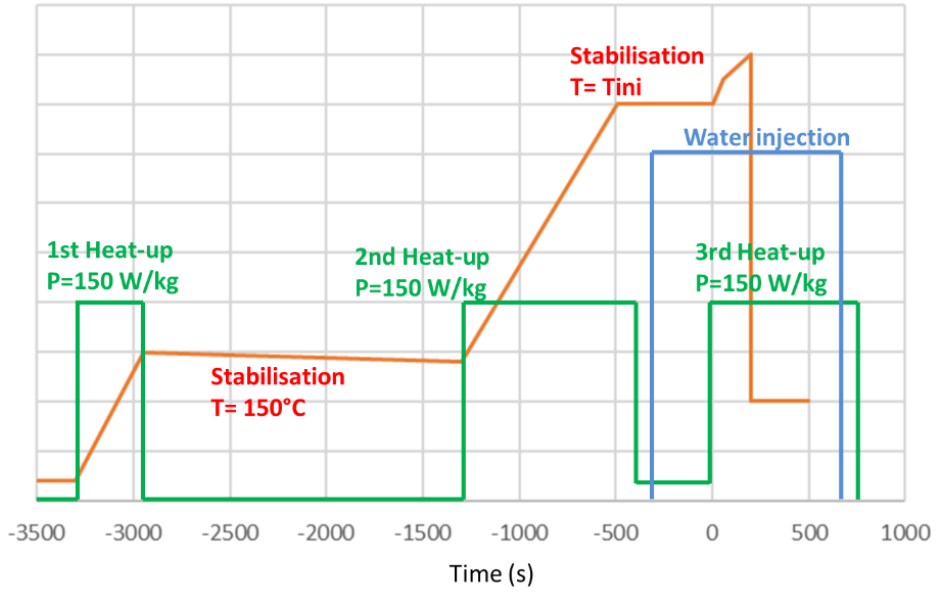

Figure 22 : Set-up of heat-up, bed temperature and water injection

The main phases of the test are depicted on Figure 22. First, an approximately 20 kg/s flow rate of 120 °C steam is injected through the test section from the bottom, in order to heat up the by-pass balls (unlike stainless steel balls, it cannot be heated up by induction). In parallel starts the first inductive heat-up phase of the bed (150 W/kg). When the bed temperature reaches 150 °C, the furnace is stopped, while the steam generator goes on during the stabilization phase, until by-pass ball temperature reaches the saturation temperature. A second heat-up phase is initiated in order to reach the target initial temperature T_{ini} in the experimental bed. Once the target T_{ini} is reached, the furnace is stopped and the water is injected from bottom (with a predefined mass flow rate). Water flows first through the lower quartz bed (support bed). As water penetrates the bottom of the experimental bed, the third heat-up phase is started

3.3.3 COCOMO-3D input

For simplification reasons, only the experimental bed, the by-pass and the lower (supporting) bed were reproduced. The present calculations focus on tests at atmospheric pressure; where only the initial temperature T_{ini} and the injection mass rate were varied (tests PA-0, PA-1, PA-2, PA-4 and PA-5 in Chikhi et al. [81], see Table 2). Like in the experiment, the bed was heated up to

150°C, followed by a stabilization phase. The second heat-up was then applied in order to reach the target T_{ini}. T_{ini} being reached, the heat-up is deactivated and the injection (at wanted mass rate) starts. The heat-up is first re-activated as soon as the presence of vapour is detected (meaning that water is penetrating the hot experimental bed).

First, the bed was discretized into 25 cells axially (axial cell size ~ 2 cm). The bed and the by-pass were radially discretized into 20 and 5 cells respectively (radial cell size ~ 1 cm for both).

Table 2 : experimental set-up of the different tests at 1 bar

Test	Initial temperature (°C)	Injection flowrate (g/s)
PA-0	150	318
PA-1	400	318
PA-2	700	318
PA-4	400	127
PA-5	400	635

3.3.4 PEARL vs. COCOMO results

Concerning the quench front progression, the local temperature was taken as criterion for the tracking of the quench front. Chikhi et al. [81] also assumed that the quench front reaches a thermocouple position when its temperature falls down to the saturation temperature. Since the experiment revealed that the quench front within the bed is more or less uniform (referring to the purple, green, clear blue, brown and dark blue dots on Figure 23, being measures at different radial and azimuthal positions), only the position of quench front at the centre of the bed was considered by COCOMO-3D. For cases PA-1, PA-2 and PA-5 (respectively on Figure 24-(b), Figure 23, Figure 24-(d)) COCOMO-3D predicts a faster cooling, i.e. faster quench front progression, in the by-pass (green curve) than in the experimental bed (blue curve), which is totally consistent with the outcomes of the experiments [81]. Indeed, it was expected that the low porosity of the by-pass and the steam flow tend to drag water into the by-pass region (as already mentioned in section 1.1.2). The faster quench front in the by-pass leads to a water accumulation above the experimental bed, while the latter is not fully quenched. This may cool the upper free surface of the bed. This behaviour was correctly reproduced and can be observed on Figure 23 and Figure 24-(d), where the highest position of the heated bed appears to be cooled before the quench front has even reached it. As for PA-0 and PA-4 (respectively on Figure 24-(a),-(c)), the

by-pass and the bed were cooled with the same velocity, which is also in good agreement with the experiment.

Nevertheless, quantitatively speaking, looking for instance at the test PA-2 (Figure 23), one observes that COCOMO-3D predicts a faster quench front through the bed than in the test, whereas the predicted quench front through the bypass is slower than in the test (see the yellow dots on the figure).

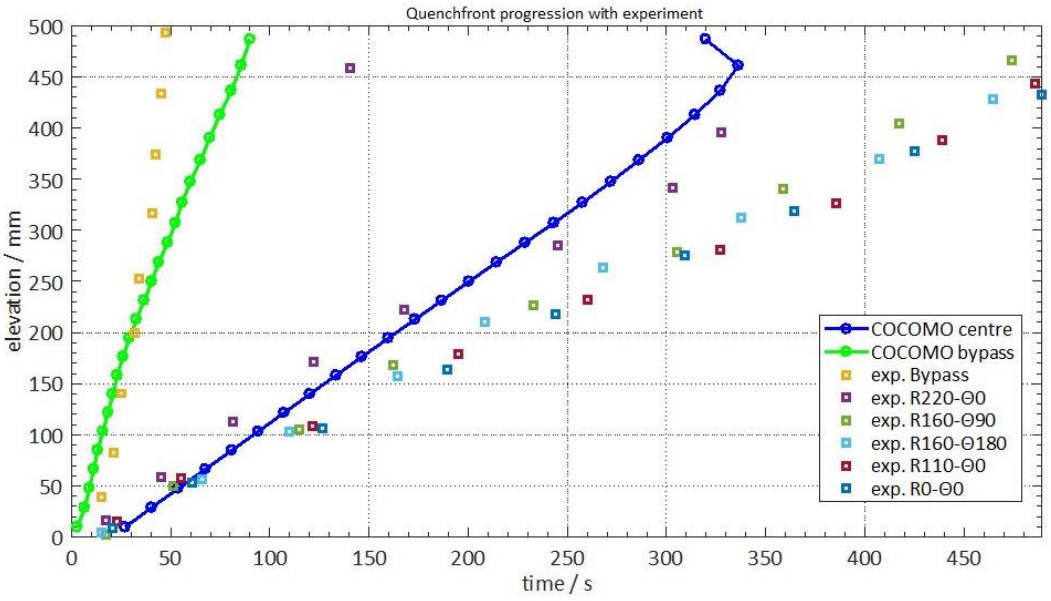

Figure 23 : Quench front progression in PEARL PA-2 test and with COCOMO

(a)

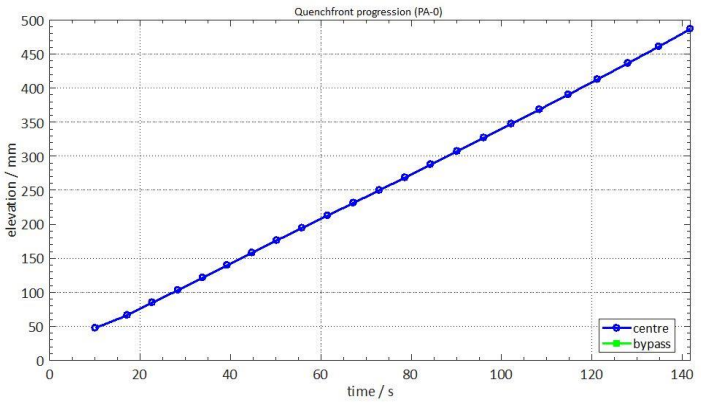

(b)

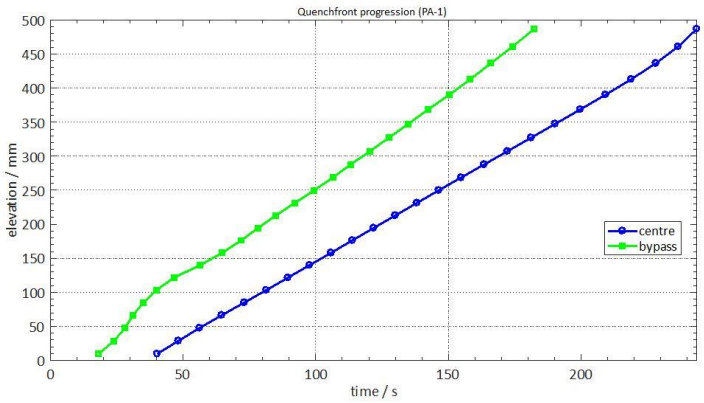

(c)

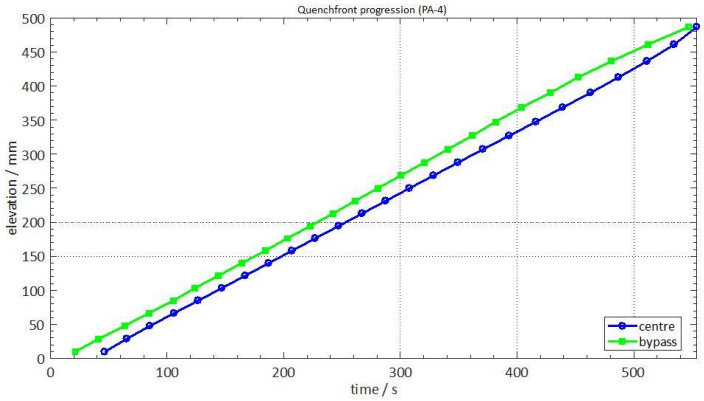

(d)

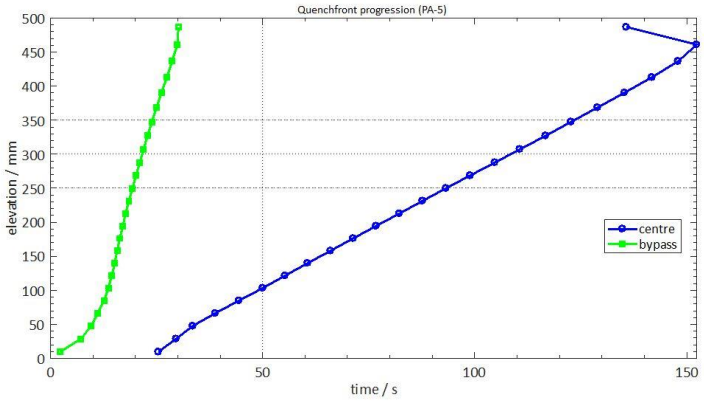

Figure 24 : Quench front progression calculated by COCOMO, for case PA-0, PA-1, PA-4 and PA-5 (fine meshing)

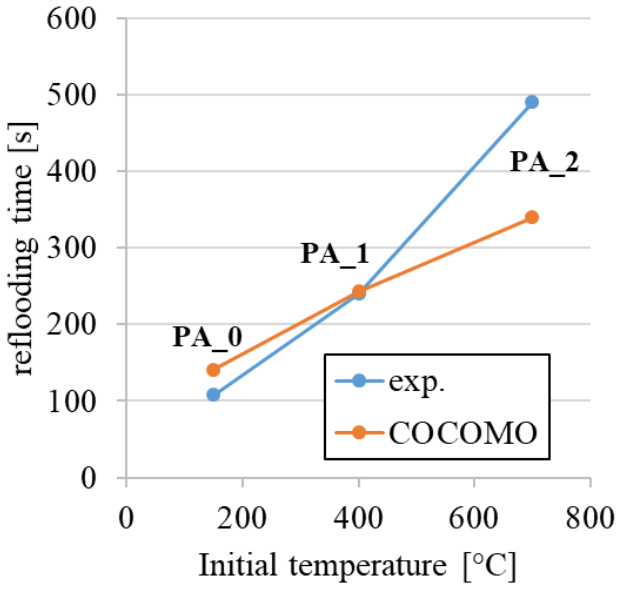

Figure 25 : Reflooding time vs. initial temperature (constant injection rate)

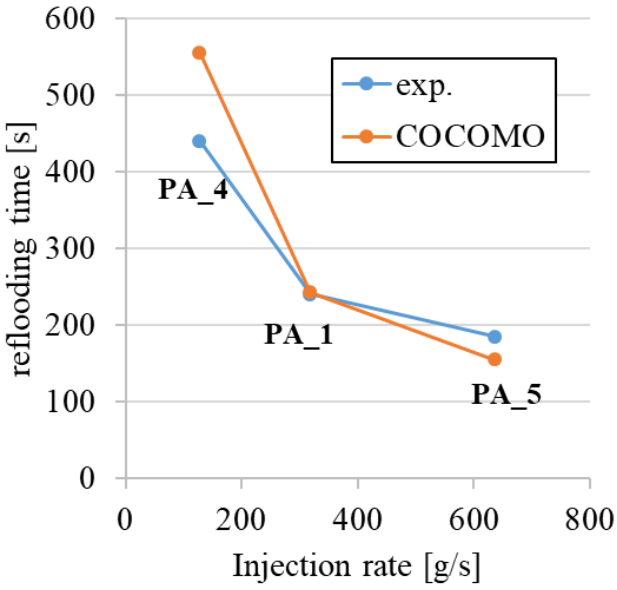

Figure 26 : Reflooding time vs. injection rate (constant initial temperature)

Chikhi and Fichot concluded also that the reflooding time increases with the initial temperature of the debris bed, but inversely decreases by increasing the injection rate. The experimental results are summarized (blue curves) on Figure 25 and Figure 26, showing the influence of the initial temperature and the water injection rate respectively on the reflooding time. This dependency is in general well reproduced by COCOMO-3D (orange curves), in spite of the underestimation of the quench front progression for the case PA-2 already mentioned above.

In order to observe the influence of the meshing on the results, simulations were repeated with a coarser discretization. The bed was then discretized into 6 cells axially (axial cell size ~ 8 cm). The bed and the by-pass were radially discretized into 15 and 3 cells respectively (radial cell size ~ 1.5 cm for both). Quench progression in the hot bed (blue curves) and the by-pass (green curves) for cases PA-0, PA-1, PA-4 and PA-5 are showed on Figure 27-(a),-(b),-(c) and –(d), respectively. While the overall behaviour of the front progression in the bed and in the by-pass remained the same as with the previous fine meshing, one remarks that with a coarse meshing COCOMO-3D predicts in general a slightly faster water progression inside the hot bed (bed totally flooded a dozen of seconds earlier than with the finely discretized bed), and a more noticeable faster progression inside the by-pass (green curves) namely in Figure 27-(b) and –(c) (respectively 50 s and 100 s earlier than with the finely discretized bed).

(a)

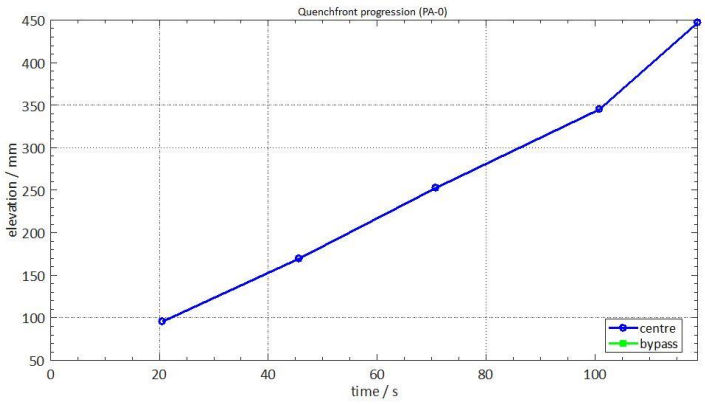

(b)

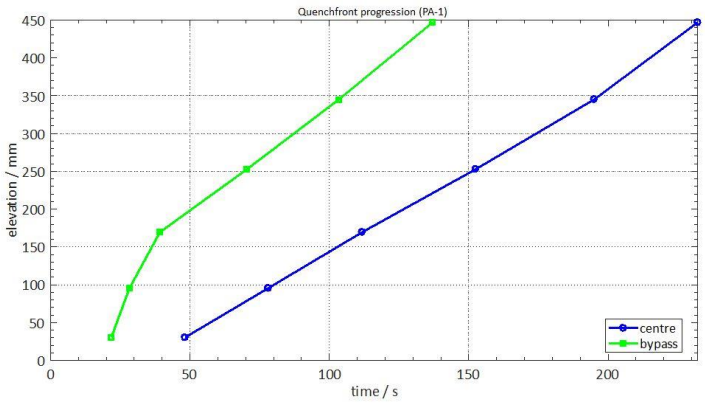

(c)

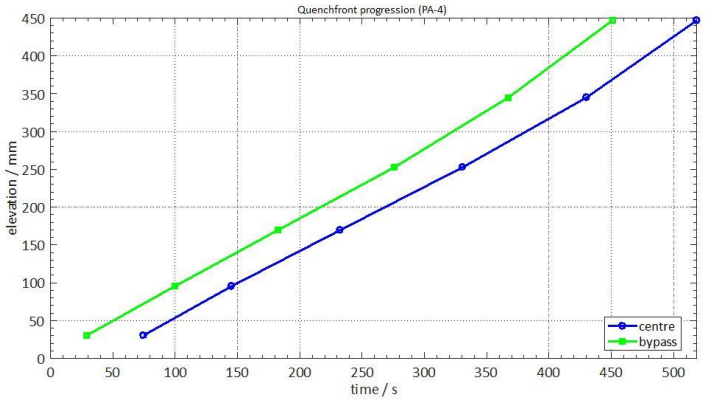

(d)

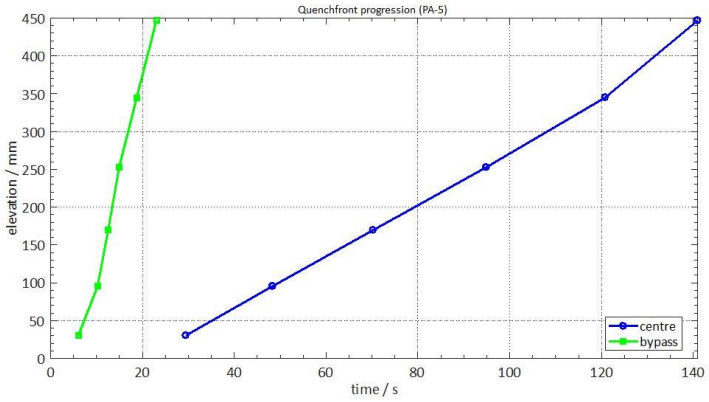

Figure 27 : Quench front progression calculated by COCOMO for cases PA-0, PA-1, PA-4 and PA-5 (coarse meshing)

3.4 Simulation of reactor-scale debris bed

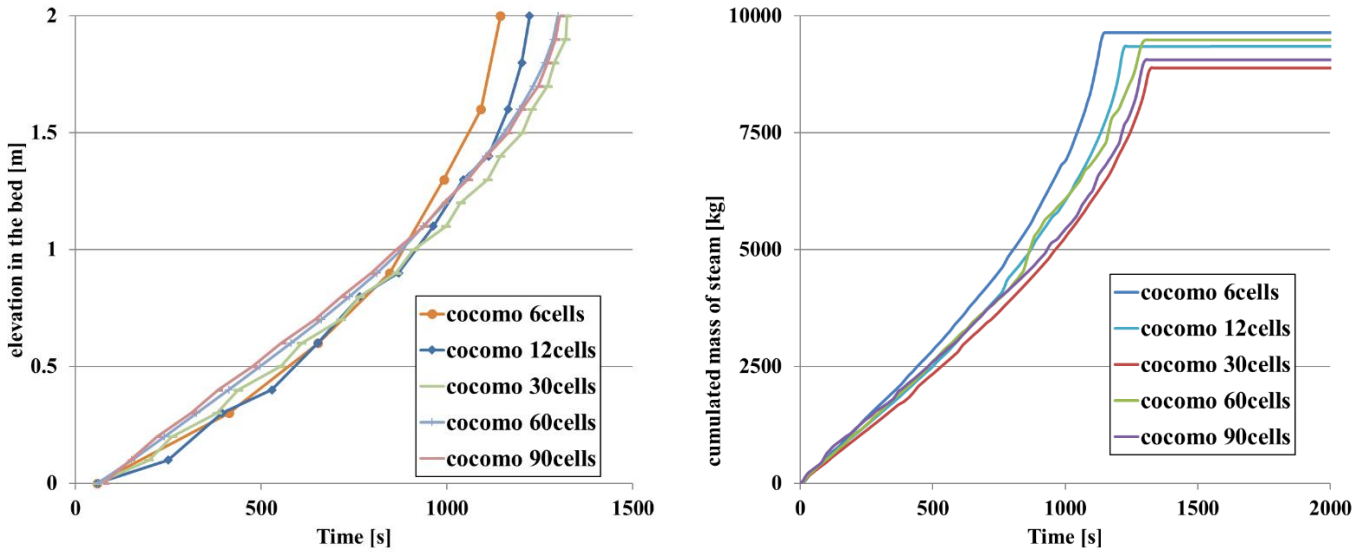

(a) **(b)**

Figure 28 : Quench front progression and Generated mass of steam obtained with different axial discretizations

In order to observe the possible dependence of the quenching simulation upon the discretization for typical reactor calculations, a larger debris bed with a porosity of 40% was reproduced in COCOMO-3D. The bed is 2 m-high and has a radius of 1.54 m (inner diameter of reactor pressure vessel in a NPP of type KONVOI). It is composed of spherical particles made of stainless steel with an effective diameter of 2.9 mm. The size distribution of the particle of the bed is assumed to be similar to the one of the DEBRIS test. The cold water is also assumed to be supplied by gravity-driven injection, as it should be the case by flooding a degraded core from the bottom; water coming from the hot leg flows downwards by gravity (main coolant pumps are switched off; water circulation inside the primary circuit achieved by natural convection) along the downcomer to reach the bottom core plate. Like for the simulation of DEBRIS, injection was simulated by defining a pressure boundary condition at the bottom of the bed. A fixed pressure of approximatively 163000 Pa was set, corresponding to a hydrostatic head of approximately 6 m. An initial temperature of 1400°C has been set uniformly in the bed particles (temperatures that can be found during an severe accident). The system pressure is 1 bar. The quenching was

simulated with different axial discretizations, from 6 cells (cell size ~ 33 cm) up to 90 cells (cell size ~ 2 cm).

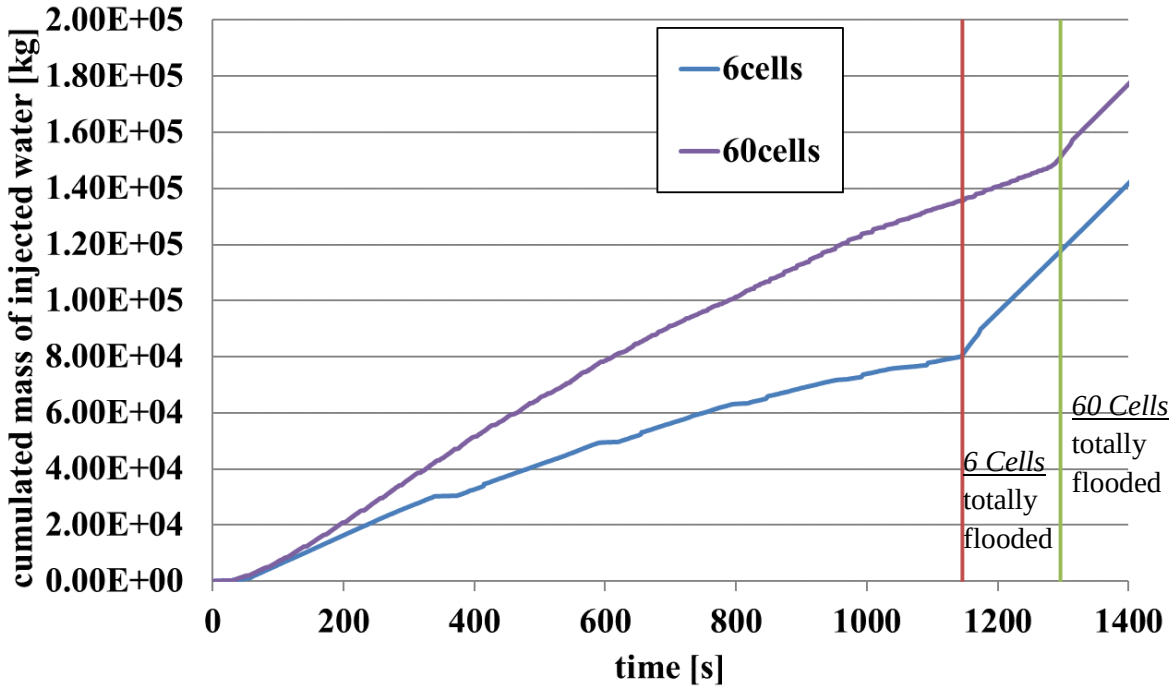

Figure 29 : Mass of water injected over the whole quenching (gravity-driven injection)

From Figure 28 (a), one notices discrepancies between the quench front progression from the different discretizations, approximately 200 s delay between the coarsest (6 cells, orange curve) and the finest meshing (30-60-90 cells, green, mauve and pink curves). Also looking at the cumulated mass of steam generated during the quenching (on Figure 28 (b)), 7% discrepancy between the 6-cell and 30-cell simulations may be observed. However, there is no clear dependency of the meshing on the quench front or on the total mass of produced steam, but rather a non-monotonic convergence of the results seems to be reached by refining the meshing. Figure 29 shows the amount of water injected throughout the quenching process, for calculations with 6 and 60 cells. The total amount at the end of quenching (that is, when the bed is fully flooded) is to be read at the red and green vertical lines, for the coarse and fine meshing respectively. Apart from the quenching delay, it appears that twice more water has been injected for the quenching of the finely discretized bed than for the quenching of the coarsely discretized bed. Further calculations were performed by varying the porosity (porosities of 30%, 40% and 45%, see Figure 30), the particle diameter (diameters of 2.0, 2.9 and 5.0 mm; see Figure 31), the system

pressure (1 bar, 3 bar and 5 bar; see Figure 32) or even the debris bed height (bed heights of 1.5, 2.0 and 3.0 m; see Figure 33).

Regarding the quench front progression, discrepancies between the coarsest and finest discretizations seem to improve significantly by decreasing the porosity, the particle size and the system pressure, or inversely, by increasing the bed height. In each parameter study the quench front discrepancy between the coarse and fine meshing, obtained for the smallest set parameter (i.e. for 30% porosity on Figure 30 (a), for 2.0 mm particle diameter on Figure 31 (a) or for a system pressure of 1 bar on Figure 32 (a)) or for the greatest bed height (3.0 m on Figure 33 (a)) can be significant. For example, almost 500 s delay are observed on Figure 30, Figure 31 and Figure 33 (a). However, the sensitivity on the meshing can be easily distinguished from the effect of the variation of parameters; thus, no confusion is possible. This distinction between the influence of physical parameters and meshing is less obvious, regarding the steam generation. Indeed, taking as example the pressure variations analysis with the finest meshing (90 cells curves), Figure 32 (b) presents negligible difference, regarding the mass of generated steam, which can be therefore confused with the numerical effect of the discretization. Hence, this may lead to some misinterpretations.

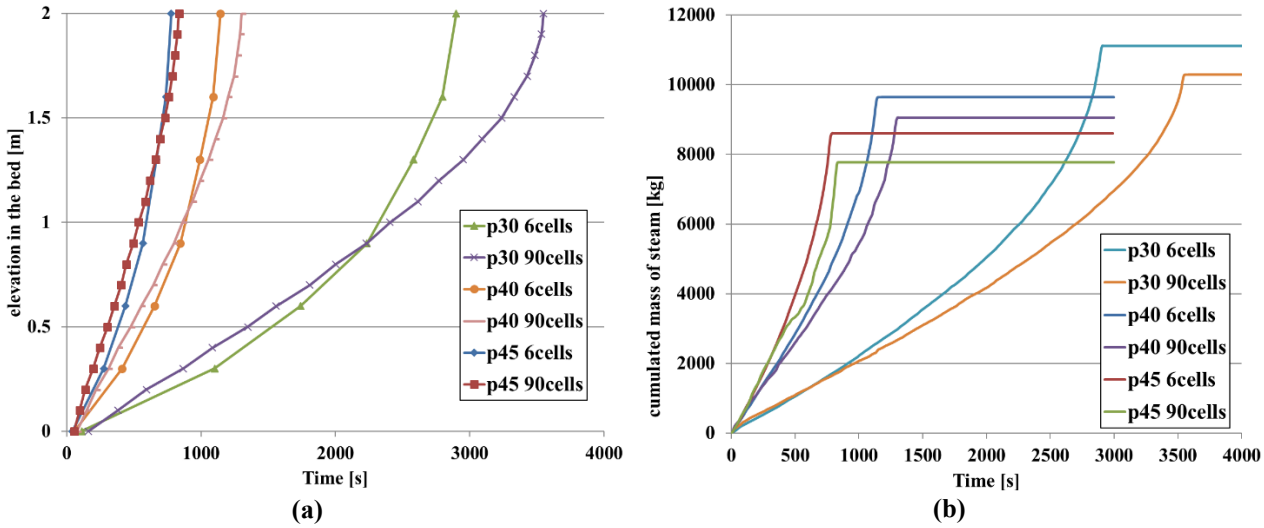

Figure 30 : (a) Quench front progression and (b) Generated mass of steam obtained with 6 and 90 cells for porosities of 30%, 40% and 45%

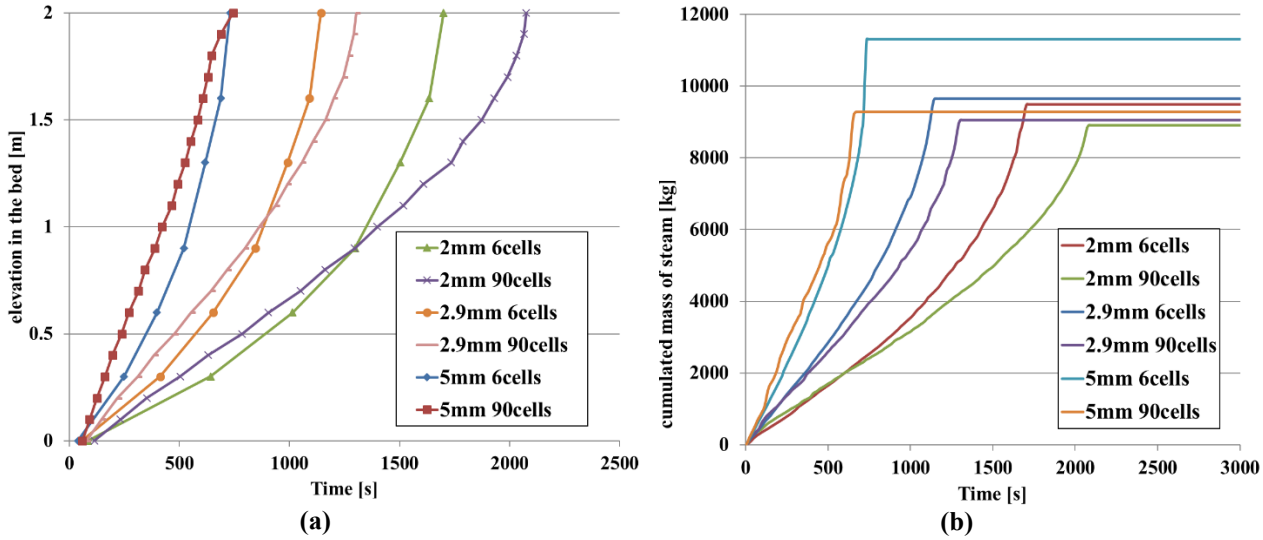

(a) (b)

Figure 31 : (a) Quench front progression and (b) Generated mass of steam obtained with 6 and 90 cells for particle sizes of 2.0, 2.9 and 5.0 mm

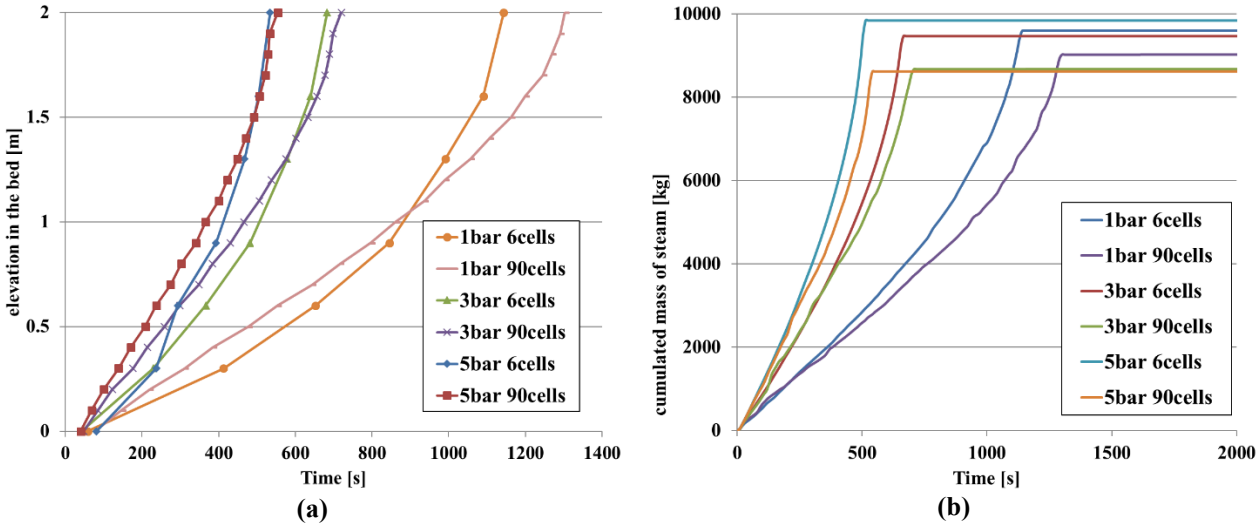

(a) (b)

Figure 32 : (a) Quench front progression and (b) Generated mass of steam obtained with 6 and 90 cells for system pressures of 1, 3 and 5 bar

Some simulations with very coarse discretizations (for instance, 6 and 12 cells) were long-lasting (over an hour instead of a few minutes) and unstable, and had convergence problems. During the simulation, the sign of the calculated velocities at cell faces continuously turned around (water flow downward and upward), as cell void fractions were reaching the minimum value.

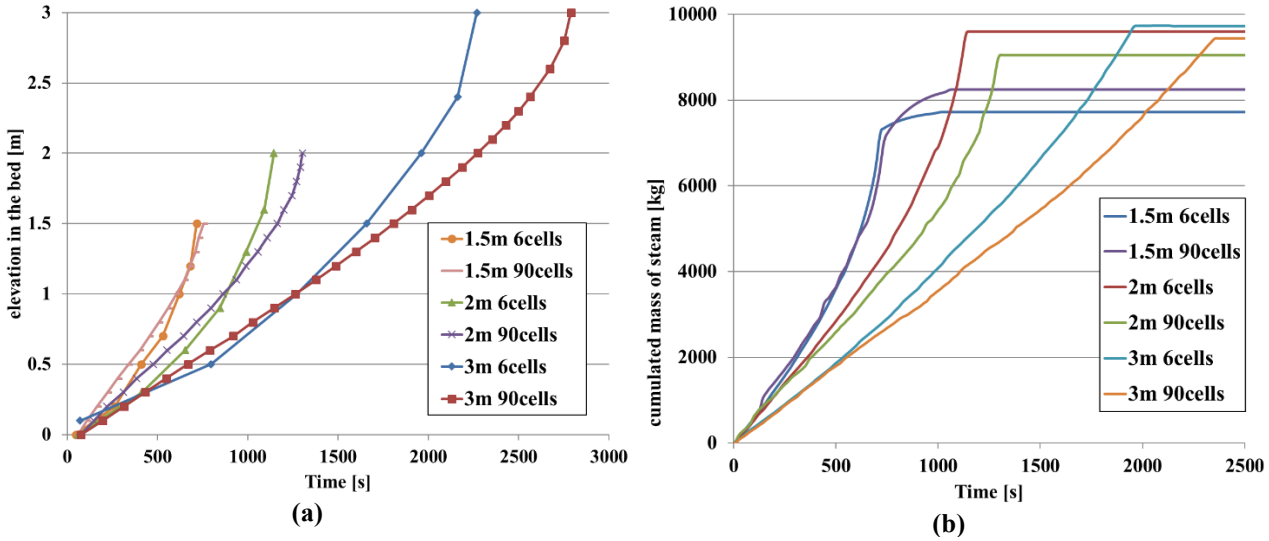

Figure 33 : (a) Quench front progression and (b) Generated mass of steam obtained with 6 and 90 cells for debris bed height of 1.5, 2.0 and 3.0 m

3.5 Identification of the problem

In COCOMO-3D, cells represent homogeneous control volumes, where steam and water are seen as a homogeneous mixture. Like illustrated on Figure 34, a cell with a low void fraction is treated like a liquid continuum with bubbles homogeneously distributed, while a high void fraction is treated like a gas continuum with droplets. Between a certain maximum and minimum void fraction, control volumes are supposed to contain a mixture of droplets and bubbles.

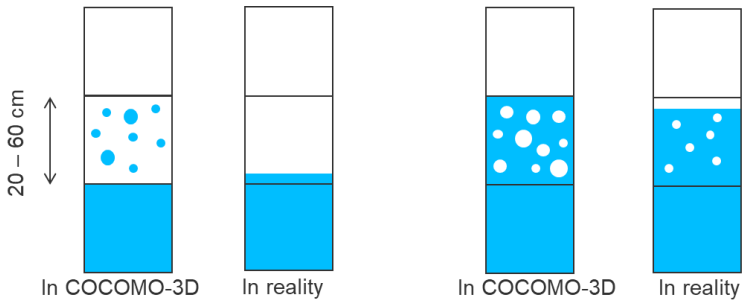

Figure 34 : two-phase flow representation in current COCOMO-3D meshing vs. reality

This assumption is reasonable when working with a fine meshing (cell size ~ some mm to few cm), enabling the computation of the different regime and transient that may occur within a boiling zone. When using large cells, homogeneous steam-water mixture cannot be considered as

a good representation anymore. Rather than that, a separation of the phases is expected. It makes the configuration, in terms of heat transfer totally different; but also, in terms of hydraulics. Indeed, the pressure that is calculated in each cell is valid for the whole cell volume; no pressure gradient is considered within a cell. This assumption doesn't affect the calculation if the cell size is of some mm, since the axial gradient due to the local water column would be very low (and even lower for steam, which has a lower density than water). As for large cells, where phase separation would be expected, pressures above and under the interface should be distinguished. Moreover, when a small amount of water is injected into a dry cell (like depicted on Figure 34, left), it should quench only a proportionate volume of this cell: a part of this water goes into steam and the rest remains liquid, and thus, contributes to the progression of the front. However, in the code, the same small amount of water is distributed over the whole cell, and therefore, all the water evaporates, leading to local pressure oscillations. One has to wait for the cell temperature to reaches the saturation temperature, in order to begin to fill in the cell with water.

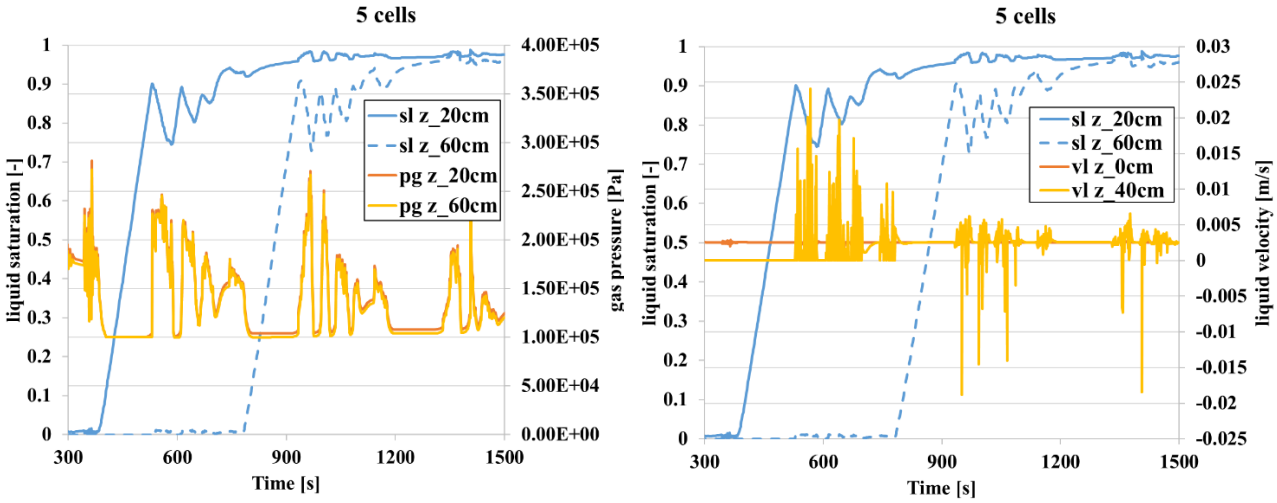

(a) **(b)**

Figure 35 : Cell liquid fraction vs. (a) pressure vs. (b) liquid velocity for coarse meshing

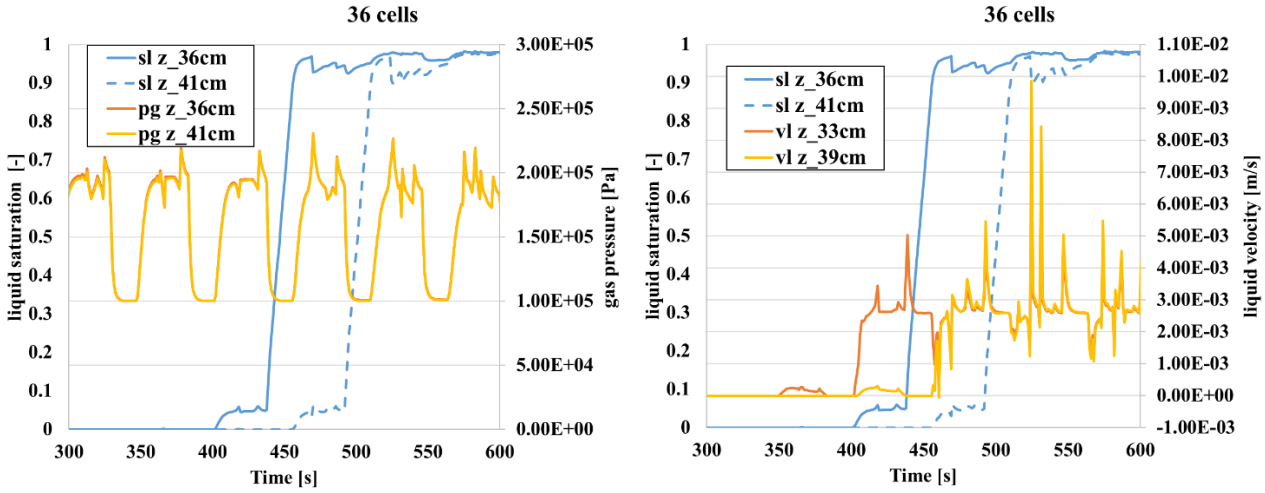

(a) **(b)**

Figure 36 : Cell liquid fraction vs. (a) pressure vs. (b) liquid velocity for fine meshing

During the quenching simulation, it appears that instabilities occur as a cell is about to be fully saturated with water. The pressure inside the whole homogeneous cell, mostly governed by the friction models, seems to be too low; lower than the pressure in the next cells that was supposed to be reached by water. Consequently, this prevents water to flow upwards. What follows now focusses on the quenching at the cell scale in order to highlight the meshing issue.

Figure 35 and Figure 36 focus on the water-filling of one cell during the flooding of the debris bed. This flooding was computed on the same input as the previous reactor-scale debris bed, and was also discretized only axially. Only, here, water is supplied by a fixed injection in order to isolate the effect of the mesh size from the gravity-injection effect (depending on the local pressure). On Figure 35, the blue curve presents the filling of a 40 cm-high cell (bed discretization into 5 cells) at the position $z= 20\ cm$ (centroid of the cell), while the dashed blue curve represents the liquid fraction of the upper neighbour cell (centroid at $z= 60\ cm$). Similarly, on Figure 36 the blue curve addresses a 5.5 cm-high cell (bed discretized into 36 cells) at position $z= 36\ cm$, while the dashed blue curve represents the liquid fraction of the upper neighbour cell (centroid at $z= 41\ cm$). The dimensions and positions of the studied cells are summarized right below:

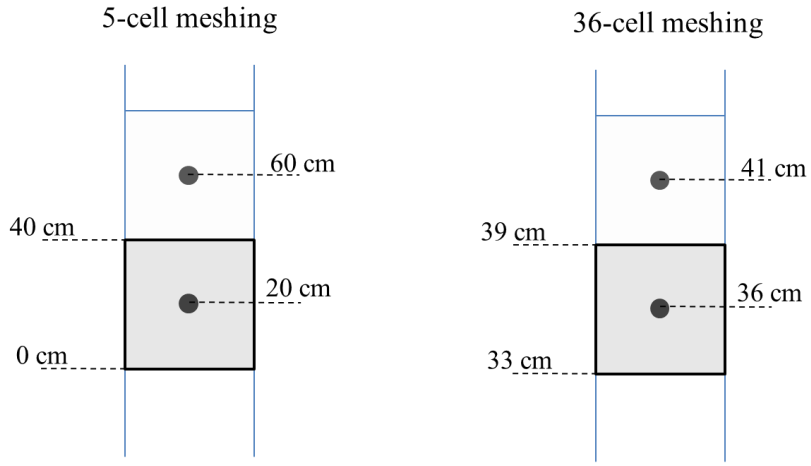

Figure 37 : Dimensions and positions of the studied cells (studied cells in grey)

On Figure 35 and Figure 36 (a), the red and yellow curves represent the pressure evolution in the studied cell and in the upper neighbour cell respectively. On Figure 35 and Figure 36 (b), the red and yellow curves depict the water velocity at the lower and upper boundaries (axial cell edges) of the studied cell. Exact positions of these cell boundaries are reported on the figure above.

From the outcomes of the 36-cell configurations on Figure 36 (a), one observes a slow beginning of filling of the cell (blue curve between *t= 400* and *430 s*) as the pressure is at around 2 bar due to instabilities in the lower neighbour cell. This lower cell is almost totally flooded, but already supplies water to the studied cell, as it can be seen on Figure 36 (b), the red curve representing the velocity of water at the lower boundary of the studied cell. As the pressure gets stable after *t=430 s*, the liquid fraction increases rapidly and monotonically up to 0.95. At this point, the pressure inside the cell increases again to 2 bar and some water is supplied to the upper neighbour cell, judging by the water velocity at the upper boundary of the studied cell (yellow curve on Figure 36 (b)), resulting in a pre-filling of the upper cell. For the case with 5 cells, on Figure 35 (a), one observes a fast increase of the liquid fraction up to 0.90. After reaching 0.90, liquid fraction starts oscillating, as pressure in cell also oscillates. A positive water velocity can be noticed at the upper cell boundary, though it seems that no water reaches the upper cell. Once the pressure gets stable again, the liquid fraction reaches slowly 0.95, the water velocity at the upper boundary gets also stable and allows water flowing upwards into the upper cell. The liquid fraction of the upper cell reaches quickly 0.9, due to the constant and “positive” mass rate of

water. After this point, pressure and velocity starts oscillating again. Water velocity even turns negative, yielding a backflow from time to time.

In brief, it seems obvious that the modelling of two-phase flow in porous media must be revised for the use of coarse meshing. The homogeneous mixture model yields a significant loss of information, when the control volume is too large.

Great efforts were spent in the last decades in order to improve the modelling of the two-phase flow in porous media, for the specific use of severe accident codes. Duval [83] proposed a description of the heat and mass transfer at the pore scale, in order to obtain a macroscopic description with local thermal non-equilibrium by applying a volume averaging method. This modelling required though some assumptions and simplification of the flow configuration at the pore scale in order to solve the closure problem. Bachrata [84] enhanced this model by improving the heat transfer modelling, namely concerning the nucleate boiling. In his work, Sapin [85] assessed more extensively the modelling in his experimental facility, addressing the visualization of the boiling and quenching processes in a debris bed. The model was implemented in ICARE-CATHARE code and validated against the PRELUDE experiments. Being a small-scale experiment, no coarse meshing can be applied. Bachrata [84] performed also reactor-scale simulations, where cell size was axially in the range of 25 cm; aim was namely to identify the differences between small and large-scale simulations, regarding the reflood process.

Moreover, the problem concerns not only cell containing a water and steam interface, but also topological changes, involving different physical behaviour. Figure 38, presenting the simulation of a heap-like bed (in red on the figure) with COCOMO-3D, illustrates this problem of topology changes. The code represents the conical boundary (defined by the user; see the yellow line on the figure) as a smeared surface, since cells in COCOMO-3D may only be homogeneous; i.e. either a cell belongs only to the porous zone (debris bed, in red on the figure), or it belongs only to the non-porous zone (pool outside the bed, in blue on the figure). This approximation of linear slopes of boundaries through step-like boundaries strongly overestimates the boundary area, when using coarse meshing (and even more in 3D). It can subsequently cause numerical problems and significant quantitative errors, namely regarding quantities like heat exchanges within the bed, which are volume-related, or heat transfers at the bed surface.

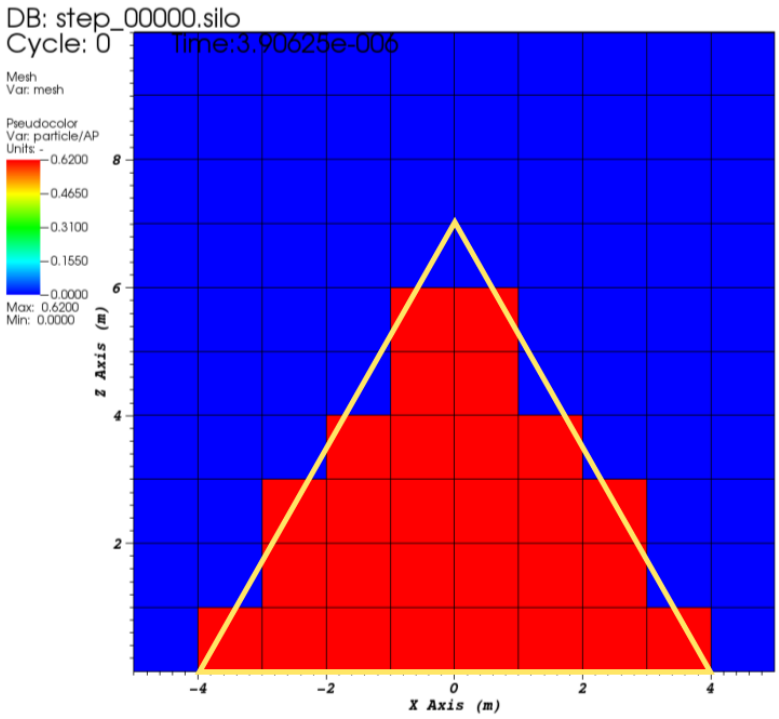

Figure 38 : Modelling of a conical debris bed in COCOMO-3D (yellow line: user-defined geometry)

In order to overcome the numerical problems that may occur in simulation with coarse meshing, solutions have to be found to deal with cells, containing the debris bed boundaries, but also the quench front. Concerning the debris bed geometry, surface smearing can be avoided by reconstructing the boundaries in cells containing it. In other words, a method must be found that splits cells into two new cells: one belonging to the debris bed zone, the other belonging to the pool outside the bed. The interface position is determined by the zone geometry, which is supposed to be set by the user. Of course, it will generate cells that cannot be described in a regular grid anymore. For this reason, the current work couldn't have gone any further with the standard version of COCOMO-3D using a structured meshing, and must be pursued with an unstructured version. However, new problems arise regarding the reconstruction of the quench front. Firstly, the position of the quench front is not foreseen to be defined by user's settings, but depends on physical criteria, that will be discussed in the next chapters. Secondly, the front evolves with time. Therefore, a dynamic grid is required, which enables the creation and suppression of nodes and cells during the simulation.

In the following chapters, a method will be developed to generate a meshing respecting the geometry of the debris bed domain, by means of an unstructured meshing. Consequently, in order to pursue this work, only the unstructured version of COCOMO-3D can be used. After that, another reconstruction method addressing the quench front progression will be developed. To do that, one has to find an approach to track the quench front in the meshing at each time step, and reconstruct the front by means of a method relying on physical parameters. The reconstruction yields new cells and change their geometry as they are swept by the quench front. Therefore, conservation equations must be locally adapted, accounting for geometry changes of the concerned cells but also for the specific heat and mass transfers through the quench front. The modelling of the quench front reconstruction will be firstly verified against one-dimensional basics cases. Finally, the reactor-scale simulations performed previously in section 3.4 will be repeated with the new modelling and compared to the old results, in order to take note of the actual improvement.

4 New models for reconstruction of bed geometry and quench front

4.1 General

In this chapter, a new approach is developed in order to deal with cells containing topology changes, different than the basic averaging of the phase properties inside the control volume. In the previous chapter, it came out that the actual modelling lead to area/volume overestimation when reconstructing a porous zone with a coarse meshing. The particular behaviour of the quench front cannot be properly modelled by a fixed coarse meshing, since the homogeneous approach for the cell containing the quench front, that are called “mixed cells” in literature (since they contain at least two continuums; i.e. each phase is present in a significant amount inside the cell), leads to a strong loss of information. Pressure may be unrealistic, and the wrong heat transfer regimes are considered. These issues are hard, if not impossible, to overcome by using a regular orthogonal meshing. For this reason, the unstructured version of COCOMO-3D must be used, enabling the generation of irregular grids. The first part of this chapter is dedicated to the reconstruction of the debris bed boundaries. The reconstruction of the quench front is addressed in the second part. The necessary modifications of the conservation equations for the mixed cells are presented in the third part, while the last part gives an overview of the new resolution algorithm.

4.2 Debris bed reconstruction

Only debris beds with a trivial geometry are considered: with a polygonal section, defined by the user. At the scale of cells, the boundaries of the bed domain can be seen locally as straight lines (2D, see example on Figure 39) or planes (3D). Knowing the geometry, i.e. the coordinates of each zone vertex (black points on Figure 39), line/plane equations can be locally easily determined in each cell intersected by the boundaries.

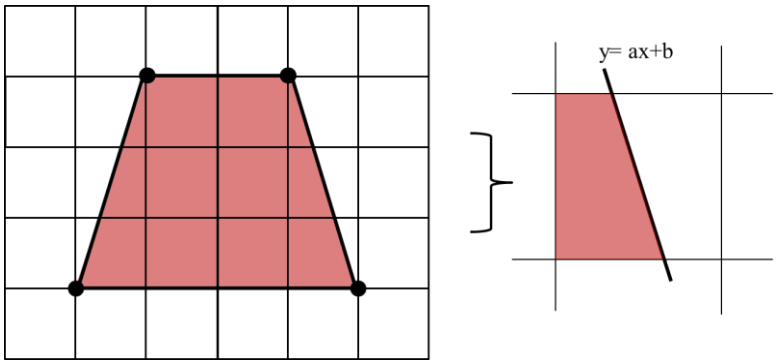

Figure 39: 2D-example of cells intersected by the bed boundaries

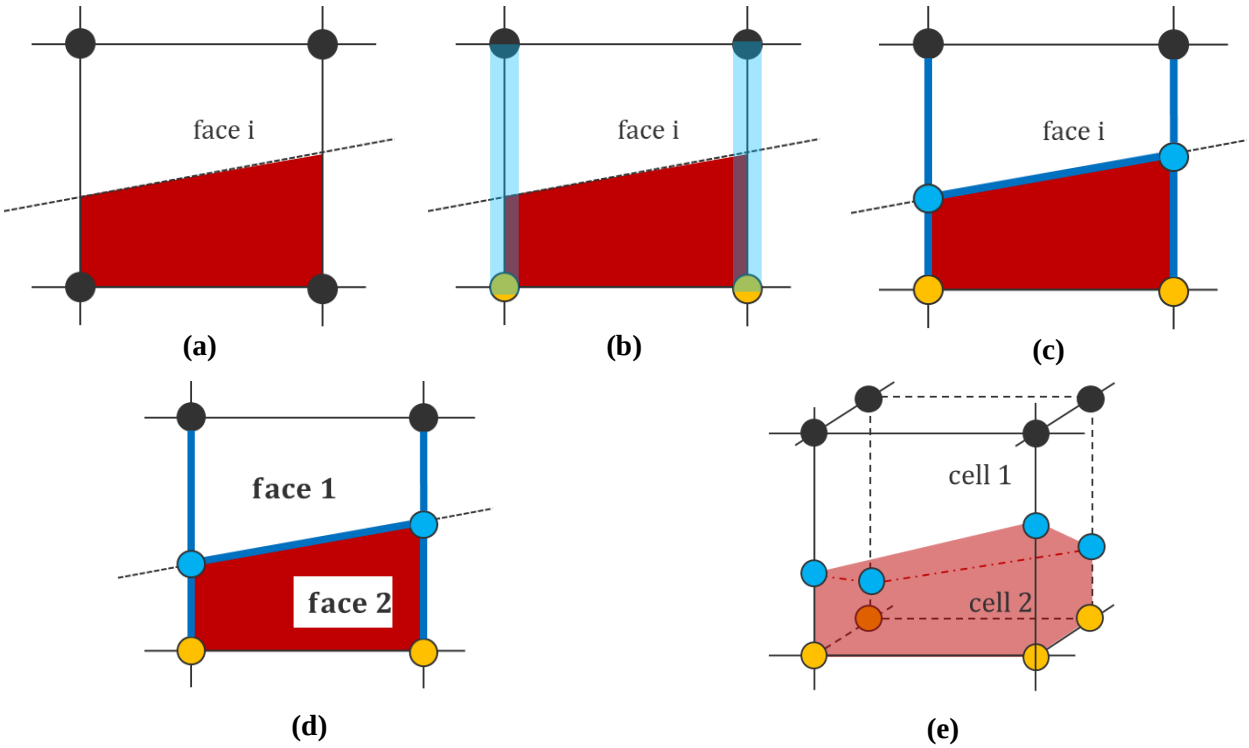

Figure 40 : Process of bed boundary reconstruction

The reconstruction procedure is depicted on Figure 40. The first step consists in tracking the cells that are intersected by the bed boundaries. To do this, each node of the grid must be flagged with respect to the zone it belongs to: either to the bed zone, or outside the bed zone. Coordinates of each node have to be compared to the boundary equation of the cell it belongs to, under the form [$f(x) = ax+b$] in 2D. For example, on Figure 40 (b) cell node of coordinates (x_i, y_i) belongs to the bed zone (marked by yellow points) if:

$$ax_i+b - y_i > 0$$

otherwise the nodes lay outside. After that, the intersected edges must be found. An edge is intersected if its two nodes belong to different zones (marked in blue on Figure 40 (b)). At the intersection point of the boundary line with the edge, a new node is created (blue points on Figure 40 (c)). Faces that have two cut edges, are also supposed to be intersected. Junctions between the two newly created nodes (from the two intersected edges) is defined as a new edge. From this, two new faces are created as shown on Figure 40 (d). Subsequently, cells that have at least three split faces, contains necessarily the boundaries, which is reconstructed as a new face, formed by all the newly created edges of the cell. Figure 41 shows a post-visualization of a conical debris bed, which has been reconstructed in a coarse grid by the approach described above.

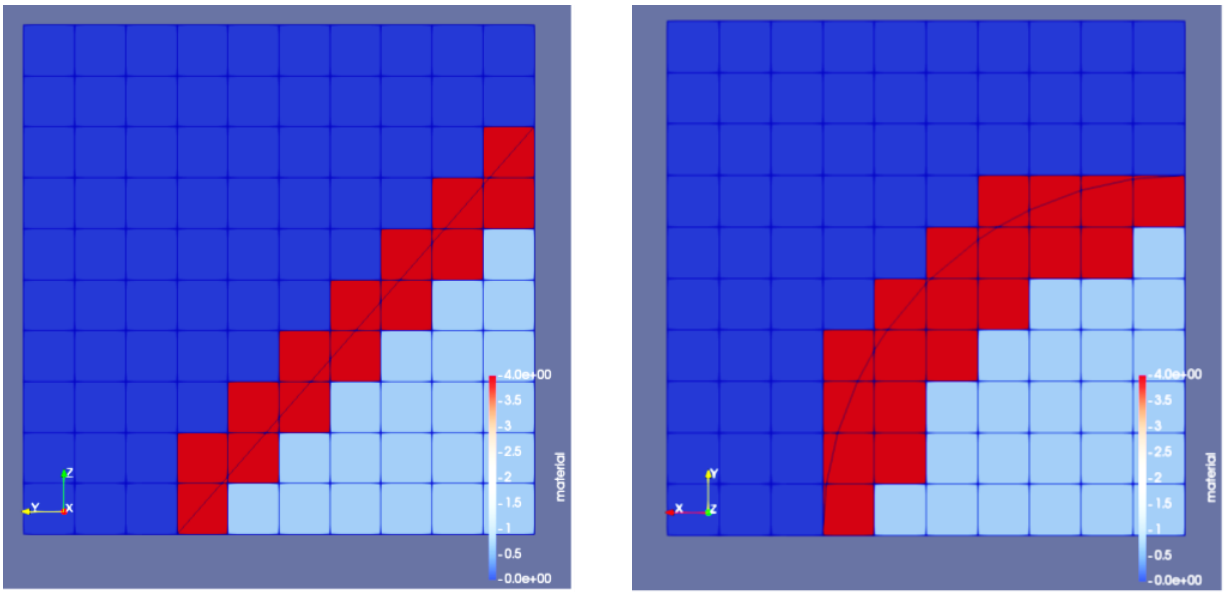

Figure 41 : Reconstruction of an heap-like bed in COCOMO-3D (left: vertical section through the centre of bed; right: horizontal section at the base of bed)

Light blue cells are original cells belonging completely to the bed domain. Dark blue cells are outside the bed domain. Original cells intersected by the bed boundaries are marked in red. From Figure 41 (left), one notices that the expected triangular aspect of the vertical section of the cone is very well reconstructed, and above all, the boundary presents no discontinuity. The circular

boundary of the base of the cone is also satisfactory reconstructed (see Figure 41 (right)), though a perfect circle cannot be generated by the method exposed here.

4.3 Quench front reconstruction

4.3.1 Existing tracking methods

Many methods exist nowadays regarding the reconstruction of interface between the present phases. Most of them are based on the volume fraction of each material in a control volume. Among these methods, only a few might be appropriate depending on the situation. One of the first methods, by Harlow et al. [86] and Amsden [87], consisted in tracking marker particles. The level-set method, more mathematical, was developed by Osher and Sethian [88]. Later appeared another kind of reconstruction method, so-called “simple line interface calculation” SLIC by Noh et al. [89], which reconstructs the interface within the cell as one segment aligned with one of the major coordinate axes (see example on Figure 42 (a)); in the literature, this method belongs to the group of the piecewise constant methods. With the volume-of-fluid (VOF) method from the work of Hirt and Nichols [90], while segments are still parallel to one of the coordinates axes, more than one segment may exist in the same control volume (see Figure 42 (b)); it is referred then to piecewise stair-stepped methods. Though these methods are quite simple to implement, they cannot reproduce the multidimensional behaviour of the interface in a realistic way, and their representation in a coarse meshing may seem unsatisfactory.

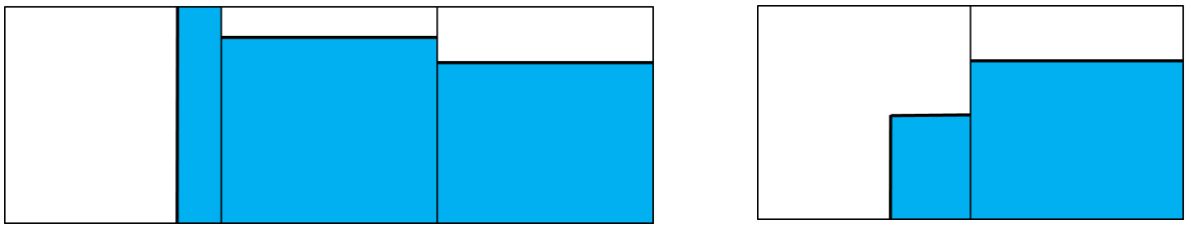

(a) **(b)**

Figure 42 : illustration of (a) piecewise constant and (b) stair-stepped methods

The PLIC (piecewise linear interface calculation) method overcomes this issue, by representing the interface in each cell also as a segment, but that can be inclined (developed by Young [91,92];

implementation well detailed by Rider et al. [93]). The approach consists in two steps, depicted on Figure 43 (a). First, the slope of the interface line is determined (**(1)** on the figure); i.e. the normal vector of the interface must be estimated. Several methods are available in the literature to estimate the normal vector. But one of the most famous is the Young's method, which basically treats the normal as being the local volume fraction gradient. In other words, considering the discrete nature of the computation, the normal is calculated as a function of the volume fraction of the neighbouring cells. The method was first developed for 2D cases, and later on extended to 3D configurations. However, the Young's approach can be only applied on orthogonal meshes. Johnson extended this approach for irregular meshes in [94].

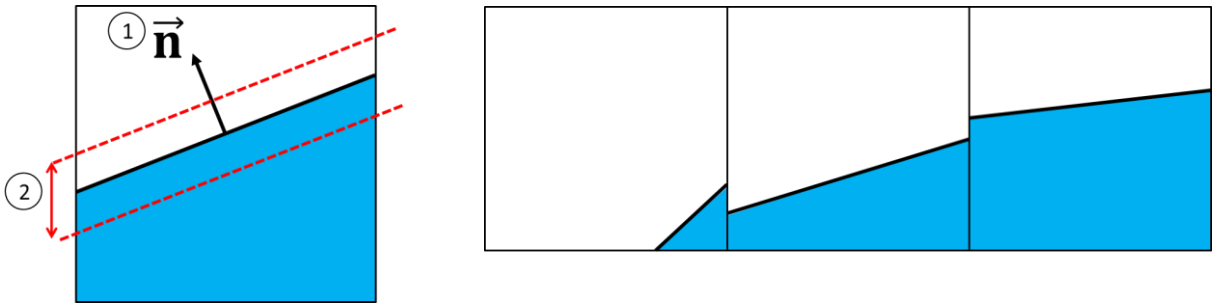

(a) **(b)**

Figure 43 : Illustrations of (a) PLIC reconstruction and (b) its resulting discontinuities

After determining the slope, the position of the interface is set with respect to the volume fraction (**(2)** on the figure). Volume under the interface must correspond to the volume fraction. These methods present two inconveniences. Firstly, they are not appropriate for multi-material situation (more than 2 materials). Secondly, interface discontinuities will appear between two neighbour cells (Figure 43 (b)).

Other interesting existing approaches, originally developed for visualization, might remove these two issues, such as the isosurface [95] or equisurface [96] algorithms. In these methods, average volume fractions of materials must be first estimated at each vertex. The isosurface algorithm reconstructs a surface where the volume fraction of a certain material is 0.5. Knowing values of volume fractions at each vertex, the line, representing a constant value of the volume fraction of 0.5 in the cell, can be reconstructed by interpolating the values at each concerned edge, like it is shown on Figure 44 (a). Different of isosurface method, the equisurface method reconstructs a surface where the volume fractions of two pairs of materials are equal. For instance, on Figure 44

(b), for the left edge, the position where the volume fractions of the material 1 and 2 (denoted in black and green respectively) happen to be equal (0.45) is denoted in red. This method is worth for cells containing more than two materials though. Otherwise, it would yield exactly the same surface as the isosurface method (surface of volume fraction 0.5).

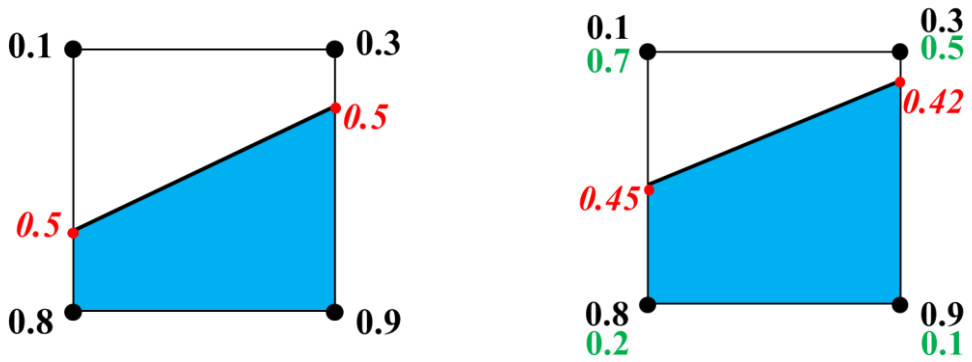

Figure 44 : Illustration of (a) isosurface and (b) equisurface reconstructions

As mentioned by Meredith [95], all these approaches ultimately enable the continuity between interfaces of neighbour cells, since the construction will depend on volume fractions along edges (and not volume fraction of cells). But, unlike the PLIC method, the volume of fluid cannot be exactly matched.

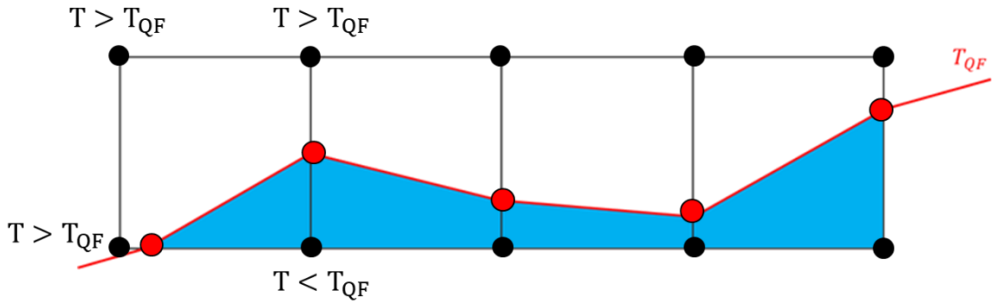

Figure 45 : Illustration of the isotherm reconstruction method

A last appealing approach would consist in reconstructing the quench front as an isotherm. Analog to the isosurface method, but taking temperatures instead of void fraction as criterion, average temperatures must be first calculated at cell vertices. Isotherm is then reconstructed by

joining the points at edges, located by interpolation, where the temperature is the predefined quench front temperature (see Figure 45). This approach is inspired from the Marching Cube method [97], addressing visualization issue like shading of a surface by reconstructing lines of constant shading value. At this point it is worth to remind how a quench front is defined. A quench region is mostly characterized by the boiling processes and so by the local temperatures, and namely the particle temperatures, since this quantity is the easiest to measure experimentally; in particular compared to void fraction or heat fluxes. In order to simplify the problem a little, a low injection velocity is assumed, yielding a slow quenching. While a fast quenching (from a high velocity injection) yields a large quench region, a slow quenching yields a very thin quenching region, which can be seen as a surface, defined by one temperature. It is harder to describe a large quench region by only one parameter. To stay the more conservative possible, the different regimes of the quench region should be distinguished, by referring to different specific temperatures. Assuming a low injection, the quench front can therefore be represented by an isotherm, i.e. a surface where the temperature T_{QF} is constant. As mentioned in the literature as well as in experiments presented in this work, the value of T_{QF} is often estimated as near to the saturation temperature T_{sat}.

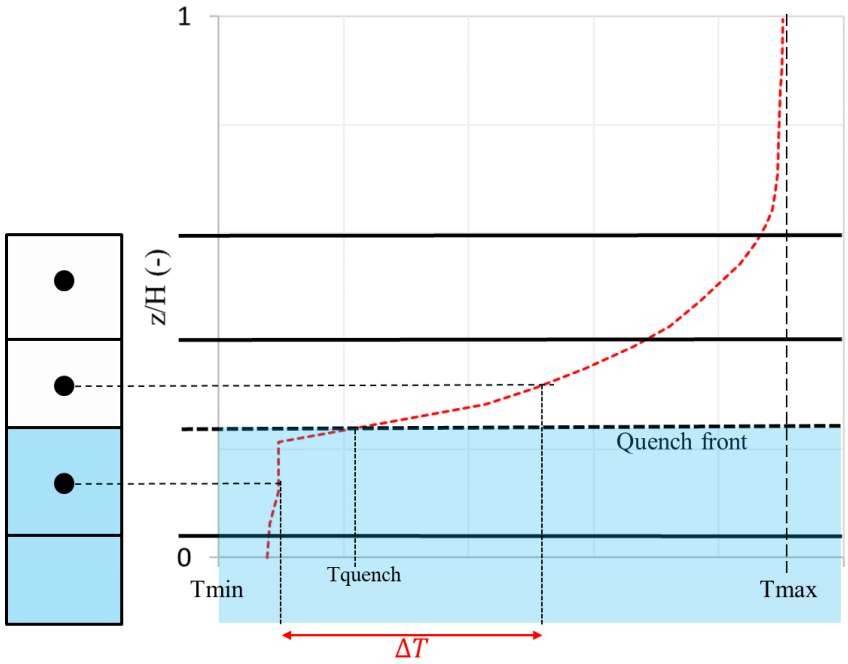

Figure 46 : Temperature gradient at the interface by using the isotherm reconstruction method

However, this method might present a major disadvantage. While representing the quench front as an isotherm, and so as a cell face, may be a realistic way to visualize the quench front, the use of such a method for quenching calculations is questionable. The quench front temperature will never directly intervene in the equations or in the temperature gradient calculation. (see Figure 46).

4.3.2 Quench front tracking

After this overview of existing methods of interface reconstruction, time has come to focus on the present issue of quench front reconstruction. It would seem natural to use the liquid volume fraction, as criterion for the tracking of mixed cells and the reconstruction, like for all the methods presented above. The PLIC method for instance, would split a mixed cell into a purely gaseous cell and a purely liquid cell, whereas under the quench front a liquid continuum with bubbles would be more realistic. More inconvenient are the quench front discontinuities that come out at cell edges, which would require some extra treatments, like smoothing for example. The isosurface algorithm can overcome this issue, though does not take into account the presence of bubbles in the liquid phase neither. The isotherm method presents the benefits of relying on thermal criteria, more representative of the quench front definition. Nevertheless, a major issue arises concerning the calculation of quench front progression with this method. From the reconstruction one obtains the volume under the quench front, as well as the volume difference between two time levels, from which the quench front velocity can be deduced. In others words, the quench front velocity is only governed by the local temperatures, which makes the computation hard to control, and the effect of other parameters, such as water mass rates, difficult to predict. Moreover, as already mentioned, the quench front temperature would be used for the reconstruction only, and not even for the heat transfer calculations.

In terms of computation, the quench front progression should be strongly influenced by the amount of water flowing in and out of mixed cells, and also by the temperature gradient between the debris bed and water, i.e. by the evaporation rate at the quench front region. This implies a method that takes the volume of water as criterion for the reconstruction, and that is coupled with

an assumption on the evaporation process at the quench front, accounting explicitly for the quench front temperature, in order to determine the quench front velocity.

The coming approach is derived from the isosurface method in order to ensure an easy reconstruction and no discontinuity of the quench front from one cell to another. This approach is however a bit different from the standard isosurface method in that it does not rely on the volume fraction of material (i.e. water or steam; more specifically s_l or s_g), as it could be expected, but on the volume fraction of the "quenched" sub-cell under the interface, henceforth denoted "*CVF*" (Cell Volume Fraction), as depicted on Figure 47 and defined as follows:

$$\mathrm{CVF} = \frac{V_{dn}}{V_{dn} + V_{up}} = \frac{V_{dn}}{V} \qquad (4\text{-}1)$$

V_{dn} and V_{up} being the volume of the quenched (*dn*) and unquenched (*up*) sub-cells. Calculation of V_{dn} and V_{up} will be developed later in 4.4.4.

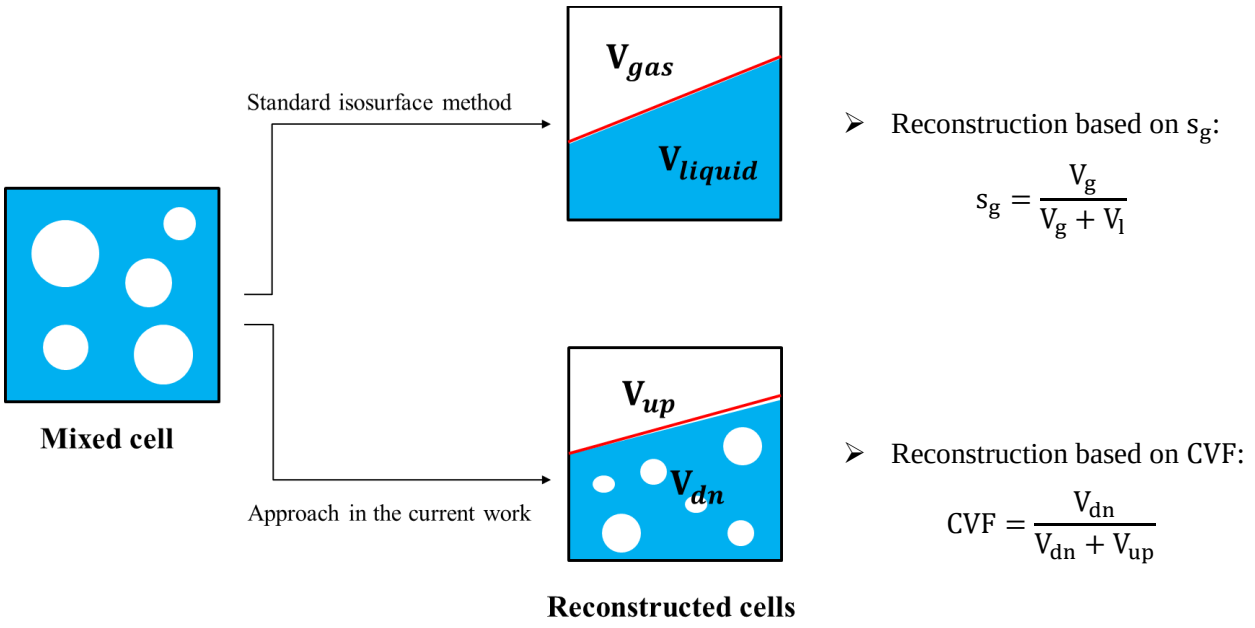

Figure 47 : Standard isosurface reconstruction vs. current reconstruction method

The volume under the curve (obtained after the reconstruction) might not fully match with the actual volume of the quenched sub-cell (obtained by the resolution of the equation system) though. The quench front velocity can be determined on the basis of assumption concerning

evaporation and water flow at the quench front (seen 4.4.2), as a function of T_{QF}. The new resolution of the conservation equations will be detailed in 4.4.

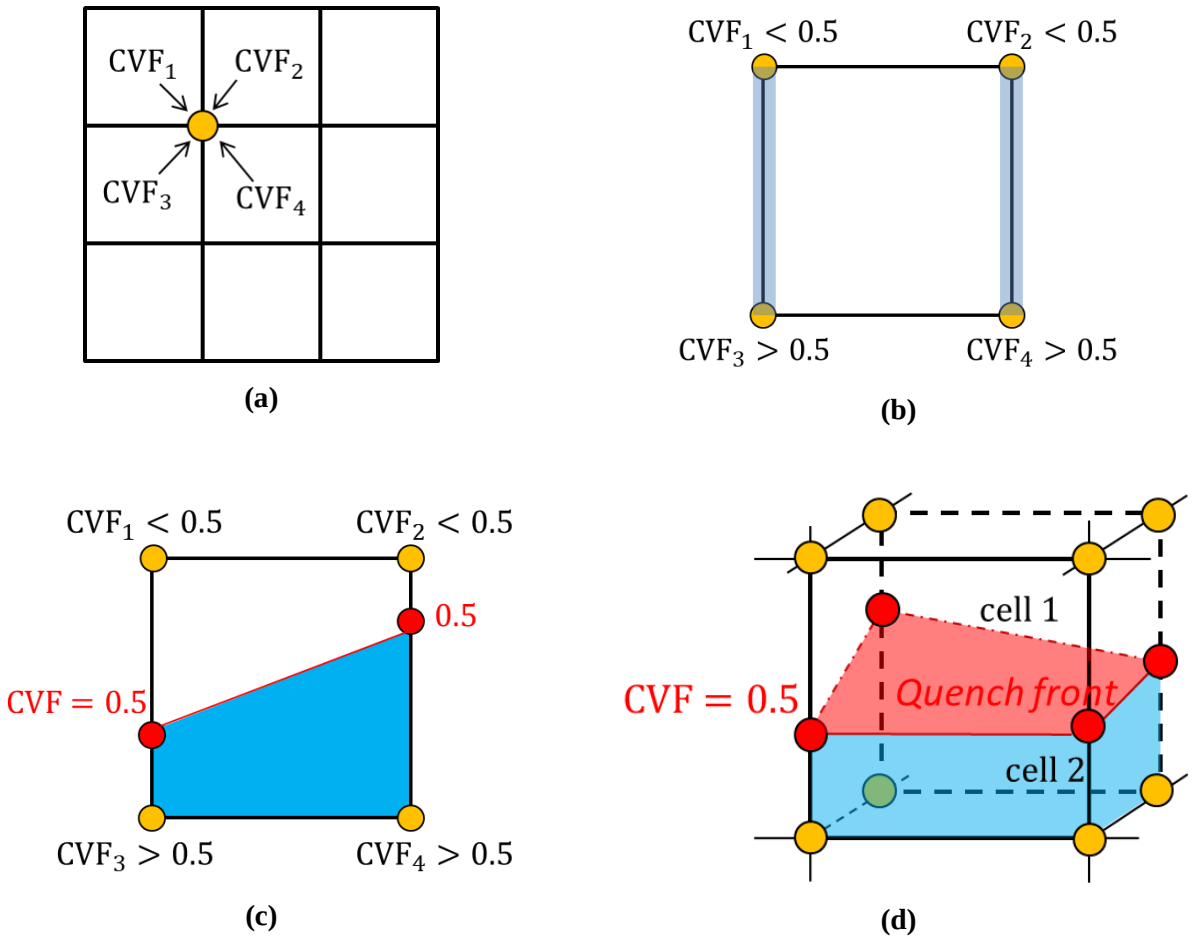

Figure 48 : Procedure of the quench front reconstruction

Like explained in the previous section, first, average *CVF* at each vertex must be calculated (see Figure 48 (a)). Averaging methods can be consulted in Appendix-H. After that, it can be checked which vertices (i.e. grid nodes) belong to the zone below the quench front:

- If $CVF_{node} < 0.5$, then not quenched, node is above the quench front.
- If $CVF_{node} > 0.5$, then quenched, node is therefore under the quench front.

Applying the same method developed in the previous section for the debris bed reconstruction, mixed cells can be detected. Cell edges that have one vertex above ($CVF_{node} < 0.5$) and the

other one under ($CVF_{node} > 0.5$) the quench front are ultimately intersected by the quench front, like the edges marked in blue on Figure 48 (b).

The position of the intersection point on each intersected edge is found by interpolating the CVF. Knowing the coordinates of the two nodes denoted $\boldsymbol{x_1}(x_1, y_1, z_1)$ and $\boldsymbol{x_2}(x_2, y_2, z_2)$ and their respective cell volume fractions CVF_1 and CVF_2, the position of the intersection point $\boldsymbol{x_{QF}}(x_{QF}, y_{QF}, z_{QF})$ of the edge (joining $\boldsymbol{x_1}$ and $\boldsymbol{x_2}$) with the quench front line of constant value *0.5*, can be obtained by:

$$\mathrm{x_{QF}} = \frac{0.5 - \mathrm{CVF_1}}{\mathrm{CVF_2} - \mathrm{CVF_1}} (\mathrm{x_2} - \mathrm{x_1}) + \mathrm{x_1}$$

At these coordinates, a new node is created (Figure 48 (c)). If two edges of a same face are intersected, then the face is supposed to be split into two faces. The quench front line can be reconstructed by joining the two intersection points belonging to the two edges; this line is defined as new edge. Cells that have at least three faces containing a quench front line, are ultimately mixed cells; and thus, they will contain the quench front surface. The quench front surface, which will subsequently be stored as a new cell face, is formed by the quench front lines of the intersected faces. Finally, the mixed cells are split by the newly created surface into two new cells, with the quench front as common face, like shown on Figure 48 (d).

4.4 Adaptation of conservation laws with respect to moving boundaries

4.4.1 Spatial conservation law

The reconstructed quench front evolves with time. In other words, since the quench front is discretized into cell faces, one has to work on cells having moving boundaries. In our case, one edge (in 2D) or face (3D) moves, i.e. the interface, while the others remain fixed. As a matter of fact, these cells, with moving boundaries, are subject to volume variations and have to be handled very carefully. Indeed, in addition to the usual conservation equations, the spatial conservation law (SCL) must be respected in order to avoid numerical errors regarding volumes and masses. The interface velocity (i.e. quench front velocity) must be taken into account in every

conservation equation, namely in the expression of the liquid and gas velocity. Indeed, if the face moves, one has to refer to the relative velocity $\vec{u}_{rel}$, when integrating the mass over a cell:

$$\vec{u}_{rel} = \vec{u} - \vec{u}_{QF} \, , \tag{4-2}$$

where $\vec{u}$ is the computed velocity of water or steam though the face, and $\vec{u}_{QF}$ is the quench front velocity.

From the work of Trulio and Trigger [98], the rate of change of an elementary control volume is directly related to the velocity of the surface bounding the control volume (see Figure 49). This relation can be formulated by (4-3), with $\vec{u}_b$ being the general denomination of the moving boundary velocity.

$$\frac{d}{dt}\int_V dV = \int_S \vec{u}_b \cdot d\vec{S} \tag{4-3}$$

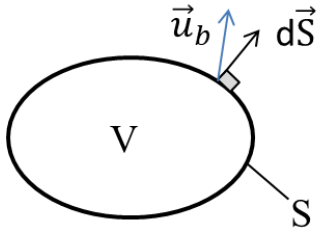

Figure 49 : Control volume with moving boundary

Demirdzic and Peric [99,100] discretized the equation (4-3) over an arbitrary quadrilateral grid cell (see Figure 50), and obtained the relation (4-4), where V and V^{old} are the cell volumes at the new and old time levels respectively; $\vec{u}_{bi}$ is the velocity of the cell face i, of surface area vector $\vec{A}_i$.

$$\frac{1}{\Delta t}\left(V - V^{old}\right) = \sum_i \vec{u}_{bi} \cdot A_i \quad , \quad i = e, w, n, s \tag{4-4}$$

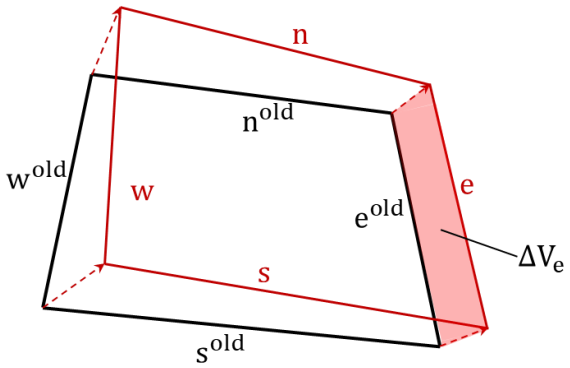

Figure 50 : Quadrilateral grid cell at two successive time points

The main objective here is to express velocities $\vec{u}_{be}, \vec{u}_{bw}, \vec{u}_{bn}$ and $\vec{u}_{bs}$, such that the SCL is satisfied. In other words, the volume changes yielded by the estimated velocities must be equal to the volumes (or area, in 2D) swept by the faces during the time Δt. In their early work [99], Demirdzic and Peric found a way to compute velocities for 2D cases that fits the SCL, which may also work in 3D.

Moreover, considering that the total volume change of the cell corresponds to the sum of the swept volumes of each of its faces during Δt (sign depending on velocity direction):

$$\frac{1}{\Delta t}\left(V - V^{old}\right) = \frac{\sum_i \Delta V_i}{\Delta t}, \quad i = e, w, n, s \tag{4-5}$$

The discrete form of SCL (4-4) remains fully satisfied if (4-6) is assumed.

$$\vec{u}_{bi} \cdot \vec{A}_i = \frac{\Delta V_i}{\Delta t}, \quad i = e, w, n, s \tag{4-6}$$

However, in the present work, ΔV is also an unknown of the conservation equation system. The quench front velocity must be found by an additional physical assumption.

4.4.2 Formulation of the quench front velocity

It is assumed that the quench zone is very thin, so that it can be approximated by a plane front that is identical with the water front. As explained in the last section 4.3.2, the quench front splits

a cell in a cold (quenched) sub-cell denoted by index *dn* (“down”) and a hot sub-cell denoted by index *up*. One denotes with a single prime the state directly under the interface (e.g. u_l' is the liquid velocity right under the interface) and with double prime the states directly right above the interface (e.g. u_l'' is the liquid velocity above the interface), like depicted on Figure 51.

In order to determine the quench front velocity, the following assumption is made: because the quench zone remains thin, no mass or energy can be stored in it. Then, the total mass balance across the quench front moving at velocity u_{QF} can be expressed as

$$\begin{aligned}\varepsilon s_l'\rho_l'\left(u_l' - u_{QF}\right) + \varepsilon s_g'\rho_g'\left(u_g' - u_{QF}\right) + (1-\varepsilon)\rho_s'\left(u_s' - u_{QF}\right) - \varepsilon s_l''\rho_l''\left(u_l'' - u_{QF}\right) \\ -\varepsilon s_g''\rho_g''\left(u_g'' - u_{QF}\right) - (1-\varepsilon)\rho_s''\left(u_s'' - u_{QF}\right) = 0\end{aligned} \tag{4-7}$$

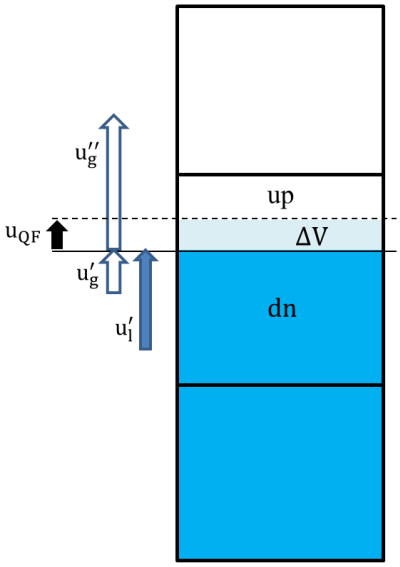

Figure 51 : Volume swept by the quench front during Δt and the associated velocities

The total energy balance across the quench front yields

$$\begin{aligned}\varepsilon s_l'\rho_l'i_l'\left(u_l' - u_{QF}\right) + \varepsilon s_g'\rho_g'i_g'\left(u_g' - u_{QF}\right) + (1-\varepsilon)\rho_s'i_s'\left(u_s' - u_{QF}\right) \\ -\varepsilon s_l''\rho_l''i_l''\left(u_l'' - u_{QF}\right) - \varepsilon s_g''\rho_g''i_g''\left(u_g'' - u_{QF}\right) \\ -(1-\varepsilon)\rho_s''i_s''\left(u_s'' - u_{QF}\right) = 0\end{aligned} \tag{4-8}$$

The solid particles do not move, and for simplification, it was assumed the mass of particles does not change across the interface (same porosity and density), i.e.:

$$u_s' = u_s'' = 0 \tag{4-9}$$
$$(1-\varepsilon)\rho_s'(u_s' - u_{QF}) = (1-\varepsilon)\rho_s''(u_s'' - u_{QF}) = (1-\varepsilon)\rho_s u_{QF}$$

Furthermore, it is assumed that the debris bed ahead of the front is dry and no liquid crosses the interface. Thus,

$$s_l'' = 0\ ;\ u_l'' = 0 \tag{4-10}$$

Then, the mass balance equation across the interface simplifies to

$$\varepsilon s_l'\rho_l'(u_l' - u_{QF}) + \varepsilon s_g'\rho_g'(u_g' - u_{QF}) - \varepsilon s_g''\rho_g''(u_g'' - u_{QF}) = 0 \tag{4-11}$$

and the energy balance equation becomes

$$\begin{aligned}\varepsilon s_l'\rho_l' i_l'(u_l' - u_{QF}) + \varepsilon s_g'\rho_g' i_g'(u_g' - u_{QF}) + (1-\varepsilon)\rho_s u_{QF}(i_s'' - i_s') \\ -\varepsilon s_g''\rho_g'' i_g''(u_g'' - u_{QF}) = 0\end{aligned} \tag{4-12}$$

From (4-11) one gets

$$\varepsilon s_g''\rho_g''(u_g'' - u_{QF}) = \varepsilon s_l'\rho_l'(u_l' - u_{QF}) + \varepsilon s_g'\rho_g'(u_g' - u_{QF}) \tag{4-13}$$

Equation (4-13) inserted into equation (4-12) gives

$$\begin{aligned}\varepsilon s_l'\rho_l' i_l'(u_l' - u_{QF}) + \varepsilon s_g'\rho_g' i_g'(u_g' - u_{QF}) + (1-\varepsilon)\rho_s u_{QF}(i_s'' - i_s') \\ -\left[\varepsilon s_l'\rho_l'(u_l' - u_{QF}) + \varepsilon s_g'\rho_g'(u_g' - u_{QF})\right] i_g'' = 0\end{aligned} \tag{4-14}$$

Solving (4-14) yields an expression for u_{QF}, function of the properties under the interface, and of the energy gradient across the interface:

$$u_{QF} = \frac{\varepsilon s_l'\rho_l' u_l'(i_g'' - i_l') + \varepsilon s_g'\rho_g' u_g'(i_g'' - i_g')}{\varepsilon s_l'\rho_l'(i_g'' - i_l') + \varepsilon s_g'\rho_g'(i_g'' - i_g') + (1-\varepsilon)\rho_s(i_s'' - i_s')} \tag{4-15}$$

In order to be able to calculate the quench front velocity, known values to the prime variables on the left-hand side of equation (4-15) must be assigned.

Firstly, it is assumed that the liquid and gas state right under the interface equal the bulk values in the sub-cell *dn* (up-wind assumption):

$$s_l' = s_{l,dn},\quad \rho_l' = \rho_{l,dn},\quad v_l' = v_{l,dn},\quad i_l' = i_{l,dn} \tag{4-16}$$

and

$$s_g' = s_{g,dn},\quad \rho_g' = \rho_{g,dn},\quad v_g' = v_{g,dn},\quad i_g' = i_{g,dn} \tag{4-17}$$

Concerning the solid phase enthalpy, one assumes that it is quenched during the passage of the quench front from the temperature it has ahead of the front (in sub-cell *up*) to a temperature T_{QF} close to the saturation temperature, i.e.

$$\begin{aligned} \mathrm{i_s''} &= \mathrm{i_s(T_{s,up})} \\ \mathrm{i_s'} &= \mathrm{i_s(T_{QF})} \\ \mathrm{T_{QF}} &= \mathrm{T_{sat}} + \Delta\mathrm{T} \end{aligned} \tag{4-18}$$

ΔT is a user-defined parameter typically in the range $[0 - 20\ K]$.

Besides, the temperature of gas right above the interface is defined as being between saturation temperature and the bulk temperature of the sub-cell *up*, i.e.

$$\mathrm{T_g''} = (1 - \phi)\mathrm{T_{sat}} + \phi\mathrm{T_{g,up}} \tag{4-19}$$

ϕ is a user-defined parameter with $\phi \in [0,1]$.

The density ρ_g'' and the enthalpy i_g'' are then calculated from the equation of state as functions of T_g'' and the pressure ahead of the quench front, $p_{g,up}$.

$$\mathrm{\rho_g''} = \mathrm{\rho_g(p_{g,up}, T_g'')} \tag{4-20}$$

$$\mathrm{i_g''} = \mathrm{i_g(p_{g,up}, T_g'')} \tag{4-21}$$

4.4.3 Resolution of the momentum conservation equations at the quench front

The general expression of the momentum conservation equations at the quench front is analogue to the one already presented in 2.2.2 for a standard fixed face, that is:

$$\left(\mathrm{K_{gs}^{lam} + K_{gs}^{turb}}|\vec{\mathrm{u}}_\mathrm{g}|\right)\vec{\mathrm{u}}_\mathrm{g} + \frac{1}{\mathrm{s_g}}\left(\mathrm{K_{gl}^{lam} + K_{gl}^{turb}}|\vec{\mathrm{u}}_\mathrm{g} - \vec{\mathrm{u}}_\mathrm{l}|\right)\left(\vec{\mathrm{u}}_\mathrm{g} - \vec{\mathrm{u}}_\mathrm{l}\right) + \overrightarrow{\nabla \mathrm{p}} - \rho_\mathrm{g}\vec{\mathrm{g}} = 0 \tag{4-22}$$

for the gas and

$$\left(\mathrm{K_{ls}^{lam} + K_{ls}^{turb}}|\vec{\mathrm{u}}_\mathrm{l}|\right)\vec{\mathrm{u}}_\mathrm{l} - \frac{1}{\mathrm{s_l}}\left(\mathrm{K_{gl}^{lam} + K_{gl}^{turb}}|\vec{\mathrm{u}}_\mathrm{g} - \vec{\mathrm{u}}_\mathrm{l}|\right)\left(\vec{\mathrm{u}}_\mathrm{g} - \vec{\mathrm{u}}_\mathrm{l}\right) + \overrightarrow{\nabla \mathrm{p}} - \rho_\mathrm{l}\vec{\mathrm{g}} = 0 \tag{4-23}$$

for the liquid.

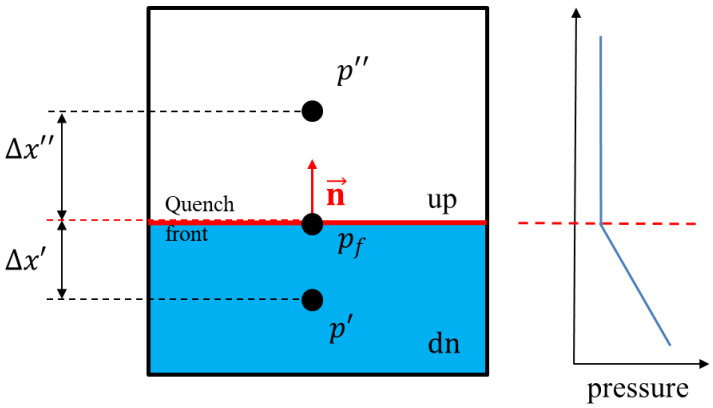

Figure 52 : Pressure gradient at the quench front

Nevertheless, the discretization of the equations (4-22) and (4-23) for the sub-cell *dn* yields respectively:

$$\left(K'^{lam}_{gs} + K'^{turb}_{gs}|u'_g|\right)u'_g + \frac{1}{s'_g}\left(K'^{lam}_{gl,dn} + K'^{turb}_{gl,dn}|u'_g - u'_l|\right)\left(u'_g - u'_l\right) + \frac{p_f - p'}{\Delta x'} - \rho'_g g = 0 \quad (4\text{-}24)$$

and

$$\left(K'^{lam}_{ls} + K'^{turb}_{ls}|u'_l|\right)u'_l - \frac{1}{s'_l}\left(K'^{lam}_{gl,dn} + K'^{turb}_{gl,dn}|u'_g - u'_l|\right)\left(u'_g - u'_l\right) + \frac{p_f - p'}{\Delta x'} - \rho'_l g = 0 \quad (4\text{-}25)$$

With p_f the pressure at the centre of the quench front, and $\Delta x'$, the distance between x_f the centre of the quench front surface and x_{dn} the centroid of sub-cell *dn*, like it is shown on Figure 52.

Here, u'_g, u'_l, $\Delta x'$ and g are the vector components perpendicular to the surface, with respect to $\vec{n}_f$ the surface normal vector of the quench front:

$$u'_g = \overrightarrow{u'_g} \cdot \vec{n}_f$$

$$u'_l = \overrightarrow{u'_l} \cdot \vec{n}_f$$

$$\Delta x' = (\vec{x}_f - \vec{x}_{dn}) \cdot \vec{n}_f$$

$$g = \vec{g} \cdot \vec{n}_f$$

For the sub-cell *up*, the discretized form of (4-22) yields

$$\left(K''^{\mathrm{lam}}_{\mathrm{gs}} + K''^{\mathrm{turb}}_{\mathrm{gs}}|u''_{\mathrm{g}}|\right)u''_{\mathrm{g}} + \frac{p'' - p_{\mathrm{f}}}{\Delta x''} - \rho''_{\mathrm{g}}g = 0 \tag{4-26}$$

With $\Delta x''$, the distance between x_f the centre of the quench front surface and x_{up} the centroid of sub-cell *up*, like it is shown on Figure 52.

For given values of u'_g and u'_l one can calculate u_{QF} from equation (4-15) and then u''_g from equation (4-27), which is deduced from equation (4-13).

$$u''_{\mathrm{g}} = \frac{\varepsilon s''_{\mathrm{g}}\rho''_{\mathrm{g}}u_{\mathrm{QF}} + \varepsilon s'_{\mathrm{l}}\rho'_{\mathrm{l}}\left(u'_{\mathrm{l}} - u_{\mathrm{QF}}\right) + \varepsilon s'_{\mathrm{g}}\rho'_{\mathrm{g}}\left(u'_{\mathrm{g}} - u_{\mathrm{QF}}\right)}{\varepsilon s''_{\mathrm{g}}\rho''_{\mathrm{g}}} \tag{4-27}$$

In order to eliminate p_f, one can solve equation (4-26) for p_f:

$$p_{\mathrm{f}} = p'' + \Delta x''\left[\left(K''^{\mathrm{lam}}_{\mathrm{gs}} + K''^{\mathrm{turb}}_{\mathrm{gs}}|u''_{\mathrm{g}}|\right)u''_{\mathrm{g}} - \rho''_{\mathrm{g}}g\right] \tag{4-28}$$

and insert the result in equations (4-24) and (4-25). Then the momentum conservation equations for gas in the sub-cell *dn* reads

$$\begin{aligned}\left(K'^{\mathrm{lam}}_{\mathrm{gs}} + K'^{\mathrm{turb}}_{\mathrm{gs}}|u'_{\mathrm{g}}|\right)u'_{\mathrm{g}} + \frac{1}{s'_{\mathrm{g}}}\left(K'^{\mathrm{lam}}_{\mathrm{gl,dn}} + K'^{\mathrm{turb}}_{\mathrm{gl,dn}}|u'_{\mathrm{g}} - u'_{\mathrm{l}}|\right)\left(u'_{\mathrm{g}} - u'_{\mathrm{l}}\right)\\ + \frac{\Delta p}{\Delta x'} - \rho'_{\mathrm{g}}g + \frac{\Delta x''}{\Delta x'}\left[\left(K''^{\mathrm{lam}}_{\mathrm{gs}} + K''^{\mathrm{turb}}_{\mathrm{gs}}|u''_{\mathrm{g}}|\right)u''_{\mathrm{g}} - \rho''_{\mathrm{g}}g\right] = 0\\ = \mathrm{Resi}^{\mathrm{mo}}_{\mathrm{g}}\end{aligned} \tag{4-29}$$

and for the liquid

$$\begin{aligned}\left(K'^{\mathrm{lam}}_{\mathrm{ls}} + K'^{\mathrm{turb}}_{\mathrm{ls}}|u'_{\mathrm{l}}|\right)u'_{\mathrm{l}} - \frac{1}{s'_{\mathrm{l}}}\left(K'^{\mathrm{lam}}_{\mathrm{gl,dn}} + K'^{\mathrm{turb}}_{\mathrm{gl,dn}}|u'_{\mathrm{g}} - u'_{\mathrm{l}}|\right)\left(u'_{\mathrm{g}} - u'_{\mathrm{l}}\right)\\ + \frac{\Delta p}{\Delta x'} - \rho'_{\mathrm{l}}g + \frac{\Delta x''}{\Delta x'}\left[\left(K''^{\mathrm{lam}}_{\mathrm{gs}} + K''^{\mathrm{turb}}_{\mathrm{gs}}|u''_{\mathrm{g}}|\right)u''_{\mathrm{g}} - \rho''_{\mathrm{g}}g\right] = 0\\ = \mathrm{Resi}^{\mathrm{mo}}_{\mathrm{l}}\end{aligned} \tag{4-30}$$

with

$$\Delta p = p'' - p'$$

For given properties in the sub-cells ($p', \varepsilon', s_g', s_l', p'', \varepsilon'', s_g'', s_l'', ...$) equations (4-29) and (4-30) can be solved numerically, for the velocities $u'_g$and u'_l. This is done by applying the Newton's iteration method, like it was the case for standard fixed meshing. Let's write

$$\mathbf{x} = \begin{pmatrix} \mathrm{u'_g} \\ \mathrm{u'_l} \end{pmatrix}, \qquad \mathbf{F}(\mathbf{x}) = \begin{pmatrix} \mathrm{Resi_g^{mo}(u'_g, u'_l)} \\ \mathrm{Resi_l^{mo}(u'_g, u'_l)} \end{pmatrix} = 0 \tag{4-31}$$

where $Resi_g^{mo}$ and $Resi_l^{mo}$ are the left hand sides of equations (4-29) and (4-30), respectively.

If $\boldsymbol{x}^n$ denotes an approximate solution at iteration step n, and $\boldsymbol{x}^{n+1} = \boldsymbol{x}^n + \Delta\boldsymbol{x}$ the improved solution at iteration step $n+1$, a truncated Taylor series expansion yields

$$\mathbf{F}(\mathbf{x}^{\mathrm{n}} + \Delta\mathbf{x}) = \mathbf{F}(\mathbf{x}^{\mathrm{n}}) + \frac{\partial \mathbf{F}}{\partial \mathbf{x}}\Delta\mathbf{x} = 0 \tag{4-32}$$

Solving for $\Delta\boldsymbol{x}$ yields the iteration rule to calculate an improved approximate solution $\boldsymbol{x}^{n+1}$,

$$\mathbf{x}^{\mathrm{n+1}} = \mathbf{x}^{\mathrm{n}} + \Delta\mathbf{x} = \mathbf{x}^{\mathrm{n}} - \left(\frac{\partial \mathbf{F}}{\partial \mathbf{x}}\right)^{-1} \mathbf{F}(\mathbf{x}^{\mathrm{n}}) \tag{4-33}$$

Here, the Jacobian matrix $\frac{\partial \boldsymbol{F}}{\partial \boldsymbol{x}}$ is a 2 x 2 matrix, composed of the partial derivatives of the residuals of $Resi_g^{mo}$ and $Resi_l^{mo}$ with respect to the velocities u'_g and u'_l

$$\frac{\partial \mathbf{F}}{\partial \mathbf{x}} = \begin{pmatrix} \dfrac{\partial \mathrm{Resi_g^{mo}}}{\partial \mathrm{u'_g}} & \dfrac{\partial \mathrm{Resi_g^{mo}}}{\partial \mathrm{u'_l}} \\ \dfrac{\partial \mathrm{Resi_l^{mo}}}{\partial \mathrm{u'_g}} & \dfrac{\partial \mathrm{Resi_l^{mo}}}{\partial \mathrm{u'_l}} \end{pmatrix} \tag{4-34}$$

For simplicity, the partial derivatives $\frac{\partial Resi_g^{mo}}{\partial u'_g}$, $\frac{\partial Resi_g^{mo}}{\partial u'_l}$, $\frac{\partial Resi_l^{mo}}{\partial u'_g}$ and $\frac{\partial Resi_l^{mo}}{\partial u'_l}$ are approximated by finite differences:

$$\frac{\partial \mathrm{Resi_g^{mo}}}{\partial \mathrm{u'_g}} \approx \frac{\mathrm{Resi_g^{mo}(u'_g + \Delta u'_g, u'_l)} - \mathrm{Resi_g^{mo}(u'_g, u'_l)}}{\Delta \mathrm{u'_g}} \tag{4-35}$$

$$\frac{\partial \mathrm{Resi_l^{mo}}}{\partial \mathrm{u'_g}} \approx \frac{\mathrm{Resi_l^{mo}(u'_g + \Delta u'_g, u'_l)} - \mathrm{Resi_l^{mo}(u'_g, u'_l)}}{\Delta \mathrm{u'_g}} \tag{4-36}$$

$$\frac{\partial \mathrm{Resi_g^{mo}}}{\partial \mathrm{u'_l}} \approx \frac{\mathrm{Resi_g^{mo}(u'_g, u'_l + \Delta u'_l)} - \mathrm{Resi_g^{mo}(u'_g, u'_l)}}{\Delta \mathrm{u'_l}} \tag{4-37}$$

$$\frac{\partial \mathrm{Resi_l^{mo}}}{\partial \mathrm{u'_l}} \approx \frac{\mathrm{Resi_l^{mo}(u'_g, u'_l + \Delta u'_l)} - \mathrm{Resi_l^{mo}(u'_g, u'_l)}}{\Delta \mathrm{u'_l}} \tag{4-38}$$

The increments for the variables are chosen so that the second half of the significant digits is perturbed:

$$\Delta u'_g = 10^{-8} \cdot \max(|u'_g|, 10^{-2}) \tag{4-39}$$

$$\Delta u'_l = 10^{-8} \cdot \max(|u'_l|, 10^{-2}) \tag{4-40}$$

Starting from an initial guess for the velocities, the iterative solution procedure given by equation (4-33) is repeated until the norm of the corrections $\|\Delta \boldsymbol{x}\|$ has diminished below a prescribed threshold. Then the numerical solution is assumed to have converged to the true solution within an acceptable tolerance.

4.4.4 Determination of the new grid geometry

Knowing the quench front velocity, the volume ΔV quenched in a time increment Δt can be calculated, according to equation (4-6) from:

$$\Delta V = A_{QF} \cdot u_{QF} \cdot \Delta t \tag{4-41}$$

where A_{QF} is the cross section area of a cell face which splits an original cell into sub-cells and is part of the quench front.

As already mentioned in 4.3.2, the new volumes of the quenched (*dn*) and unquenched (*up*) sub-cells and the respective fraction of the volume of the sub-cell *dn* to the total volume of the un-split cell can be calculated as

$$\begin{aligned} V_{dn} &= V_{dn}^{old} + \Delta V \\ V_{up} &= V_{up}^{old} - \Delta V \\ CVF &= \frac{V_{dn}}{V_{dn} + V_{up}} = \frac{V_{dn}}{V} \end{aligned} \tag{4-42}$$

Knowing the volume fractions CVF at the new time level *t*, the new grid topology can be computed by executing the algorithm for grid reconstruction discussed in 4.3.2. Nevertheless, this algorithm is not conservative, i.e. it is not guaranteed that the volumes of the sub-cells resulting

from the partitioning according to the CVF-function strictly equal $[CVF \cdot V]$ and $[(1 - CVF) \cdot V]$. Therefore, only the face properties (normal vector, area) of the partitioned grid are used for the calculation of fluxes. For the cell volumes, the values calculated from equation (4-42) satisfying the conservation law should be used.

4.4.5 Modification of conservation equations to take into account moving cell faces

4.4.5.1 General form

Using first order implicit time discretization, the discretized mass conservation equation for a phase k in a cell i with moving grid faces can be written in the general form

$$\frac{\alpha_{k,i}\rho_{k,i}V_i - \alpha_{k,i}^{old}\rho_{k,i}^{old}V_i^{old}}{\Delta t} + \sum_{j=1}^{N_f}\left[\alpha_{k,j}\rho_{k,j}\left(\vec{u}_{k,j} - \vec{u}_{f,j}\right)\cdot\vec{A}_j^{old}\right] = \Gamma_{k,i}V_i \tag{4-43}$$

With $\alpha_{k,i} = \begin{cases} s_{g,i}\varepsilon_i \,, if\ k = g \\ s_{l,i}\varepsilon_i \,, if\ k = l \\ (1-\varepsilon_i) \,, if\ k = s \end{cases}$

Here, the index j denotes the properties at the cell faces, while the index i denotes the cell averaged properties. Keeping in mind, that

$$V_i = V_i^{old} + \Delta V = V_i^{old} + \Delta t\sum_{j=1}^{N_f}\left(\vec{u}_{f,j}\cdot\vec{A}_j^{old}\right) \tag{4-44}$$

and inserting it into equation (4-43) gives

$$V_i^{old}\frac{\alpha_{k,i}\rho_{k,i} - \alpha_{k,i}^{old}\rho_{k,i}^{old}}{\Delta t} + \sum_{j=1}^{N_f}\left(\alpha_{k,j}\rho_{k,j}\vec{u}_{k,j}\cdot\vec{A}_j^{old}\right) + \alpha_{k,i}\rho_{k,i}\sum_{j=1}^{N_f}\left(\vec{u}_{f,j}\cdot\vec{A}_j^{old}\right) - \sum_{j=1}^{N_f}\left(\alpha_{k,j}\rho_{k,j}\vec{u}_{f,j}\cdot\vec{A}_j^{old}\right) = \Gamma_{k,i}V_i \tag{4-45}$$

This can be re-arranged to give

$$V_i^{old}\frac{\alpha_{k,i}\rho_{k,i}-\alpha_{k,i}^{old}\rho_{k,i}^{old}}{\Delta t}+\sum_{j=1}^{N_f}\left(\alpha_{k,j}\rho_{k,j}\vec{u}_{k,j}\cdot\vec{A}_j^{old}\right)$$
$$=\Gamma_{k,i}V_i\ +\sum_{j=1}^{N_f}\left(\alpha_{k,j}\rho_{k,j}-\alpha_{k,i}\rho_{k,i}\right)\cdot\left(\vec{u}_{f,j}\cdot\vec{A}_j^{old}\right) \quad (4\text{-}46)$$

With the exception of the last term on the right-hand side this is the same formulation as for a fixed grid. Note that for un-split cells the volume remains constant, i.e. $V_i^{old}=V_i$ and $\vec{u}_f=0$. In split cells, with exception of the face representing the quench front, all other faces are stationary.

Similarly, the energy conservation equation for phase k in cell i can be expressed by

$$V_i^{old}\frac{\alpha_{k,i}\rho_{k,i}e_{k,i}-\alpha_{k,i}^{old}\rho_{k,i}^{old}e_{k,i}^{old}}{\Delta t}+\sum_{j=1}^{N_f}\left(\alpha_{k,j}\rho_{k,j}i_{k,j}\vec{u}_{k,j}\cdot\vec{A}_j^{old}\right)$$
$$=Q_{k,i}V_i\ -\sum_{j=1}^{N_f}\left(k_{eff,k,j}\cdot\nabla T_{k,j}\cdot\vec{A}_j^{old}\right)+\sum_{j=1}^{N_f}\left(\alpha_{k,j}\rho_{k,j}i_{k,j}-\alpha_{k,i}\rho_{k,i}i_{k,i}\right)\cdot\left(\vec{u}_{f,j}\cdot\vec{A}_j^{old}\right) \quad (4\text{-}47)$$

Here, the terms $Q_{k,i}$ represents various volumetric heat sources coming e.g. from volumetric heating, phase change, chemical reactions or heat exchange with other phases.

Taking into account the considerations in 4.4.2, the discretized form of mass and energy conservation equations for the cold and hot sub-cells can be explicitly expressed.

4.4.5.2 Mass and energy conservation equations for the cold sub-cell *dn*

For conservation of mass in the cold sub-cell *dn*, the state at the quench front is approximated by taking the upwind state. In other words, for fluxes leaving the cell we have $(\cdot)_j=(\cdot)_{dn}$. Thus, for the gas phase, equation (4-46) becomes

$$V_{dn}^{old}\frac{\alpha_{g,dn}\rho_{g,dn}-\alpha_{g,dn}^{old}\rho_{g,dn}^{old}}{\Delta t}+\sum_{\substack{j=1\\ j\neq QF}}^{N_f}\left(\alpha_{g,j}\rho_{g,j}\vec{u}_{g,j}\cdot\vec{A}_j^{old}\right)+\alpha_{g,dn}\rho_{g,dn}u_g'A_{QF} = -\Gamma_{evap,dn}V_{dn} \tag{4-48}$$

The energy conservation equation of the gas phase yields

$$V_{dn}^{old}\frac{\alpha_{g,dn}\rho_{g,dn}e_{g,dn}-\alpha_{g,dn}^{old}\rho_{g,dn}^{old}e_{g,dn}^{old}}{\Delta t}+\sum_{\substack{j=1\\ j\neq QF}}^{N_f}\left(\alpha_{g,j}\rho_{g,j}i_{g,j}\vec{u}_{g,j}\cdot\vec{A}_j^{old}\right) +\alpha_{g,dn}\rho_{g,dn}i_{g,dn}u_g'A_{QF} = Q_{g,dn}V_{dn}-\sum_{j=1}^{N_f}\left(k_{eff,g,j}\cdot\nabla T_{g,j}\cdot\vec{A}_j^{old}\right) \tag{4-49}$$

Note that the last terms in equations (4-46) and (4-47) cancel out due to the upwind treatment of convective terms, $(\cdot)_j = (\cdot)_{dn}$. Concerning the third terms in equations (4-48) to (4-51), it is implicitly assumed that the normal of the face representing the quench front points out of sub-cell *dn* (otherwise, the sign would change).

Analogously, the discrete mass conservation equation for the liquid in the sub-cell *dn* becomes

$$V_{dn}^{old}\frac{\alpha_{l,dn}\rho_{l,dn}-\alpha_{l,dn}^{old}\rho_{l,dn}^{old}}{\Delta t}+\sum_{\substack{j=1\\ j\neq QF}}^{N_f}\left(\alpha_{l,j}\rho_{l,j}\vec{u}_{l,j}\cdot\vec{A}_j^{old}\right)+\alpha_{l,dn}\rho_{l,dn}u_l'A_{QF} = \Gamma_{evap,dn}V_{dn} \tag{4-50}$$

and the energy conservation equation

$$V_{dn}^{old}\frac{\alpha_{l,dn}\rho_{l,dn}e_{l,dn}-\alpha_{l,dn}^{old}\rho_{l,dn}^{old}e_{l,dn}^{old}}{\Delta t}+\sum_{\substack{j=1\\ j\neq QF}}^{N_f}\left(\alpha_{l,j}\rho_{l,j}i_{l,j}\vec{u}_{l,j}\cdot\vec{A}_j^{old}\right) + \alpha_{l,dn}\rho_{l,dn}i_{l,dn}u_l'A_{QF} = Q_{l,dn}V_{dn}-\sum_{j=1}^{N_f}\left(k_{eff,l,j}\cdot\nabla T_{l,j}\cdot\vec{A}_j^{old}\right) \tag{4-51}$$

For the solid phase, the mass conservation equation simplifies to

$$V_{dn}^{old}\frac{\alpha_{s,dn}\rho_{s,dn}-\alpha_{s,dn}^{old}\rho_{s,dn}^{old}}{\Delta t}=0\ \rightarrow \alpha_{s,dn}\rho_{s,dn}=\alpha_{s,dn}^{old}\rho_{s,dn}^{old} \tag{4-52}$$

and the discrete energy conservation equation reads

$$\begin{aligned}&V_{dn}^{old}\frac{\alpha_{s,dn}\rho_{s,dn}e_{s,dn}-\alpha_{s,dn}^{old}\rho_{s,dn}^{old}e_{s,dn}^{old}}{\Delta t}\\&=Q_{s,dn}V_{dn}-\sum_{j=1}^{N_f}\left(k_{eff,s,j}\cdot\nabla T_{s,j}\cdot\vec{A}_j^{old}\right)+u_{QF}A_{QF}\alpha_{s,dn}\rho_{s,dn}\left(i_s'-i_{s,dn}\right)\end{aligned} \tag{4-53}$$

Here, i_s' is different to $i_{s,dn}$ and has to be calculated according to equation (4-18).

4.4.5.3 Mass and energy conservation equations for the dry sub-cell *up*

Since it has been assumed that no liquid exists in the hot sub-cell, the associated mass and energy conservation equations do not have to be considered. For the conservation of gas mass though, one has:

$$\begin{aligned}&V_{up}^{old}\frac{\alpha_{g,up}\rho_{g,up}-\alpha_{g,up}^{old}\rho_{g,up}^{old}}{\Delta t}+\sum_{\substack{j=1\\j\neq QF}}^{N_f}\left(\alpha_{g,j}\rho_{g,j}\vec{u}_{g,j}\cdot\vec{A}_j^{old}\right)-\alpha_g''\rho_g''u_g''A_{QF}\\&=u_{QF}A_{QF}\left(\alpha_g''\rho_g''-\alpha_{g,up}\rho_{g,up}\right)\end{aligned} \tag{4-54}$$

Note that $\alpha_{g,up}=\alpha_g''=\varepsilon_{up}$. ρ_g'' is obtained according to equations (4-19) and (4-20).

Energy conservation for the gas phase gives

$$\begin{aligned}&V_{up}^{old}\frac{\alpha_{g,up}\rho_{g,up}e_{g,up}-\alpha_{g,up}^{old}\rho_{g,up}^{old}e_{g,up}^{old}}{\Delta t}+\sum_{\substack{j=1\\j\neq QF}}^{N_f}\left(\alpha_{g,j}\rho_{g,j}i_{g,j}\vec{u}_{g,j}\cdot\vec{A}_j^{old}\right)-\alpha_g''\rho_g''i_g''u_g''A_{QF}\\&=Q_{g,up}V_{up}-\sum_{j=1}^{N_f}\left(k_{eff,g,j}\cdot\nabla T_{g,j}\cdot\vec{A}_j^{old}\right)+u_{QF}A_{QF}\left(\alpha_g''\rho_g''i_g''-\alpha_{g,up}\rho_{g,up}i_{g,up}\right)\end{aligned} \tag{4-55}$$

The properties ahead of the quench front, ρ_g'' and e_g'', are calculated from equations (4-19) to (4-21).

Like for the cold sub-cell, the mass conservation equation for the solid phase simplifies to

$$\alpha_{s,up}\rho_{s,up} = \alpha_{s,up}^{old}\rho_{s,up}^{old} \tag{4-56}$$

Therefore, the discrete energy conservation equation for the solid phase reads

$$V_{up}^{old}\alpha_{s,up}^{old}\rho_{s,up}^{old}\frac{e_{s,up} - e_{s,up}^{old}}{\Delta t} = Q_{s,up}V_{up} - \sum_{j=1}^{N_f}\left(k_{eff,s,j}\cdot\nabla T_{s,j}\cdot\vec{A}_j^{old}\right) - u_{QF}A_{QF}\alpha_{s,up}^{old}\rho_{s,up}^{old}\left(i_s'' - i_{s,up}\right) \tag{4-57}$$

However, according to (4-18), $i_s'' = i_{s,up}$, and thus, the last term of the right-hand side cancels out.

4.4.6 Resolution of the conservation equation system

In the numerical solution procedure in COCOMO-3D the mass and momentum conservation equations for gas and liquid are solved simultaneously for the gas and liquid velocities as well as the pressure and the liquid saturations. For this, first the gas and liquid velocities at cell faces are calculated for given values of liquid saturation and pressure in the cells. Then the mass conservation equations are used to solve for liquid saturation and pressure. This requires to know the partial derivatives of liquid and gas velocities (or of mass fluxes) with respect to the saturation and pressure differences across cell faces. The method for regular cell faces is described in [66]. Here, the method to calculate the required derivatives in the case where the face represents a quench front is described in Appendix-I.

Solving the energy conservation equations for T_g, T_l and T_s is achieved analogously to the standard version of COCOMO-3D, and therefore does not need to be adapted and further developed in this chapter.

4.5 The new general algorithm

After having developed the main aspects of the present improvement work on the quench front modelling, the quench front reconstruction method and the procedure to solve the conservation equation system must be considered together and embodied in the whole resolution algorithm, which was exposed on Figure 10 (section 2.4). Before exposing the new resolution pattern, it is worth to talk about another important point regarding the beginning of the resolution loop at each time step: the initialization of the grid.

4.5.1 Initialization of the grid

From the results obtained at the end of the resolution loop of a certain time level, some original cells got split, some others recover their original state, or some cells already split remain split but present a new geometry. The original grid is set once at the very beginning of the simulation and remains untouched during the whole simulation. Indeed, the original cells are still needed as reference for the calculation of *CVF* and thus for the quench front reconstruction. However, resolution procedure of the balance conservation equations is applied on another grid, so-called "active grid", on which all active original cells (i.e. un-split cells) and currently existing sub-cells are indexed.

4.5.1.1 Creation / suppression of sub-cells

Original cells that happen to be split are not deleted per se, but "deactivated" from the active grid, while two new associated elements "sub-cells" are allocated into the active grid. While initialization of the geometry (centroid position, face area, volume) of cells and sub-cells is easy to process, the initialisation of the physical quantities must be handled carefully, in order to avoid instabilities. Three configurations are possible.

- Initialization of sub-cells from an original cell that was not split at the previous time level:

If the original cell was a dry cell, and the unquenched sub-cell *up* presents the major volume (i.e. *CVF < 0.5*), then the sub-cell *up* takes over the gas properties calculated for the original cell (such as T_g, p_g), while the quenched sub-cell takes the fluid properties from its next quenched neighbour ($s_g, T_g, p_g\ s_l, T_l, p_l$). Inversely, if the original cell was a quenched cell, and the quenched sub-cell *dn* presents the major volume (i.e. *(1-CVF) < 0.5*), then the sub-cell *dn* takes over the fluid properties calculated for the original cell ($s_g, T_g, p_g\ s_l, T_l, p_l$), while the unquenched sub-cell takes the gas properties from its next unquenched neighbour (s_g, T_g, p_g). As for the initialization of extensive quantities such as the mass and the energy, one rather refers to volume related quantities, like the density (kg/m³) or indirectly the specific internal energy (J/kg). The method to determine the next neighbouring cell is explained in the next sub-section 4.5.1.2.

- Re-activation of an original cell that was split at the previous time level:

If the re-activated cell is flagged as "quenched", cell takes over the properties computed for the last quenched sub-cell. Inversely, if flagged as "unquenched", the cell would inherit the properties computed for the dry sub-cell.

- Initialization of sub-cells that already existed at the previous time level:

In this case, geometry and physical quantities are simply updated.

4.5.1.2 Creation / suppression of merged cells

This subsection presents another relevant reconstruction feature. In order to prevent infinitely small sub-cell, or working with very low void fraction both leading to numerical instabilities as mentioned in section 3.5, sub-cells are merged to their next neighbour of the same type (quenched or unquenched), when their volume lays under a certain threshold (here, if *CVF < 0.*1 or if *(1-CVF) < 0.1*), like shown below on Figure 53.

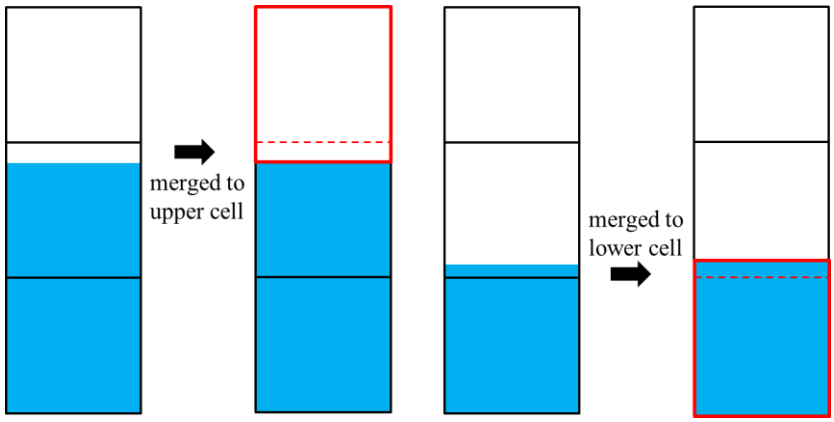

Figure 53 : Illustration of 1D sub-cell / cell merging

In 1D, the next neighbour cell is pretty obvious to find out, since there is only one possibility. In 2D however, a rule must be defined to determine the cell that the sub-cell is going to be merged to. In order to do this, the distances between the quench front centroid and the intersection of the quench front normal with the sub-cell faces are calculated and compared (see Figure 54). The intersected face showing the shortest distance to the quench front centroid is assumed to be the nearest face. The sub-cell is then merged to the cell sharing this face in common.

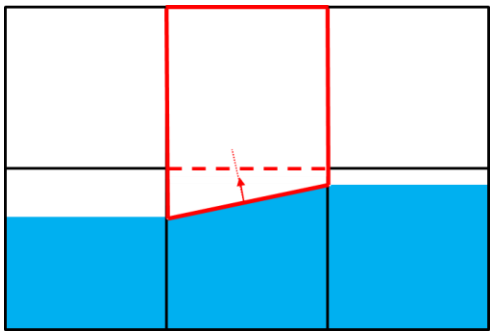

Figure 54 : Illustration of 2D merging sub-cell / next neighbour cell

Analog to the initialization of sub-cells, three configurations must be distinguished.

- Initialization of merged cells that did not exist at the previous time level:

Physical quantities of the merged cell, e.g. the pressure or the temperature, are computed by volume-weighted averaging of the quantities of the sub-cell and of the associated original cell to be merged to. Extensive quantities, like the fluid masses, are basically integrated (by addition).

- Initialization of sub-cells and re-activation of original cells from merged cells:

Physical quantities computed for the merged cell are attributed to the re-activated original cell and to the resulting sub-cell.

- Initialization of merged cells that already existed at the previous time level:

In this case, geometry and physical quantities are simply updated.

4.5.2 Resolution pattern

The revised resolution scheme is summarized on Figure 55, where the contributions of the present work to the original code are represented in red. Like for the resolution scheme presented in Chapter 2 (Figure 10), it described the whole procedure applied on each active cell and sub-cell, during a time step Δt, between a previous time level t^{old} and the new time level t. At the beginning of the resolution loop, the quench front is already reconstructed based on the *CVF*s, which have been deduced from the results of the previous time level. First, steam and water velocity, u_g and u_l, are calculated at each un-split face of the whole computation domain, by solving the momentum conservation equations. If a face happens to be a quench front, u_g' and u_l' are obtained by solving the momentum conservation equation dedicated to the quench front; quench front velocity u_{QF} is obtained from (4-15), while u_g'' is deduced by (4-27) knowing u_g', u_l' and u_{QF}. In order to solve the momentum conservation equations, values of quantities like the pressure, the saturation, the density, must be guessed. As initial guess, the values found during the resolution of the previous time level are used.

As already mentioned, mass flows are simply derived from velocities. However, it has to be checked if the faces are moving or not (i.e. interfaces or not). If a face is moving, one has to take into account the velocity of the face u_{QF}. By integrating the mass flows at the boundaries of each cell, and adding the evaporation rate (also deduced from values computed during the previous time level) one estimates the mass residuum from the mass conservation equations, like shown in details in the last chapter. The unknowns p_g and s_l are calculated by solving the mass conservation equation for steam and water of each cell. Concerning quenched sub-cells *dn*, p_g^{dn}

and s_l^{dn} are calculated, while only p_g^{up} is of particular interest for the unquenched sub-cell *up*. New steam pressure and liquid saturation must be found, such that the mass residuum of steam and liquid are equal to 0, in order to respect the mass balance. From this, material properties, as well as steam and water mass, are updated. Thereafter velocities are also updated by solving again the momentum equations, but considering these newly updated quantities (new pressure, new volume fractions…). Subsequently, mass residuum for mass and steam can be newly estimated, using the re-calculated mass flows and evaporation rate.

After having estimated all the heat transfers within the debris bed ($Q_{s,sat}, Q_{s,g}, Q_{s,l}$), as well as the conductive heat flow, and knowing the source term $Q_{s,source}$ from the setting of the boundary conditions, energy residuum of the solid phase can be calculated. As an initial guess for e_s , the specific internal energy computed during the resolution of the previous time level is taken. Similarly, energy residuum of steam and water are also estimated, taking into account all the volume related heat transfer, but also the enthalpy fluxes, yielded by the mass transport at the cell boundaries. If the face is moving, u_{QF} must be considered. Moreover, in order to avoid an accumulation of numerical error, the energy from the mass excess (mass residuum) is subtracted, as a numerical heat loss. Thereafter one can solve the system and find the unknowns: T_s, T_g and T_l for original cells, or T_s^{dn}, T_g^{dn} and $T_l^{dn}$for sub-cells *dn*, and T_s^{up}, T_g^{up} for sub-cells *up*. Materials properties can be updated again with respect to these new temperatures.

The whole scheme is repeated until the values for pressures, volumes fractions, temperatures, mass and also cell volume converge. As soon as the convergence is reached, the obtained values can be stored as "old" values for the resolution of the next time level. Knowing the new u_{QF}, volumes of the quenched sub-cells (and so of unquenched sub-cells) are updated. From this, *CVF* of original cells are also updated. A split cell presenting a *CVF* under 0 or above 1, means that the cell becomes un-split and that the next cell previously quenched or dry, respectively, gets split. However, if the newly created sub-cells presents a volume under the threshold of 10% of the total cell volume, the sub-cell is merged to the cell that presented a *CVF* under 0 or above 1. Finally, averaged *CVF* are determined at each node in order to execute the reconstruction procedure of the quench front.

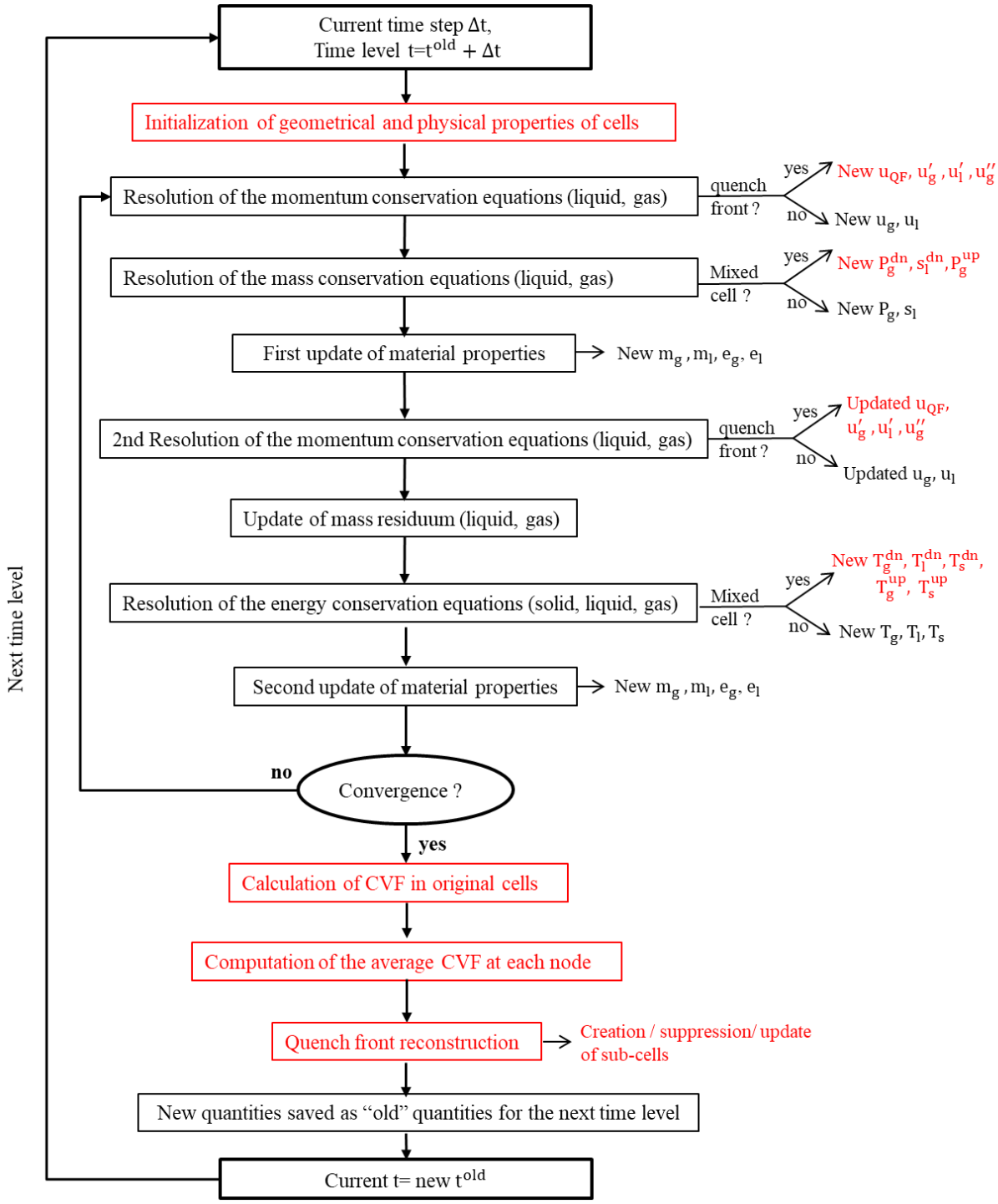

Figure 55 : Resolution pattern of the revised version of COCOMO-3D

.

5 Applications

In this chapter, the new quenching modelling is verified regarding the reconstruction of the quench front, the quench front progression (i.e. quenching time) as well as the associated steam generation. The capabilities to deal with reactor-scale cases are tested and compared to the 1D outcomes of the previous version of COCOMO-3D.

The setting of COCOMO-3D inputs with the new code version, for the different cases that are presented in this chapter, is exactly the same setting as with the previous standard code version, with only one exception: quench front must be initialized, too. Indeed, the quench front may not appear from nowhere, and thus, it has to be already present at the very beginning of the simulation. The present work focuses on the quenching modelling to be used in integral codes and not on the specific requirements to introduce this model into each integral code. For simplification reason, the quench front is defined such that at least one original cell is fully quenched, like depicted:

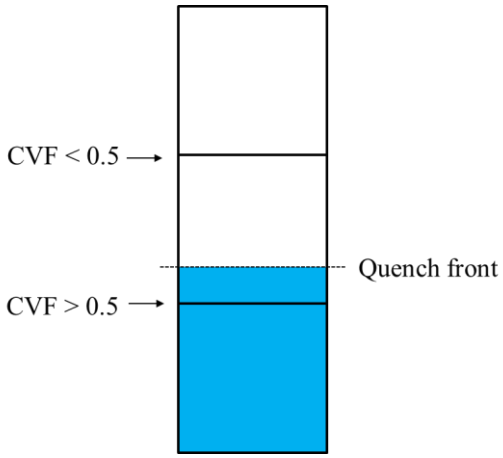

Doing this, the quench front depends on the *CVF* (= 1.0) of the lower cell (like explained in the previous chapter). Otherwise, if the quench front would have begun in the first cell, it would have required to define the *CVF* as boundary conditions, since no lower cell exists.

Tracking of the quench front is no longer based on the saturation temperature, like it was the case in chapter 3, but basically on the actual position of the reconstructed interface.

5.1 Model verification

5.1.1 Quench front progression by constant bottom-flooding

This part checks if the friction model, e.g. the momentum conservation equations, and also the mass conservation equations are still valid with the presence of moving boundaries, i.e. quench front interface.

To do this, one reproduces in COCOMO-3D a simple debris bed, which is defined on a Cartesian coordinates system, with a section of 1 x 1 m (thus, 1 m²). In order to test big cells, a height of 2.0 m is set, like for the reactor-scale case in section 3.4. A porosity of 0.4 and an effective particle diameter of 2.9 mm are considered. To emphasize the analysis on the momentum and mass conservation equations, regardless of the effect of thermal exchanges and boiling (that is, assessing a monophasic flow in the porous medium), particle temperature as well as temperature of injection water are initialized to saturation temperature; thus, preventing any thermal exchange. The initial quench front position is set 10 cm above the bottom of the bed. Moreover, a small fully quenched cell is defined right under the bottom of the bed, in order to fulfil the requirements mentioned earlier in this chapter. Since no multidimensional effects are going to be observed (homogeneous bed, temperature profile and injection distribution), the bed is discretized only axially.

Quenching simulations are performed for two injection rates: 2.0 kg/s and 5.0 kg/s. Because injection is forced and no boiling occurs, the quench front velocity and the quenching time (time needed for the quench front to reach the top of the bed) are easy to determine exactly. Quench front progression is linearly proportional to the injection velocity. From equation (2-35), one can find the injection velocity, and so the quench front velocity, directly from the mass rate $\dot{m}_{inj}$:

$$u_{QF} = \frac{\dot{m}_{inj}}{\rho_l A_{bed} \varepsilon}, \tag{5-1}$$

with $A_{bed} = 1.0\ m^2$, area of the bed section. the quenching time t_Q is obtained as follows:

$$t_Q = \frac{z_h - z_o}{u_{QF}}, \tag{5-2}$$

with Z_o and Z_h, initial quench front elevation and elevation of the top of the bed (i.e. bed height), respectively. Given that the quench front lays initially at *z= 0.10 m* and the bed is 2 m-high, mass rates of 2.0 and 5.0 kg/s should yield these quenching times:

Mass flow (kg/s)	**Quench front velocity (m/s)**	**Quenching time (s)**
2.0	0.0052	365
5.0	0.0130	146

Simulations were performed with different nodalizations: 3 cells (cell size ~ 65 cm) to 50 cells (cell size ~ 4 cm). Figure 56 shows post-visualizations at three time points (t_0= 0 s; t= 160 s; t_Q= 360 s) for a debris bed discretized into 12 cells, on which one can observe the movement of the reconstructed quench front.

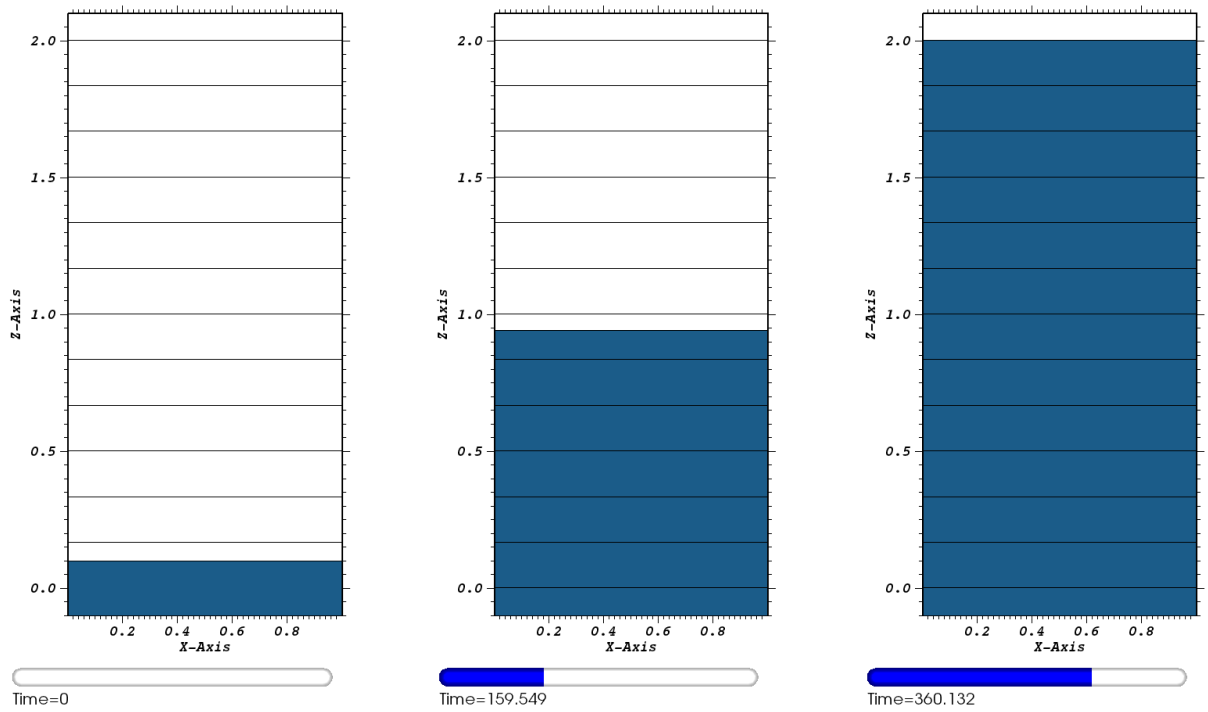

Figure 56 : 1D Simulation of flooding of a 2 m-high debris bed (injection: 2 kg/s)

Quench front progression and velocity for 3 (blue curve) and 50 cells (red curve) are reported together with the quench front progression and velocity calculated analytically (green curve) on

Figure 57 and Figure 58. From these graphs, one can see that the quench front progression under monophasic conditions is perfectly predicted as it matches the analytical results.

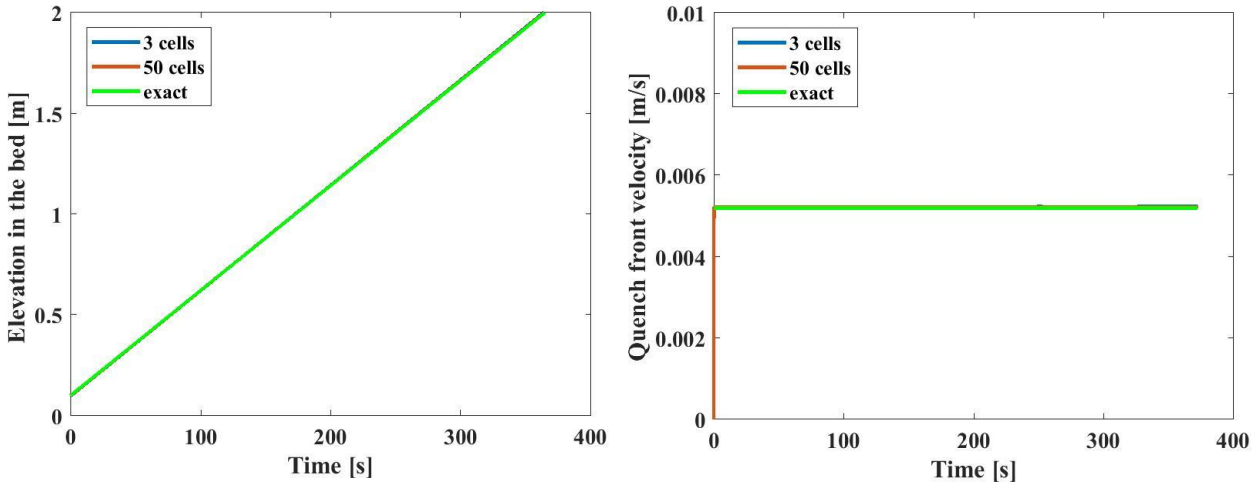

Figure 57 : Progression and velocity of the reconstructed Quench front ($\dot{m}_{inj}$ = 2 kg/s)

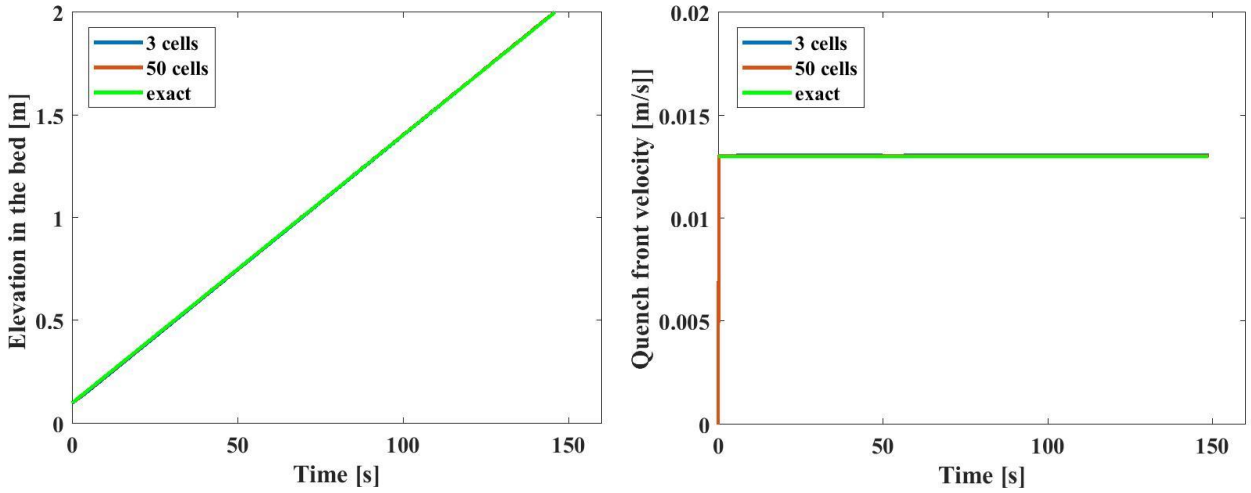

Figure 58 : Progression and velocity of the reconstructed Quench front ($\dot{m}_{inj}$ = 5 kg/s)

5.1.2 Quench front progression by gravity-driven injection

Simulation of the quenching with a gravity-driven injection, still at saturation temperature, allows for a further assessment of the friction model since the progression of the front depends on the local pressure losses. The bed configuration (geometry, porosity, temperature) are exactly the

same as in the previous section. Injection is now defined by a fixed pressure at the bottom inlet as boundary condition. However, the exact quench front progression is less trivial to determine analytically than in the previous case with constant injection rate. To do that, let's depict the problem as follows:

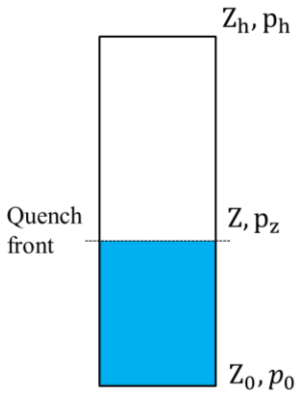

Z_0 and Z_h are respectively the initial quench front elevation and the elevation of top of the bed (i.e. bed height). p_0 and p_h are respectively the pressures at Z_0 (i.e. injection pressure set by the user) and at the top of the bed (system pressure, i.e. 1 bar). The pressure p_z at elevation *Z*, and *Z* the position of the quench front at time point *t*, remain both unknown. Then, for the pressure gradient in the dry zone (downstream of the front) and in the quenched zone (upstream of the front) under monophasic conditions, it gives:

$$\frac{p_z - p_h}{Z_h - Z} = \rho_g g + \frac{\varepsilon \eta_g}{\kappa} u_{QF} + \frac{\rho_g \varepsilon^2}{\mu} u_{QF}^2 \tag{5-3}$$

$$\frac{p_0 - p_z}{Z - Z_0} = \rho_l g + \frac{\varepsilon \eta_l}{\kappa} u_{QF} + \frac{\rho_l \varepsilon^2}{\mu} u_{QF}^2 \tag{5-4}$$

Equation (5-3) can also be rearranged as: $p_z = p_h + (\rho_g g + \frac{\varepsilon \eta_g}{\kappa} u_{QF} + \frac{\rho_g \varepsilon^2}{\mu} u_{QF}^2)(Z_h - Z)$

Inserting p_z into equation (5-4) yields a 2nd order equation (5-5), where only u_{QF} and Z are unknown.

$$\left(\frac{\rho_g \varepsilon^2}{\mu}(Z_h - Z) + \frac{\rho_l \varepsilon^2}{\mu}(Z - Z_0)\right) u_{QF}^2 + \left(\frac{\varepsilon \eta_g}{\kappa}(Z_h - Z) + \frac{\varepsilon \eta_l}{\kappa}(Z - Z_0)\right) u_{QF} + p_h - p_0 + \rho_g g(Z_h - Z) + \rho_l g(Z - Z_0) = 0 \tag{5-5}$$

Knowing that u_{QF} is the time derivative of Z:

$$u_{QF}(t) = \frac{dZ}{dt}$$

One has to solve the 2nd order equation (5-5) for u_{QF} in order to obtain an expression of u_{QF} as a function of *Z(t)*, which is an ordinary differential equation. Thereafter this differential equation must be solved in order to obtain Z as function of the time, and visualise the quench front progression. The MATLAB function "ODE45" helps solving this differential equation and yield the green curves on Figure 59 and Figure 60.

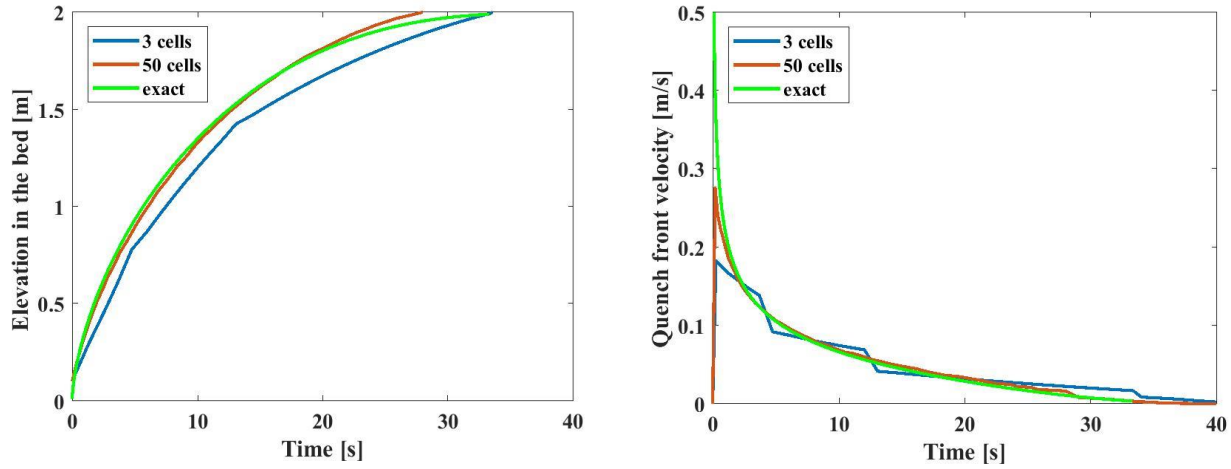

Figure 59 : Progression and velocity of the reconstructed Quench front (Hydrostatic Head = 2.0 m)

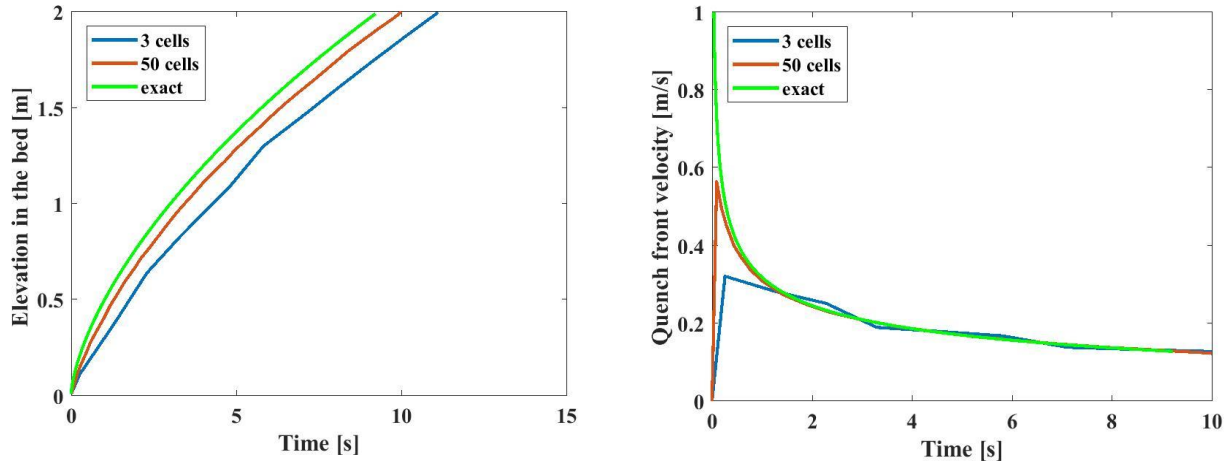

Figure 60 : Progression and velocity of the reconstructed Quench front (Hydrostatic Head = 5.0 m)

For a water column of about 2.0 m at the inlet (i.e. $p_0 = 118850\ Pa$), one observes a discrepancy of approximately 5 sec between the quenching time obtained by a 3-cell and 50-cell discretization. Nevertheless, both agrees quite well with the quench front progression obtained by means of MATLAB. The hyperbolic trend is also very well reproduced. Like expected, the quench front progression yielded by a hydrostatic head of 2.0 m stagnates near the top of the bed, because the head corresponds approximately to the bed height. Nevertheless, it appears that velocity is still impacted by the meshing, looking at the 3-cell case on Figure 59 (right). These light velocity springs are most probably due to the generation or deactivation of merged cells, and so to the re-initialization of the local pressure. For a water column of about 5.0 m at the inlet (i.e. $p_0 = 147130\ Pa$), the quench front goes as expected faster. The quenching time yielded by the 3-cell discretization is delayed of barely 2 s from the exact value, as shown on Figure 60 (left). The progression trend is also very well reproduced. The velocity springs, which were noticed on Figure 59 (right) are much smoother, and thus barely observable on Figure 60 (right). In general, the predicted quench front progression is very near to the exact progression, and gets even closer to it by increasing the discretization.

5.1.3 Quenching of hot debris bed and steam generation

This final test addresses the capability of COCOMO-3D in predicting the quench front progression in a hot debris bed; and thus, accounting for heat exchanges. The same bed as for the previous tests is taken as reference (same geometry, same porosity). In order to evaluate correctly heat transfers regarding the prediction of the quenching, water is supplied at a constant rate, because section 5.1.1 has already showed that the modelling of quenching by means of constant injection is very satisfactory. A mass rate of 5.0 kg/s was chosen, like in section 5.1.1. To determine the exact quench front velocity u_{QF}, one refers to equation (4-15). Nevertheless, this equation requires to know the upstream and downstream temperatures of gas and solid at the quench front, as well as the upstream temperature of water. The quenching of an overheated bed by subcooled water will yield an axial temperature profile under the quench front (lower part of the quenched zone is generally colder that the upper part). This will make the exact calculation of steam generation impossible, because one can't be sure of the exact temperature under the quench

front. Therefore, one has to rely on a configuration where temperatures can be easily guessed. For this reason, water is injected at saturation temperature (293.15 K). Water and particle temperatures within the quenched zone are also initialized at saturation. The quenched zone is supposed to be always purely liquid i.e. $s'_g = 0$.

Let's denote T^0, the temperature at the beginning of the quenching. Cooling of debris bed is performed for two different initial bed temperatures T_s^0: 700 K and 1500 K. The latter temperature lays in the range of very high temperatures that one may encounter in severe accidents. The unquenched zone is then initialized to 700 K or 1500 K, as well as the steam within this zone, $T_{s,up}^0 = T_{g,up}^0$. As mentioned in section 4.4.2, downstream gas temperature T_g'' is defined by relation (4-19):

$$\mathrm{T_g'' = (1-\phi)T_{sat} + \phi T_{g,up}}$$

where ϕ must be defined by the user. Thus, setting $\phi = 1$, it yields: $T_g'' = T_{g,up}$=$T_{s,up}$. As a matter of fact, no cooling of the dry zone by steam is possible, and so, downstream particles, steam and water should always stay at T_s^0 (i.e. 700 K or 1500 K).

With regard of these initial conditions and assumptions, equation (4-15) can be re-written as follows:

$$\mathrm{u_{QF} = \frac{\frac{\dot{m}_{inj}}{A_{bed}}\left(i_g(T_s^0) - i_{l,sat}\right)}{\varepsilon s'_l \rho'_l \left(i_g(T_s^0) - i_{l,sat}\right) + (1-\varepsilon)\rho_s c_{p,s}(T_s^0 - T_{sat})}} \qquad (5\text{-}6)$$

Gas specific enthalpy $i_g(T_s^0)$ must be checked in steam tables. All other values are known. Once u_{QF} is calculated, quenching time can be determined from relation (5-2). Exact results, analytically determined by (5-6), are reported on Figure 61 and Figure 62 (green curves) for initial solid temperature of 700 K and 1500 K respectively. In both cases, one observes that COCOMO-3D predicts the quench front progression very well. Quench front velocities match with analytical values during the first half of the quenching process. Nevertheless, near the end of the quenching (when reaching the top of the bed), COCOMO-3D predicts higher front velocities and deviates from the constant values obtained by (5-6). Indeed, one remarks near the end of the

quenching, that upstream gas saturation s_g' isn't equal to *0* anymore, i.e. that gas is present under the quench front, as shown on Figure 63. This contradicts with the initial assumption that the quenched zone is always purely liquid (i.e. s_g'=0), and consequently, the quench front velocity predicted by COCOMO-3D differs necessarily from the value obtained by (5-6). So, in spite of very similar velocities, these little deviations at the end of quenching yield light discrepancies regarding the quenching time (15-30 s). Quenching times are reported in Table 3.

To determine analytically the amount of steam generated during the quenching, assumptions must be made regarding the temperatures of the different phases at the end of the quenching. Assuming that the bed is at saturation temperature, the evacuated energy ΔH_s can be expressed as follows:

$$\Delta \mathrm{H_s} = \mathrm{m_s c_{p,s}}(\mathrm{T_s^0} - \mathrm{T_{sat}}) \tag{5-7}$$

Assuming also that water is at saturation temperature, too, at the end of the quenching, and that steam is overheated to T_s^0 (because T_g'' was set to $T_{g,up}$, and so to $T_{s,up}$) the energy balance can be written:

$$\Delta \mathrm{H_s} = \mathrm{m_{inj} c_{p,l}}\left(\mathrm{T_{sat}} - \mathrm{T_l^0}\right) + \mathrm{m_g}\left(\mathrm{i_{g,sat}} - \mathrm{i_{l,sat}}\right) + \mathrm{m_g c_{p,g}}(\mathrm{T_s^0} - \mathrm{T_{sat}}) \tag{5-8}$$

Since $T_l^0 = T_{sat}$, only the latent heat $(i_{g,sat} - i_{l,sat})$ and the steam overheating need to be considered. One obtains the generated mass of steam m_g:

$$\mathrm{m_g} = \frac{\mathrm{m_s c_{p,s}}(\mathrm{T_s^0} - \mathrm{T_{sat}})}{\mathrm{i_{g,sat}} - \mathrm{i_{l,sat}} + \mathrm{c_{p,g}}(\mathrm{T_s^0} - \mathrm{T_{sat}})} \tag{5-9}$$

Total masses of generated steam are reported in Table 3. COCOMO-3D prediction deviates only of 3% from exact values for $T_s^0 = 700\ K$, and 7% for $T_s^0 = 1500\ K$.

Table 3 : Quenching time and steam generation by flooding a hot debris bed with saturated water

Initial Bed temperature (K)	**Quenching time (s)**		**Steam generation (kg)**	
	Analytical	COCOMO-3D	Analytical	COCOMO-3D
700	250	220-237	537	521-526
1500	360	336-352	1042	1105-1113

Quench front progression and the associated steam generation are generally very satisfactory, for high (700 K) to very high (1500 K) temperatures, as well as for coarse and fine discretizations.

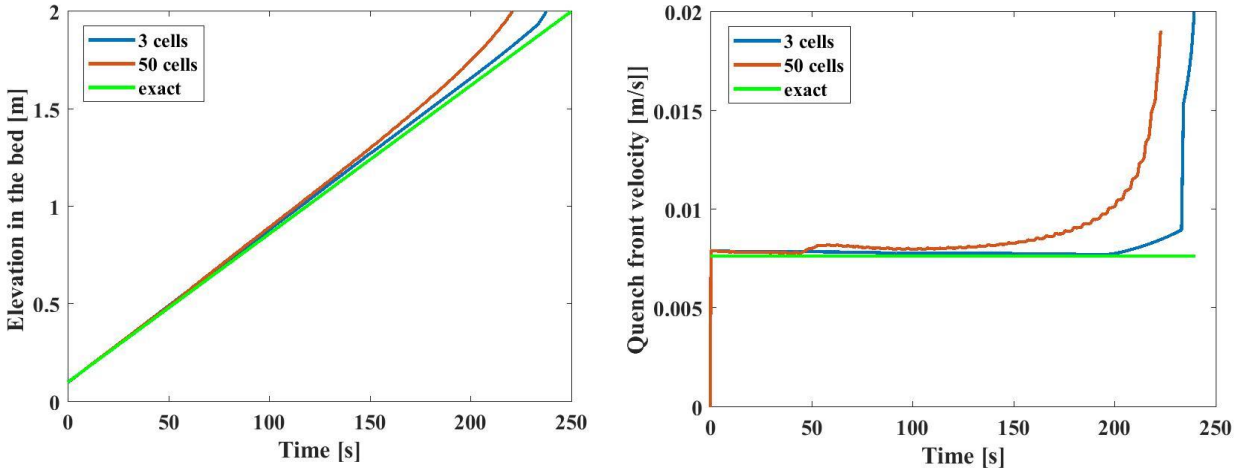

Figure 61 : Progression and velocity of the reconstructed Quench front (T_s^0= 700 K)

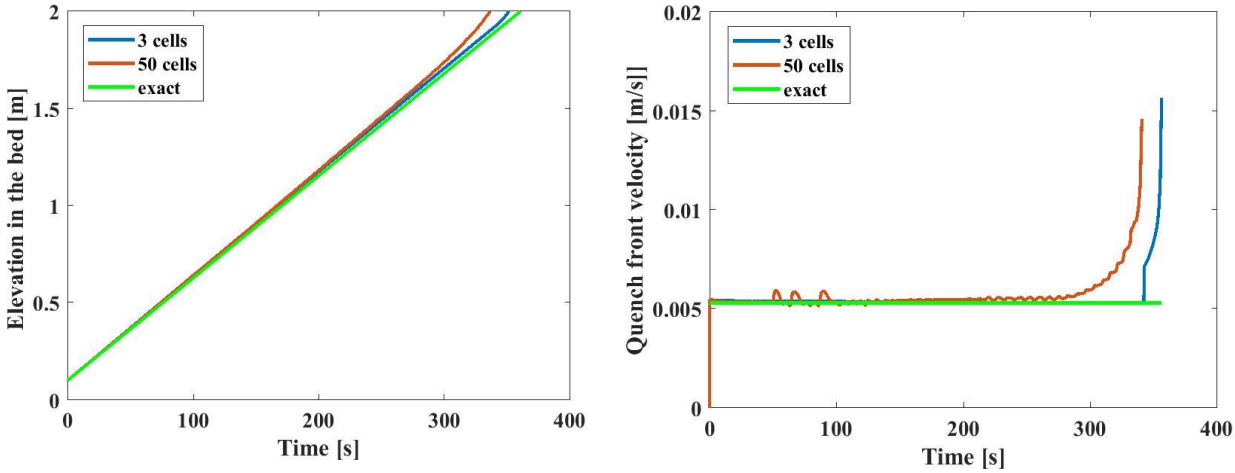

Figure 62 : Progression and velocity of the reconstructed Quench front (T_s^0= 1500 K)

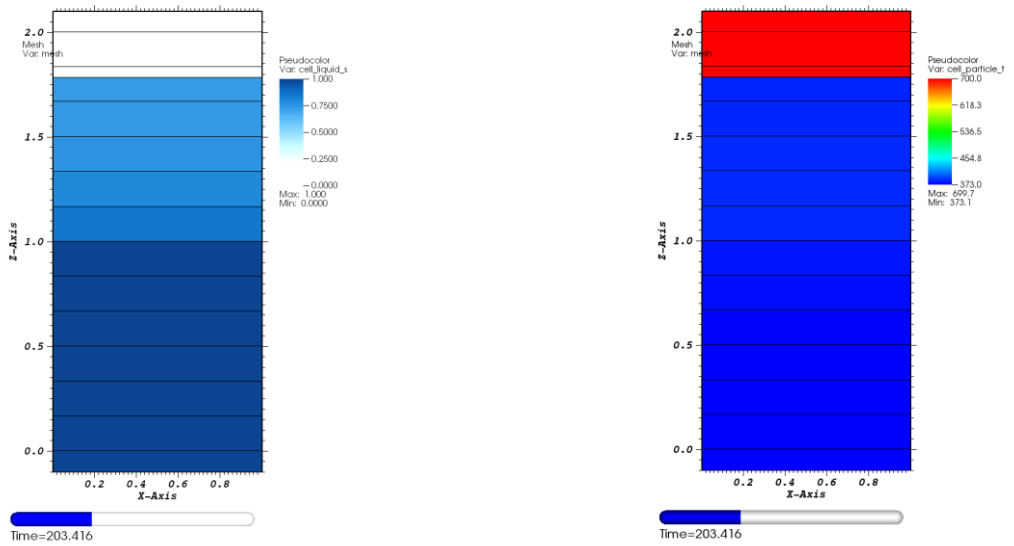

Figure 63 : Visualisation of 1D liquid fraction distribution (left) and temperature profile (right) at the end of the quenching of a 700 K debris bed

5.2 Reactor scale

Now that the new modelling has been verified against simple cases, it has to be finally confronted again to the reactor-scale case (presented earlier in section 3.4), which revealed the deficiency of COCOMO-3D when dealing with coarse meshing. Unlike the simple cases, the debris bed geometry is defined in the cylindrical coordinate system. Let's recall briefly its main characteristics: 2.0 m-high, radius of 1.54 m, porosity of 0.4, an effective particle diameter of 2.9 mm, and an initial particle temperature of 1400°C (i.e. 1673.15 K). 20°C-cold water is supplied at the bottom of the bed by gravity-driven injection; hydrostatic head at the inlet is approximately 6.0 m (i.e. 163000 Pa).

Quench front elevation was initialized at *z= 0.01 m*, i.e. 1 cm above the bottom of the bed. This might be low enough in order not to play any role on the final quenching time. Like before, simulations are performed one-dimensionally. Debris bed is discretized into 3 cells for the coarsest meshing, up to 60 cells for the finest meshing.

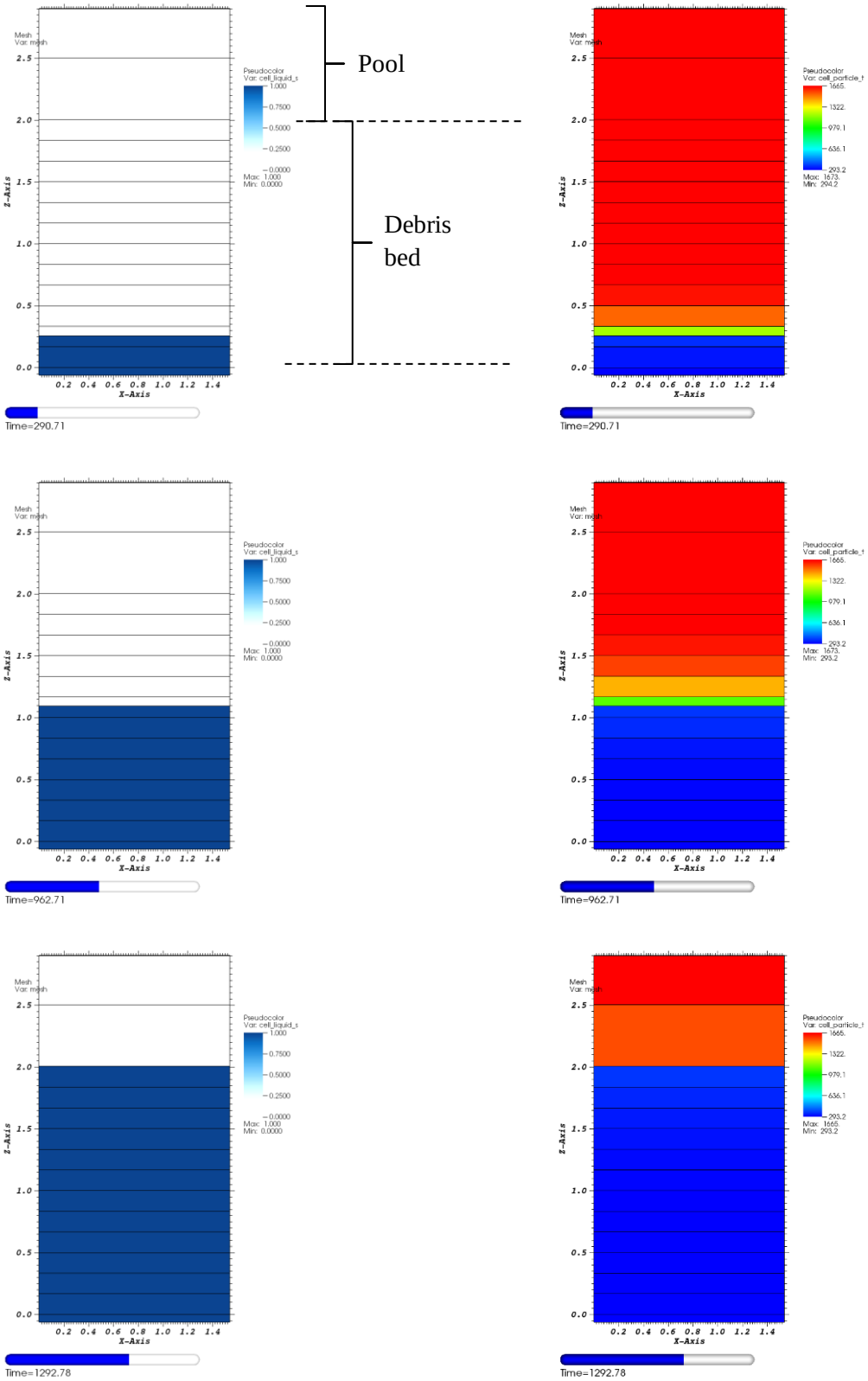

Figure 64 : Visualisation of 1D liquid fraction distribution (left) and temperature profile(right), during the quenching of a reactor-scale debris bed

Figure 64 shows post-visualisation at three time points for a bed discretized into 12 cells. One can follow the progression of the quench front, as well as the void fraction distribution. The quenching of the bed is highlighted by the evolution of the temperature profile (on the right side). Figure 65 (left) presents the quench front progression obtained for a 3-cell and 60-cell discretization (blue and red curves respectively) compared with the outcomes from the old standard COCOMO-3D version (green and violet curves), already presented on Figure 28. Deviation between quenching yielded by the coarsest and finest meshing is more acceptable with the new COCOMO-3D (60 s) that the one yielded by the old COCOMO-3D (150 s). Besides, quench front progressions obtained with the new modelling, whatever the discretization, seems to be very near to the value obtained with the finest discretization of the old COCOMO-3D, which should supposedly be the most reliable value. Moreover, regarding the steam generation during the quenching on Figure 65 (right), obtained by the new modelling with the coarsest meshing, the amount of steam (blue curve) happens to match almost perfectly the steam generation predicted by the old COCOMO-3D with 60 cells (violet curve), with a deviation of around 3%. As for the calculation with 60 cells, it presents a deviation of approximately 8% from the old COCOMO-3D results, which is also acceptable.

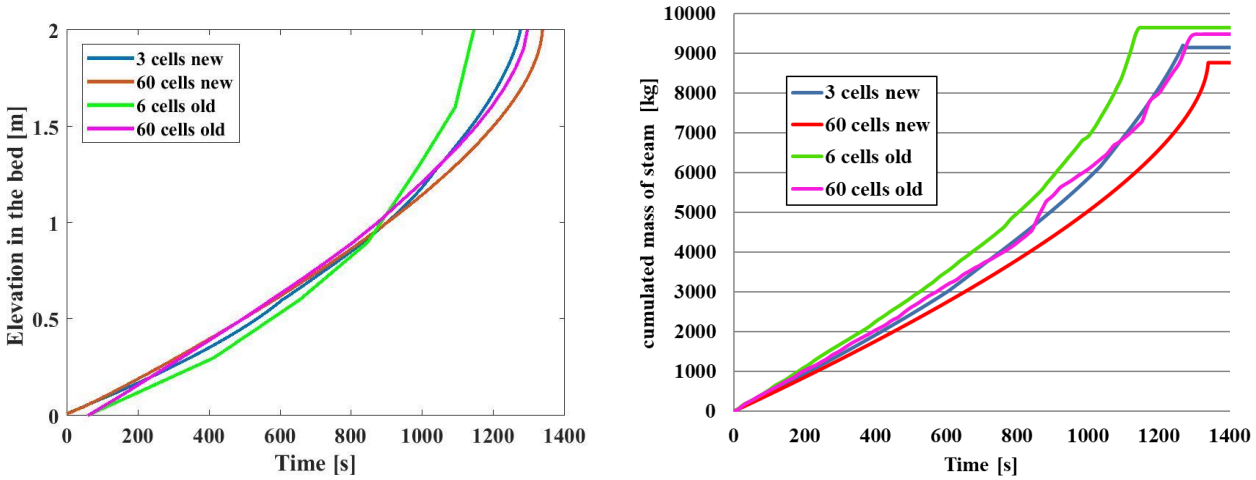

Figure 65 : Progression of the reconstructed Quench front and associated steam generation in reactor-scale debris bed (Hydrostatic Head = 6.0 m)

The second important aspect is the computing time. While several minutes (20 min -1h) were needed to computed this reactor-scale case with the old version of COCOMO-3D, the new

version of the code requires only some seconds, up to a few minutes (also for fine meshing). This is due to the fact that the new modelling prevents calculation from strong numerical instabilities. This is very well highlighted on Figure 66, presenting the behaviour of pressure at different elevations with the new (graph on the left) and the old COCOMO-3D (graph on the right), for a 12-cell meshing. On both graphs are indicated time points, when the quench front passes through the considered elevations (for example, *"QF at 0.1 m"* as the quench front has reached *z= 0.1 m*). One remarks that pressures from the old code version present strong oscillations, each peak corresponding to time point, as the quench front enters a new cell. This observation is in good agreement with the issue mentioned earlier in section 3.5. In spite of these strong oscillations, one may be able to recognize the same fundamental trends on the graph showing pressure evolution obtained with the new code version. The new modelling, i.e. the reconstruction of the quench front, seems to yield a definitely smoother, almost instability-free, pressure evolution; anyway, easier to work with. Nevertheless, some little plateaus are still noticeable, namely at *z= 0.5 m* and *1.0 m* (red and green curves), showing that the meshing still influences the results a little, though not significantly.

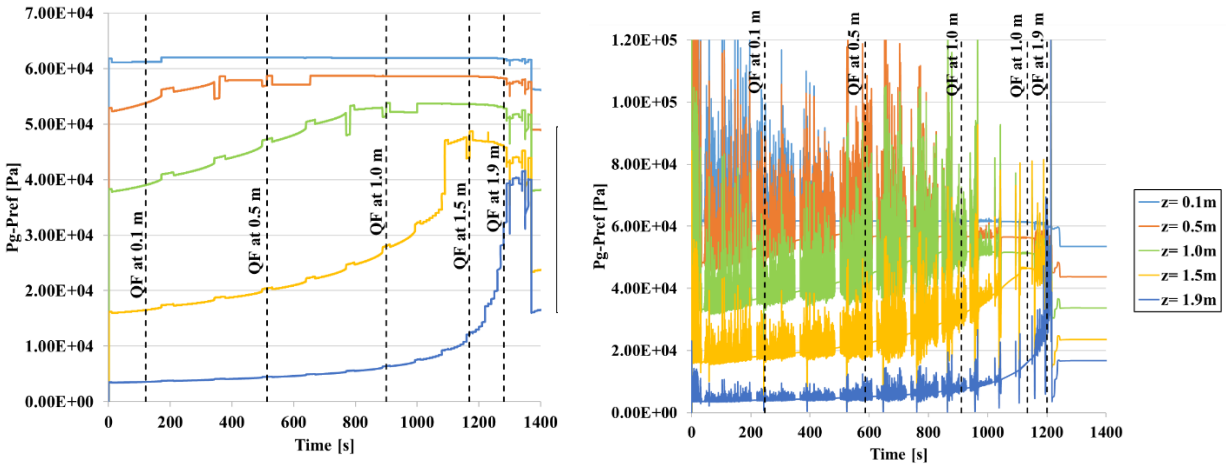

Figure 66 : Pressure evolution during the quenching at different elevations, with the new (left) and old (right) COCOMO-3D

Figure 67 satisfies the expectations, as it confirms that the amount of water that has to be injected in order to quench the debris bed completely is totally independent of the discretization. Injection of 15 ton of water was calculated in the 3-cell case as well as in the 60-cell case.

The sensitivity analysis performed for the old code version in section 3.4 is repeated here for the new code version. Figure 68 shows quench front progressions and steam generations for the different systems pressures (1 bar, 3 bar and 5 bar). Like for the old code version, it appears that it is with the pressure of 1 bar that the quench front got impacted the most by the meshing (violet and dark blue curves), though less significantly than with the old code version (refer to Figure 32, left). Besides, it is hard to notice any influence on the final steam generation. Contrarily to the old results (Figure 32, right), no impact of the meshing is observable; results obtained with 3 cells and 60 cells are very near to each other.

Quench front progressions and steam generations obtained for different porosities (30%, 40% and 45%) are presented on Figure 69. General trends, already observed on Figure 30 with the old COCOMO-3D, are also very well reproduced. Differences between results obtained with 3 cells and 60 cells are less important than in the past.

Finally, Figure 70 compares the quench front progression yielded by a hydrostatic head of 6.0 m with the one yielded by 3.0 m. As expected, the quench front progresses more slowly into the bed. Moreover, the deviation between the finest and the coarsest meshing, regarding the quenching time, remains negligible.

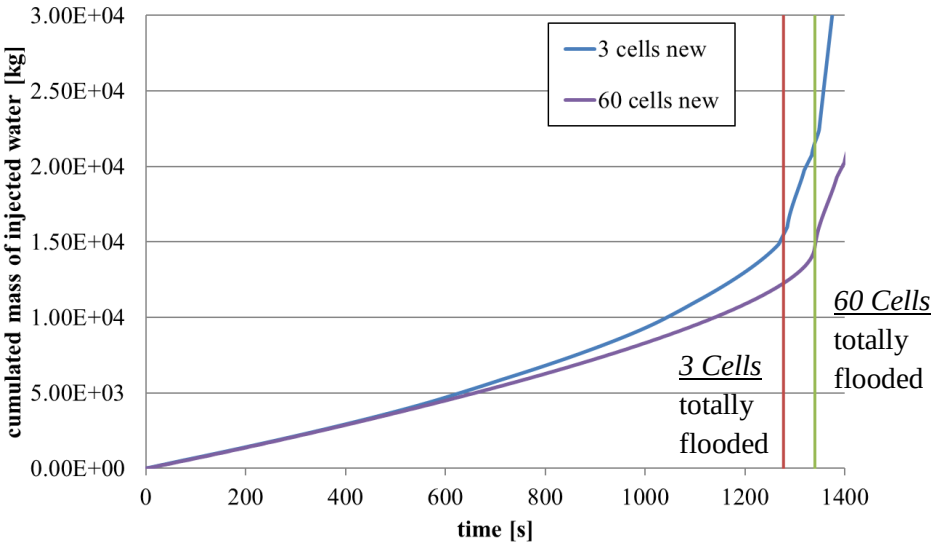

Figure 67 : Mass of water injected over the whole quenching in reactor-scale debris bed (Hydrostatic Head = 6.0 m)

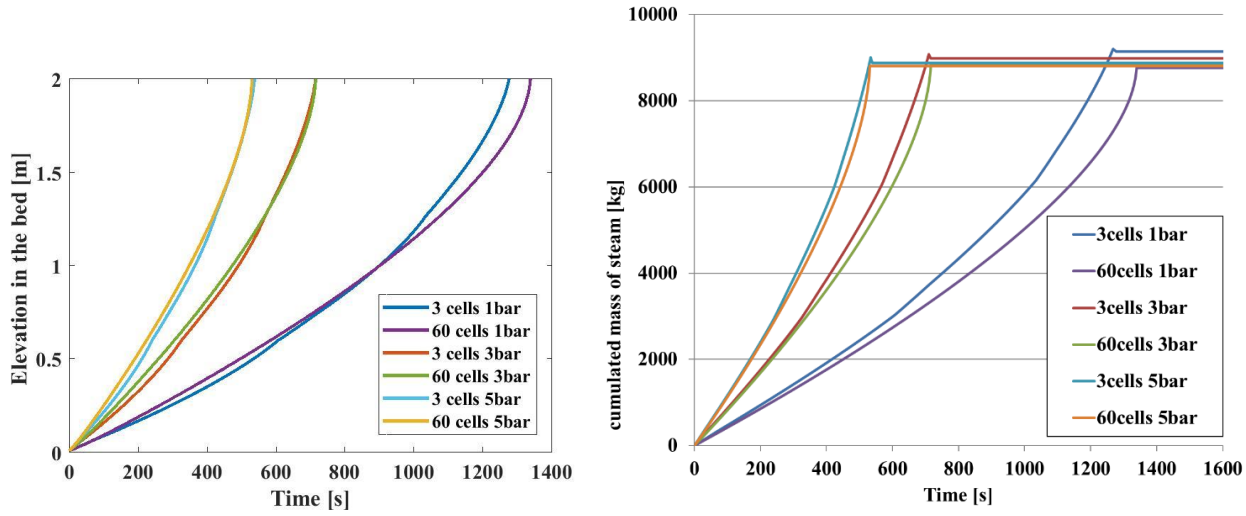

Figure 68 : (left) Quench front progression and (right) Generated mass of steam obtained with 3 and 60 cells for system pressures of 1 bar, 3 bar and 5 bar, with the new modelling

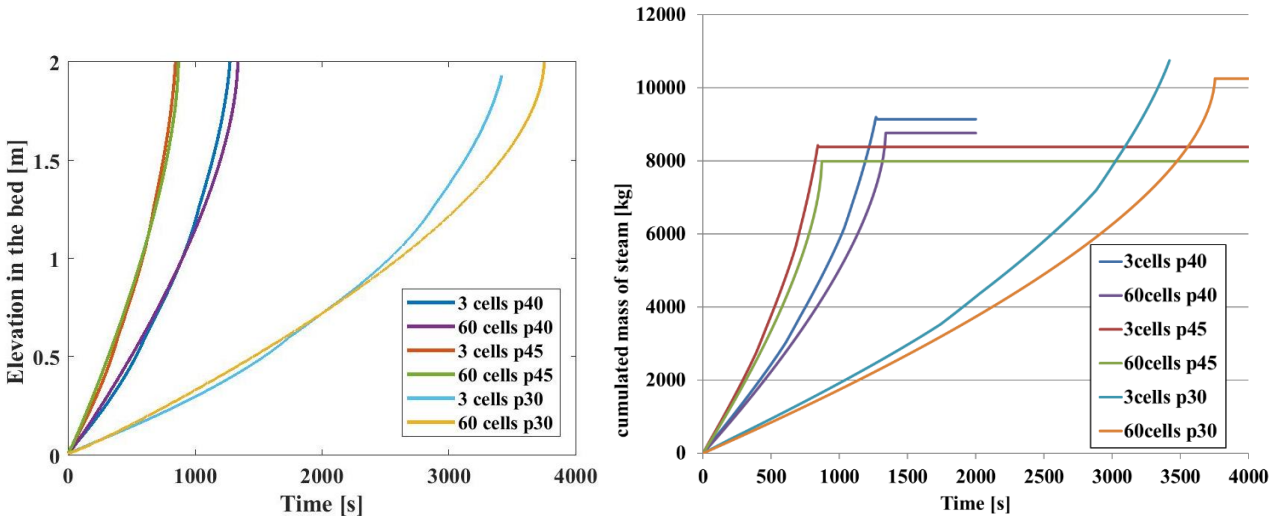

Figure 69 : (left) Quench front progression and (right) Generated mass of steam obtained with 3 and 60 cells for porosities of 30%, 40% and 45%, with the new modelling

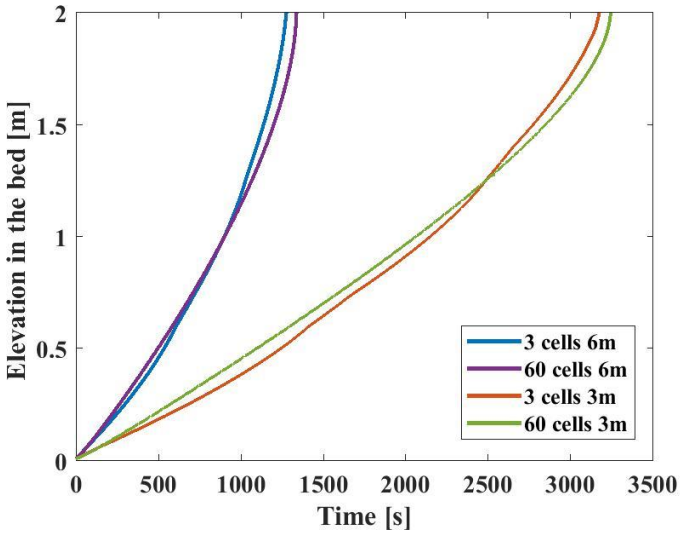

Figure 70 : Progression of the reconstructed Quench front in reactor-scale debris bed (Hydrostatic Head = 3.0 m)

6 Conclusion

Reflooding of severely degraded core is one of the major counter-measures with respect to the SAMGs. In order to predict the coolability of hot particles bed, severe accident codes must be able to deal with the thermohydraulic behaviour of two-phase flows in porous media. Integral system codes like ASTEC that are used as decision-making tool for emergency cases require a reasonably simplified modelling of the main phenomena, but also a coarsely discretized calculation domain. These requirements distinguish emergency codes from CFD-codes.

The actual modelling of COCOMO-3D for quenching, which is used as module in the integral code ATHLET-CD, already proved itself as very satisfactory when simulating down-scaled debris bed quenching or with a fine meshing but might not be fitting for emergency simulations. Indeed, when applying a 1D coarse meshing at a reactor-scale debris bed, simulations turned to be very unstable regarding pressures and water velocity, long-lasting and hence not reliable enough, as outcomes seem to be dependent upon the discretization.

The solution proposed in this work is a sounder treatment of the thermohydraulic at the boundaries of topology changes. It consists first in a reconstruction of the boundaries themselves, such as the particle bed geometry, and most of all the quench front. Reconstruction induces a redefinition of the computation grid (mesh) and generates necessarily irregular cells, which require an unstructured grid. When predefined by the user, trivial bed geometries are quite simple to reconstruct, since boundaries tracking and their steady representation are based on purely geometrical criteria. However, quench front reconstruction is far less trivial, because the quench front is a moving boundary depending on thermohydraulic criteria that are time-functions. An approach of type “isosurface” was chosen for the quench front reconstruction, based on the Cell Volume Fraction (*CVF*) instead of the material fraction more commonly used. This approach is certainly not perfect, the *CVF*s yielded by the reconstruction (being based on average *CVF* computed at nodes) deviates always a little from the *CVF*s obtained from the resolution of the equation system. Nevertheless, this approach presents also major advantages. First, the movement of the front is mostly governed by the quench front velocity, which is dependent on the predefined quench front temperature but also on the local mass, momentum and energy balances.

Secondly, this reconstruction method generates a discontinuity-free quench front in 2D or 3D simulations.

Mass, momentum and energy equations were locally adapted for moving boundaries, taking into account assumptions regarding fluid properties downstream and upstream of the quench front. Tracking and reconstruction of the quench front, as well as the new resolution of the conservation equations in the quench front region were successfully implemented and fitted to the general resolution algorithm of COCOMO-3D.

The modelling was then verified against 1D simple cases that can be also analytically resolved. 1D reactor-scale simulations with gravity-driven injection, which formerly highlighted COCOMO-3D difficulties in dealing with coarse meshing, were repeated with the new modelling. Predictions on the quenching time and steam generation are on the same range as those obtained with the standard COCOMO-3D, but are no longer dependent on the discretization. Results obtained with coarse (cell size > 60 cm) and fine (cell size < 5 cm) discretizations present only slight discrepancies. Moreover, progression of the quench front is far more stable, due the fact that the calculation of local pressure and velocities are also stable. Consequently, computing time is also significantly reduced.

To sum up, the new modelling enables fast and stable reactor-scale quenching simulations, moreover with gravity-driven injection, by using a coarse meshing and yielding apparently similar results as by using a fine meshing. So far, only 1D cases were tested, but the present model is also supposed to work in 2D and 3D cases. As this present work focuses on bottom-flooding, equations were sometimes simplified regarding this specific configuration where only upwards flow are considered. For the more complicated case of top-flooding, conservation equations should be further adapted.

Since each integral code presents own specificities, no genuine guidelines for the coupling of the model developed in this work with the different existing codes can be made. Nonetheless, implementation recommendations can be provided. First, it is essential that two-phase flow calculations are based on a 6-equation model, which clearly distinguishes the liquid from the gas phase and thus accounts explicitly for the interphase frictions. Secondly, integral codes must generate an unstructured grid, if not necessarily over the whole computational domain, at least on the reactor core region. This is unfortunately a sine qua non condition, the quench front

reconstruction and progression can only be properly modelled by means of a dynamic irregular and unstructured meshing. Thirdly, once embodied in an integral code and used together with other modules in the frame of accident calculations, the quench front initialization won't be based on boundary conditions on *CVF*, but based on *CVF* of neighbouring control volumes. This aspect must be carefully considered when integrating the quench front modelling into integral codes. As for computational restrictions of the modelling developed in this work one has already mentioned that it focuses mainly on bottom-flooding configurations. Realistic results for top-flooding calculation cannot be ensured without any further development. Same thing can be said concerning boiling of a submersed debris bed. In this case, it is probably inappropriate to reconstruct a quench front such as developed in this work, since one can even barely talk about a quench front in this case. In the future, further work could be also provided on the time-dependent reconstruction of the bed geometry, (since only fixed and trivial bed geometries were considered in the frame of this work), in order to deal with simultaneous debris bed formations and quenching.

7 References

[1] Électricité de France EDF, Le nucléaire en chiffres, 2019. https://www.edf.fr/groupe-edf/espaces-dedies/l-energie-de-a-a-z/tout-sur-l-energie/produire-de-l-electricite/le-nucleaire-en-chiffres.

[2] NEA Committee on the Safety of Nuclear Installations, Progress Made in the Last Fifteen Years through Analyses of the TMI-2 Accident Performed in Member Countries (2005).

[3] W. Weiss, Der Reaktorunfall von Tschernobyl, Nuklearmedizin 30 (1991) 226–232.

[4] Tokyo Electric Power Company Inc. (Ed.), The Development of and Lessons from the Fukushima Daiichi Nuclear Accident, Tokyo Electric Power Company, Inc., 2013.

[5] INSAG-10, Defence in Depth in Nuclear Safety, Vienna, Austria, 1996.

[6] Bal Raj Sehgal (Ed.), Nuclear Safety in Light Water Reactors, Elsevier, 2012.

[7] Pohlner. G, A. Trometer, M. Buck, F. Schäfer, Tusheva. P, T. Hollands, V. Di Marcello, U. Imke, V. Sanchez, X. Cheng, F. Kretschmar, P. Dietrich, R. Gehr, Störfallmaßnahmen zur Milderung der Folgen von Reaktorunfällen mit schweren Kernschäden. technical report IKE 2-163, 2014.

[8] D. Jacquemain (Ed.), Les accidents de fusion du coeur des réacteurs nucléaires de puissance: État des connaissances, EDP sciences, Les Ulis, 2013.

[9] I. Shepherd, T. Haste, N. Kourti, F. Oriolo, M. Leonardi, J. Knorr, S. Kretschmer, M. Umbreit, B. Adroguer, P. Hofmann, A. Miassoedov, V. Noack, M. Steinbrück, C. Homann, H. Plitz, M. Veshchunov, M. Jaeger, M. Medale, B. Turland, R. Hiles, G. Bandini, S. Ederli, T. Linnemann, M. Koch, H. Unger, K. Müller, J.F. Benítez, Investigation of core degradation (COBE), Nuclear Engineering and Design 209 (2001) 107–116.

[10] E.W. Coryell, Summary of Important Results and SCDAP/RELAP5 Analyses for OECD LOFT. Experiment LP-FP2,: NUREG/CR-6160, NEA-CSNI-R(1994)3, 1994.

[11] P. Hofmann, M. Markiewicz, Chemical behavior of (Ag,In,Cd) absorber rods in severe LWR accidents: KfK-4670 CNEANT-16/89, 1990.

[12] P. Hofmann, Reaktions- und Schmelzverhalten der LWR-Corekomponenten UO_2, Zirkaloy und Stahl waehrend der Abschmelzperiode: KFK-2220, 1976.

[13] G. Schanz, S. Hagen, P. Hofmann, G. Schumacher, L. Sepold, Information on the evolution of severe LWR fuel element damage obtained in the CORA program, Journal of Nuclear Materials 188 (1992) 131–145.

[14] D. Magallon, Characteristics of corium debris bed generated in large-scale fuel-coolant interaction experiments, Nuclear Engineering and Design 236 (2006) 1998–2009.

[15] J.M. Seiler, B. Tourniaire, A phenomenological analysis of melt progression in the lower head of a pressurized water reactor, Nuclear Engineering and Design (2014) 87–95.

[16] T.G. Theofanous, C. Liu, S. Additon, S. Angelini, O. Kymäläinen, T. Salmassi, In-vessel coolability and retention of a core melt, Nuclear Engineering and Design 169 (1997) 1–48.

[17] B.W. Spencer, K. Wang, C.A. Blomquist, L.M. McUmber, J.P. Schneider, Fragmentation and quench behavior of corium melt streams in water: NUREG/CR-6133, ANL-93/3, 1994.

[18] M. Fischer, O. Herbst, H. Schmidt, Demonstration of the heat removing capabilities of the EPR core catcher, Nuclear Engineering and Design 235 (2005) 1189–1200.
[19] H. Alsmeyer, M. Farmer, F. Ferderer, B. Spencer, W. Tromm (Eds.), The COMET-concept for cooling of ex-vessel corium melts: ICONE-6 Proc.of the 6th Internat.Conf.on Nuclear Engineering, San Diego, Calif., May 10-15, 1998 New York, N.Y. ASME, 1998, CD-ROM, 1998.
[20] M. Ishii, G. de Jarlais, Flow regime transition and interfacial characteristics of inverted annular flow, Nuclear Engineering and Design 95 (1986) 171–184.
[21] M. Ishii, G. de Jarlais, Flow visualization study of inverted annular flow of post dryout heat transfer region, Nuclear Engineering and Design 99 (1987) 187–199.
[22] N.T. Obot, M. Ishii, Two-phase flow regime transition criteria in post-dryout region based on flow visualization experiments, International Journal of Heat and Mass Transfer 31 (1988) 2559–2570.
[23] W. Hering, C. Homann, Degraded core reflood: present understanding based on experimental and analytical database and its impact on LWRs, Nuclear Engineering and Design 237 (2007) 2315–2321.
[24] A. Kaiser, W. Schütz, H. Will, PREMIX Experiments PM12 – PM18 to Investigate the Mixing of a Hot Melt with Water. Report FZKA 6380, Karlsruhe, Germany, 2001.
[25] M. Rashid, R. Kulenovic, E. Laurien, Experimental results on the coolability of a debris bed with down comer configurations, Nuclear Engineering and Design 249 (2012) 104–110.
[26] A. Karbojian, W.M. Ma, P. Kudinov, T.N. Dinh, A scoping study of debris bed formation in the DEFOR test facility, Nuclear Engineering and Design 239 (2009) 1653–1659.
[27] G. Hofmann, On the Location and Mechanisms of Dryout in Top-Fed and Bottom-Fed Particulate Beds, Nuclear Technology 65 (1984) 36–45.
[28] G. Hofmann, Dryout in very deep particulate beds, Nuclear Engineering and Design 99 (1987) 177–185.
[29] K. Atkhen, G. Berthoud, SILFIDE experiment: Coolability in a volumetrically heated debris bed, Nuclear Engineering and Design 236 (2006) 2126–2134.
[30] M. Rashid, R. Kulenovic, E. Laurien, A.K. Nayak, Experimental results on the coolability of a debris bed with multidimensional cooling effects, Nuclear Engineering and Design 241 (2011) 4537–4543.
[31] S. Thakre, L. Li, W. Ma, An experimental study on coolability of a particulate bed with radial stratification or triangular shape, Nuclear Engineering and Design 276 (2014) 54–63.
[32] I. Lindholm, S. Holmström, J. Miettinen, V. Lestinen, J. Hyvärinen, P. Pankakoski, H. Sjövall, Dryout heat flux experiments with deep heterogeneous particle bed, Nuclear Engineering and Design 236 (2006) 2060–2074.
[33] P.P. Kulkarni, M. Rashid, R. Kulenovic, A.K. Nayak, Experimental investigation of coolability behaviour of irregularly shaped particulate debris bed, Nuclear Engineering and Design 240 (2010) 3067–3077.
[34] P. Schäfer, M. Groll, R. Kulenovic, Basic investigations on debris cooling, Nuclear Engineering and Design 236 (2006) 2104–2116.

[35] P. Schäfer, G. Lohnert, Boiling experiments for the validation of dryout models used in reactor safety, Nuclear Engineering and Design 236 (2006) 1511–1519.
[36] S. Leininger, R. Kulenovic, E. Laurien, Experiments on the dryout behavior of stratified debris beds, in: 46th Annual Meeting on Nuclear Technology (AMNT 2015), Berlin, Germany, 5-7th May 2015.
[37] S. Leininger, R. Kulenovic, E. Laurien, Experiments on the dryout behavior of stratified debris beds, atw - Int. Journal for Nuclear Power (2015) 602–606.
[38] S. Leininger, R. Kulenovic, E. Laurien, Experimental Investigations on the Coolability of Debris Beds under Variation of Inflow Conditions, in: Proceedings of 16th International Topical Meeting on Nuclear Reactor Thermalhydraulics (NURETH 16), Hyatt Regency Chicago, USA, 2016.
[39] E. Takasuo, S. Holmström, T. Kinnunen, P.H. Pankakoski, The COOLOCE experiments investigating the dryout power in debris beds of heap-like and cylindrical geometries, Nuclear Engineering and Design 250 (2012) 687–700.
[40] E. Takasuo, An experimental study of the coolability of debris beds with geometry variations, Annals of Nuclear Energy 92 (2016) 251–261.
[41] N.K. Tutu, T. Ginsberg, J. Klein, J. Klages, C.E. Schwarz, Debris bed quenching under bottom flood conditions, 3850th ed., 1984.
[42] G. Repetto, T. Garcin, S. Eymery, F. Fichot, Experimental program on debris reflooding (PEARL) – Results on PRELUDE facility, Nuclear Engineering and Design 264 (2013) 176–186.
[43] G. Repetto, N. Chikhi, F. Fichot, Main outcomes on debris bed cooling from PRELUDE experiments, in: 6th European Review Meeting on Severe Accident Research (ERMSAR-2013), Avignon, France, 2-4th October, 2013.
[44] N. Chikhi, T. Garcin, F. Foubert, P. March, F. Fichot, First experimental results of large scale debris bed reflood tests in the PEARL facility, in: Proceedings of 16th International Topical Meeting on Nuclear Reactor Thermalhydraulics (NURETH 16), Hyatt Regency Chicago, USA, 2016.
[45] M. Rashid, S. Rahman, R. Kulenovic, M. Bürger, E. Laurien, Quenching Experiments: Coolability of Debris Bed, Nuclear Technology 181 (2013) 208–215.
[46] S. Leininger, T. Knobelspies, R. Kulenovic, E. Laurien, First experimental results on reflooding of debris beds at elevated pressure, in: Proceedings of 11th International Topical Meeting on Nuclear Thermal Hydraulics, Operation and Safety (NUTHOS-11), Gyeongju, South Korea, 2016.
[47] V.X. Tung, V.K. Dhir, Quenching of debris beds having variable permeability in the axial and radial directions, Nuclear Engineering and Design 99 (1987) 275–284.
[48] T. Ginsberg, J. Klein, C.E. Schwarz, J. Klages, J.C. Chen, Transient core debris bed heat removal experiments and analysis, United States, 1983.
[49] D.H. Cho, D.R. Armstrong, L. Bova, S.H. Chan, G.R. Thomas, Debris bed quenching studies (NUREG/CP--0027-Vol2). United States, 1983.

[50] D.R. Armstrong, L. Bova, D.H. Cho, Formation of dry pockets during water penetration into a hot particle bed, Transactions of the American Nuclear Society (1982) 418–419.
[51] S. Leininger, Experimentelle Untersuchungen der Kühlbarkeit prototypischer Schüttungskonfigurationen unter dem Aspekt der Reaktorsicherheit: Dissertation, IKE 8-126, Universität Stuttgart.
[52] P. Chatelard, S. Belon, L. Bosland, L. Carénini, O. Coindreau, F. Cousin, C. Marchetto, H. Nowack, L. Piar, L. Chailan, Main modelling features of the ASTEC V2.1 major version, Annals of Nuclear Energy 93 (2016) 83–93.
[53] H. Nowack, P. Chatelard, L. Chailan, St. Hermsmeyer, V. Sanchez, L. Herranz, CESAM – Code for European severe accident management, EURATOM project on ASTEC improvement, Annals of Nuclear Energy 116 (2018) 128–136.
[54] I. Gómez García-Toraño, Further development of Severe Accident Management Strategies for a German PWR Konvoi Plant based on the European Severe Accident Code ASTEC: Dissertation, KIT Karlsruhe, Karlsruhe.
[55] N. Reinke, H.W. Chan, M. Sonnenkalb, Comparative analysis of a LOCA for a German PWR with ASTEC and ATHLET-CD, in: 44th Annual Meeting on Nuclear Technology (AMNT 2013), Berlin, Germany, 14-16th May 2013.
[56] A.J. Trometer, Investigations on the flooding behaviour of a partially degraded reactor core: Dissertation, IKE 2-157, Universität Stuttgart.
[57] Tusheva. P, F. Schäfer, Y. Kozmenkov, S. Kliem, T. Hollands, A. Trometer, M. Buck, WASA-BOSS: ATHLET-CD model for severe accident analysis for generic KONVOI reactor, atw - Int. Journal for Nuclear Power vol.60, issue 7 (2015).
[58] A. Berkhan, M. Buck, Pohlner. G, S. Rahman, Modeling and Validation Basis of the MEWA code: Technical report IKE 2-160, 2013.
[59] Pohlner. G, M. Buck, S. Rahman, Modeling and Validation Basis of the JEMI code: Technical report IKE 2-161, 2013.
[60] A. Hartmann, M. Buck, J. Starflinger, Three-Dimensional Analysis on the Coolability of Inhomogeneous Debris Bed with the Code MEWA 3D, in: Proceedings of 2016 International Congress on Advances in Nuclear Power Plants (ICAPP 2016), San Francisco, CA, USA, 2016.
[61] W. Hilali, M. Buck, J. Starflinger, Modeling of Debris Bed Formation by Particles Deposition and Relocation during Severe Accidents in Light Water Reactors, in: Proceedings of 11th International Topical Meeting on Nuclear Thermal Hydraulics, Operation and Safety (NUTHOS-11), Gyeongju, South Korea, 2016.
[62] W. Hilali, M. Buck, J. Starflinger, Influence of Steam Production on Particulate Debris Bed Spreading, in: Proceedings of International Congress on Advances in Nuclear Power Plants (ICAPP 2018), Charlotte, North Carolina, United States, 2018.
[63] C. D'Alessandro, M. Buck, J. Starflinger, Assessment and Improvement of Models on Reflooding of a Severely Degraded Core to be used in Current Severe Accident System Codes, in: Proceedings of 11th International Topical Meeting on Nuclear Thermal Hydraulics, Operation and Safety (NUTHOS-11), Gyeongju, South Korea, 2016.

[64] S. Ergun, Fluid Flow through Packed Columns, Journal of Chemical Engineering Progress (1952) 89–94.
[65] M.K. Das, P.P. Mukherjee, K. Muralidhar, Modeling Transport Phenomena in Porous Media with Applications, Springer International Publishing, Cham, 2018.
[66] M. Buck, Pohlner. G, S. Rahman, Documentation of the MEWA code: Technical report (not released yet), 2012.
[67] R.J. Lipinski, Model for boiling and dryout in particle beds: NUREG/CR--2646, United States, 1982.
[68] A.W. Reed, The effect of channeling on the dryout of heated particulate beds immersed in a liquid pool: PhD Thesis, Massachusetts Institute of Technology, 1982.
[69] K. Hu, T.G. Theofanous, On the measurement and mechanism of dryout in volumetrically heated coarse particle beds, International Journal of Multiphase Flow 17 (1991) 519–532.
[70] T. Schulenberg, U. Mueller, A refined model for the coolability of core debris with flow entry from the bottom: Report KfK--3880/2, Karlsruhe, Germany, 1984.
[71] V.X. Tung, V.K. Dhir, A hydrodynamic model for two-phase flow through porous media, International Journal of Multiphase Flow 14 (1988) 47–65.
[72] W. Schmidt, Influence of multidimensionality and interfacial friction on the coolability of fragmented corium: Dissertation IKE 2-149, Universität Stuttgart, 2013.
[73] S. Rahman, Coolability of corium debris under severe accident conditions in light water reactors: Dissertation IKE 2-155, Universität Stuttgart, 2013.
[74] W.M. Rohsenow, a method of correlating heat transfer data for surface boiling of liquids: Technical Report No. 5, Massachusetts Institute of Technology, United States, 1951.
[75] J.H. Lienhard, A heat transfer textbook, 2nd ed., Prentice-Hall, Englewood Cliffs, N.J, 1987.
[76] S.V. Patankar, Numerical heat transfer and fluid flow, Taylor & Francis, Bristol, PA, 1980.
[77] M. Buck, Modelling of the Late Phase of Core Degradation in Light Water Reactors. Dissertation, IKE 2-153, Universität Stuttgart, 2007.
[78] A. Bachrata, F. Fichot, G. Repetto, M. Quintard, J. Fleurot, Quench front progression in a superheated porous medium: experimental analysis and model development, Journal of Energy and Power Engineering (2013) 514–523.
[79] M. Rashid, Coolability of volumetrically heated particle beds: Dissertation, IKE 8-124, Universität Stuttgart.
[80] C. D'Alessandro, M. Buck, J. Starflinger, Assessment of the Integral Code ASTEC Regarding the Coolability of a Debris Bed, in: 46th Annual Meeting on Nuclear Technology (AMNT 2015), Berlin, Germany, 5-7th May 2015.
[81] N. Chikhi, F. Fichot, Experimental and theoretical study of large scale debris bed reflood in the PEARL facility, Nuclear Engineering and Design 312 (2017) 48–58.
[82] N. Chikhi, F. Fichot, A. Swaidan, Effect of water entrainment on the coolability of a debris bed surrounded by a by-pass: Integral reflood experiments and modelling, Annals of Nuclear Energy 110 (2017) 418–437.

[83] F. Duval, Modélisation du renoyage d'un lit de particules contribution à l'estimation des propriétés de transport macroscopiques. Ph.D. thesis, Institut National Polytechnique de Toulouse, 2002.
[84] A. Bachrata, Modélisation du renoyage d'un cœur du réacteur nucléaire fortement dégradé: Ph.D. thesis, Institut National Polytechnique de Toulouse, 2012.
[85] P. Sapin, Etude expérimentale de l'ébullition en masse dans un milieu poreux modèle: Ph.D. thesis, Institut National Polytechnique de Toulouse. 2014.
[86] F.H. Harlow, A.A. Amsden, J.R. Nix, Relativistic fluid dynamics calculations with the particle-in-cell technique, Journal of Computational Physics 20 (1976) 119–129.
[87] A.A. Amsden, Particle-in-cell method for the calculation of the dynamics of compressible fluids: LA-3466, Los Alamos Scientific Lab., University of California, 1966.
[88] S. Osher, J.A. Sethian, Fronts propagating with curvature-dependent speed: Algorithms based on Hamilton-Jacobi formulations, Journal of Computational Physics 79 (1988) 12–49.
[89] W.F. Noh, P. Woodward, SLIC (Simple Line Interface Calculation), in: A. Vooren, P. Zandbergen (Eds.), Proceedings of the Fifth International Conference on Numerical Methods in Fluid Dynamics June 28 - July 2, 1976 Twente University, Enschede, Springer, Berlin [u.a.], 1976, pp. 330–340.
[90] C.W. Hirt, B.D. Nichols, Volume of fluid (VOF) method for the dynamics of free boundaries, Journal of Computational Physics 39 (1981) 201–225.
[91] D. Youngs, Time-Dependent Multi-material Flow with Large Fluid Distortion, Num. Method Fluid Dyn. 24 (1982).
[92] D. Youngs, An interface tracking method for a 3D Eulerian hydrodynamics code: Report AWRE-44/92/35, Atomic Weapon Research Establishment, UK, 1984.
[93] W.J. Rider, D.B. Kothe, Reconstructing Volume Tracking, Journal of Computational Physics 141 (1998) 112–152.
[94] F.L. Addessio, J. Baumgardner, J.K. Dukowicz, N.L. Johnson, B. Kashiwa, R.M. Rauenzahn, C. Zemach, CAVEAT: A computer code for fluid dynamics problems with large distortion and internal slip. Revision 1: Technical Report LA-10613-MS, Los Alamos National Laboratory, 1986.
[95] J.S. Meredith, Material Interface Reconstruction in VisIt, in: Proceedings from the Nuclear Explosives Code Development Conference, Livermore, California, Unites States, 2004.
[96] J.S. Meredith, H. Childs, Visualization and Analysis-Oriented Reconstruction of Material Interfaces, Computer Graphics Forum 29 (2010) 1241–1250.
[97] W.E. Lorensen, H.E. Cline, Marching cubes: A high resolution 3D surface construction algorithm, in: Proceedings of the 14th annual conference on Computer graphics and interactive techniques, ACM, New York, NY, 1987, pp. 163–169.
[98] J.G. Trulio, K.R. Trigger, Numerical solution of the one-dimensional hydrodynamic equations in an arbitrary time-dependent coordinate system: Report UCRL-6522, 1961.
[99] I. Demirdžić, M. Perić, Space conservation law in finite volume calculations of fluid flow, Int. J. Numer. Meth. Fluids 8 (1988) 1037–1050.

[100] I. Demirdžić, M. Perić, Finite volume method for prediction of fluid flow in arbitrarily shaped domains with moving boundaries, Int. J. Numer. Meth. Fluids 10 (1990) 771–790.

[101] R. Clavier, N. Chikhi, F. Fichot, M. Quintard, Experimental investigation on single-phase pressure losses in nuclear debris beds: Identification of flow regimes and effective diameter, Nuclear Engineering and Design 292 (2015) 222–236.

8 Appendices

Appendix-A : Calculation of effective particle diameter

The methods presented below were already mentioned in the work of Clavier et al. [101]. Given a polydispersed particle bed, composed of n_i spherical particles of diameter D_i, with *i* the index of the group of particles ($i = 1..\ n_{group}$) characterized by their same diameter. A unique particle size, so-called effective diameter, can be defined by different averaging approach:

Number-weighted diameter:

$$D^{eff} = \frac{\sum_i D_i n_i}{\sum_i n_i}$$

Length-weighted diameter:

$$D^{eff} = \frac{\sum_i D_i^2 n_i}{\sum_i D_i n_i}$$

Surface-weighted diameter:

$$D^{eff} = \frac{\sum_i D_i^3 n_i}{\sum_i D_i^2 n_i}$$

Volume-weighted diameter:

$$D^{eff} = \frac{\sum_i D_i^4 n_i}{\sum_i D_i^3 n_i}$$

A little beyond the scope of this work, in case the particles are non-spherical, one refers to equivalent diameters. Different approaches are mentioned in [101].

Appendix-B : Absolute velocities

a) On a structured grid

Absolute velocities $\left|\overrightarrow{w_g}\right|$ and $|\overrightarrow{w_l}|$for gas and liquid, at face $\left(i+\frac{1}{2},j\right)$

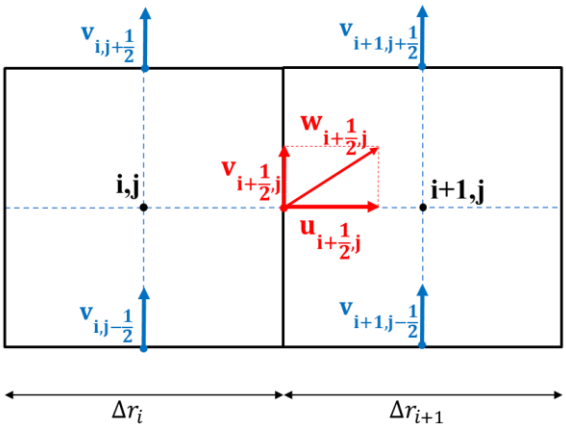

Figure 71 : velocities on orthogonal structured grid (radial)

$$\langle\left|\overrightarrow{\mathrm{w_g}}\right|\rangle_{\mathrm{i+\frac{1}{2},j}}=\sqrt{\mathrm{u^2_{g,i+\frac{1}{2},j}}+\langle\mathrm{v_g}\rangle^2_{\mathrm{i+\frac{1}{2},j}}}$$

$$\langle|\overrightarrow{\mathrm{w_l}}|\rangle_{\mathrm{i+\frac{1}{2},j}}=\sqrt{\mathrm{u^2_{l,i+\frac{1}{2},j}}+\langle\mathrm{v_l}\rangle^2_{\mathrm{i+\frac{1}{2},j}}}$$

$$\langle\left|\overrightarrow{\mathrm{w_g}}-\overrightarrow{\mathrm{w_l}}\right|\rangle_{\mathrm{i+\frac{1}{2},j}}=\sqrt{\left(\mathrm{u_{g,i+\frac{1}{2},j}}-\mathrm{u_{l,i+\frac{1}{2},j}}\right)^2+\left(\langle\mathrm{v_g}\rangle_{\mathrm{i+\frac{1}{2},j}}-\langle\mathrm{v_l}\rangle_{\mathrm{i+\frac{1}{2},j}}\right)^2}$$

where the transverse velocities $\langle v_g\rangle$ and $\langle v_l\rangle$ (tangent to the face) are obtained by interpolation:

$$\langle\mathrm{v}\rangle_{\mathrm{i+\frac{1}{2},j}}=\frac{1}{2}\,\frac{\left(\mathrm{v_{i,j-\frac{1}{2}}}+\mathrm{v_{i,j-\frac{1}{2}}}\right)\cdot\Delta\mathrm{r_{i+1}}+\left(\mathrm{v_{i+1,j-\frac{1}{2}}}+\mathrm{v_{i+1,j-\frac{1}{2}}}\right)\cdot\Delta\mathrm{r_i}}{\Delta\mathrm{r_{i+1}}+\Delta\mathrm{r_i}}$$

By neglecting the transverse terms, one can also use the simplified form of $\left|\overrightarrow{w_g}\right|$ and $|\overrightarrow{w_l}|$:

$$\langle|\overrightarrow{w_g}|\rangle_{i+\frac{1}{2},j} = \left|u_{g,i+\frac{1}{2},j}\right|$$

$$\langle|\overrightarrow{w_l}|\rangle_{i+\frac{1}{2},j} = \left|u_{l,i+\frac{1}{2},j}\right|$$

Absolute velocities $|\overrightarrow{w_g}|$ and $|\overrightarrow{w_l}|$ for gas and liquid, at face $\left(i, j+\frac{1}{2}\right)$ are computed similarly.

$$\langle|\overrightarrow{w_g}|\rangle_{i+\frac{1}{2},j} = \sqrt{\langle u_g\rangle^2_{i,j+\frac{1}{2}} + v^2_{g,i,j+\frac{1}{2}}}$$

$$\langle|\overrightarrow{w_l}|\rangle_{i+\frac{1}{2},j} = \sqrt{\langle u_l\rangle^2_{i,j+\frac{1}{2}} + v^2_{l,i,j+\frac{1}{2}}}$$

In that case, $\langle u_g\rangle$ and $\langle u_l\rangle$ are the transverse velocities, and must be interpolated.

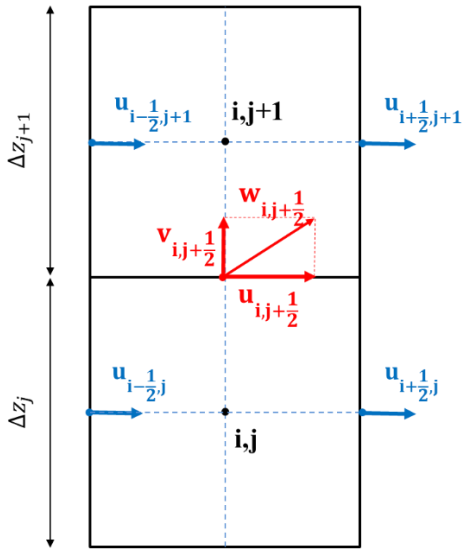

Figure 72 : velocities on orthogonal structured grid (axial)

b) On a unstructured grid

Absolute velocities $|\overrightarrow{w_g}|$ and $|\overrightarrow{w_l}|$ for gas and liquid, at face *j*

$$\langle|\overrightarrow{w_g}|\rangle_j = \sqrt{u^2_{g,j} + \langle ut_g\rangle^2_j}$$

$$\langle|\overrightarrow{w_l}|\rangle_j = \sqrt{u_{l,j}^2 + \langle ut_l\rangle_j^2}$$

where the transverse velocities $\langle ut_g \rangle$ and $\langle ut_l \rangle$ (tangent to the face) are obtained by interpolation as follows:

$$\langle ut\rangle_j = \sqrt{\overrightarrow{uf_j} \cdot \overrightarrow{uf_j} - \overrightarrow{uf_j} \cdot \overrightarrow{n_j}}$$

with uf_j at face j obtained by interpolating the velocities of cell centre $\overrightarrow{uc}_{cell1}$ and $\overrightarrow{uc}_{cell2}$:

$$\overrightarrow{uf_j} = \overrightarrow{uc}_{cell1} \cdot \frac{dr1}{dr} + \overrightarrow{uc}_{cell2} \cdot \frac{dr2}{dr}$$

And

$$\overrightarrow{uc}_{celli} = \frac{\sum_k^{nFace} u_k \cdot \vec{n}_k}{\sum_k^{nFace} |\vec{n}_k|} \text{ ; with } nFace\text{: number of faces of cell } i$$

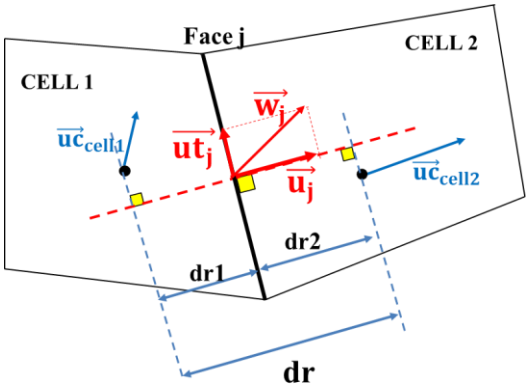

Figure 73 : velocities on unstructured grid

Like for the structured grid, the form of $|\overrightarrow{w_g}|$ and $|\overrightarrow{w_l}|$ can be simplified by neglecting the transverse terms:

$$\langle|\overrightarrow{w_g}|\rangle_j = |u_{g,j}|$$

$$\langle|\overrightarrow{w_l}|\rangle_j = |u_{l,j}|$$

Appendix-C : Interpolation methods

Indices and lengths that are referred to in this section can be found on Figure 71 to Figure 73 (previous section).

a) Linear interpolation

Structured grid

The interpolation of the quantity *X* face at $\left(i+\frac{1}{2},j\right)$

$$\langle \mathrm{X} \rangle_{\mathrm{i}+\frac{1}{2},\mathrm{j}} = \mathrm{w_L X_{i,j}} + \mathrm{w_R X_{i+1,j}}$$

With w_L and w_R the weights of the left and right-side quantities, such as:

$$\mathrm{w_L} = \frac{\Delta \mathrm{r_{i+1}}}{\Delta \mathrm{r_i} + \Delta \mathrm{r_{i+1}}} \quad , \qquad \mathrm{w_R} = \frac{\Delta \mathrm{r_i}}{\Delta \mathrm{r_i} + \Delta \mathrm{r_{i+1}}}$$

The interpolation for z-staggered faces $\left(i,j+\frac{1}{2}\right)$ follows analogously.

Unstructured grid

The interpolation of the quantity *X* at face *j*

$$\langle \mathrm{X} \rangle_{\mathrm{j}} = \mathrm{w_1 X_{cell1}} + \mathrm{w_2 X_{cell2}}$$

With w_1 and w_2 the weights of quantities at each side of the face *j*, such as:

$$\mathrm{w_1} = \frac{\mathrm{dr2}}{\mathrm{dr}} \quad , \qquad \mathrm{w_2} = \frac{\mathrm{dr1}}{\mathrm{dr}}$$

b) Up-wind interpolation

Structured grid

The interpolation of the quantity *X* at face $\left(i+\frac{1}{2},j\right)$

$$\langle \mathrm{X} \rangle_{\mathrm{i}+\frac{1}{2},\mathrm{j}} = \mathrm{w_L X_{i,j}} + \mathrm{w_R X_{i+1,j}}$$

With w_L and w_R the weights of the left and right-side quantities, such as:

$$\mathrm{w_L} = \begin{cases} 1 \ \text{if} \ \mathrm{u}_{\mathrm{i}+\frac{1}{2},\mathrm{j}} \geq 0 \\ 0 \ \text{if} \ \mathrm{u}_{\mathrm{i}+\frac{1}{2},\mathrm{j}} < 0 \end{cases}, \mathrm{w_R} = \begin{cases} 0 \ \text{if} \ \mathrm{u}_{\mathrm{i}+\frac{1}{2},\mathrm{j}} \geq 0 \\ 1 \ \text{if} \ \mathrm{u}_{\mathrm{i}+\frac{1}{2},\mathrm{j}} < 0 \end{cases}$$

The interpolation for z-staggered faces $\left(i,j+\frac{1}{2}\right)$ follows analogously.

Unstructured grid

The interpolation of the quantity *X* at face *j*

$$\langle \mathrm{X} \rangle_{\mathrm{j}} = \mathrm{w_1 X_{cell1}} + \mathrm{w_2 X_{cell2}}$$

With w_1 and w_2 the weights of quantities at each side of the face *j*, such as:

$$\mathrm{w_1} = \begin{cases} 1 \ \text{if} \ \mathrm{u_j} \geq 0 \\ 0 \ \text{if} \ \mathrm{u_j} < 0 \end{cases}, \mathrm{w_2} = \begin{cases} 0 \ \text{if} \ \mathrm{u_j} \geq 0 \\ 1 \ \text{if} \ \mathrm{u_j} < 0 \end{cases}$$

c) Geometrical interpolation

Structured grid

The interpolation of the quantity *X* at face $\left(i+\frac{1}{2},j\right)$

$$\frac{1}{\langle X\rangle_{i+\frac{1}{2},j}} = \frac{w_L}{X_{i,j}} + \frac{w_R}{X_{i+1,j}}$$

With w_L and w_R the weights of the left and right-side quantities, defined for linear interpolation in a).

The interpolation for axial faces $\left(i, j+\frac{1}{2}\right)$ follows analogously.

Unstructured grid

The interpolation of the quantity *X* at face *j*

$$\frac{1}{\langle X\rangle_j} = \frac{w_1}{X_{cell1}} + \frac{w_2}{X_{cell2}}$$

With w_1 and w_2 the weights of quantities at each side of the face *j*, defined for linear interpolation in a).

Appendix-D : Area and volume approximations

a) Area

In case of faces constituted by three vertices, area as well as face normal $\vec{n}$ can be exactly determined. Face centroid position is obtained by averaging the coordinates of the vertices.

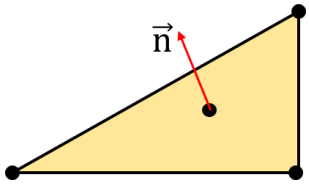

If a face is constituted of more than three vertices, the vertices may possibly not belong to the same plane. As approximation approach, the surface is first split into triangles. To do that, position of the mid-point (red point on the figure below) must be determined first, by averaging the positions of the vertices.

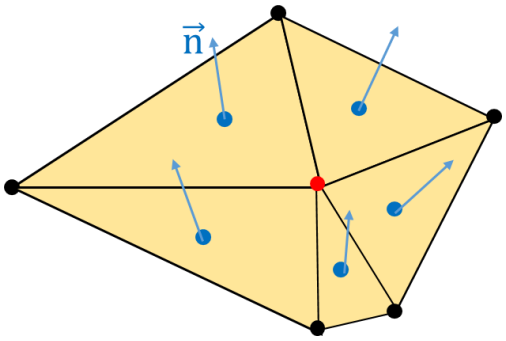

After the triangulation, area A and normal vector $\vec{n}$ of all the triangles are determined as well as the centroid positions $\vec{c}$ of all the triangles. Then, centroid, area and normal vector of the whole surface are approximated as shown below, with *nTriangle* the number of triangles:

$$\vec{c} = \frac{\sum_k^{nTriangle} \vec{c}_k A_k}{\sum_k^{nTriangle} A_k}$$

$$\vec{n} = \frac{\sum_k^{nTriangle} \vec{n}_k A_k}{\left|\sum_k^{nTriangle} \vec{n}_k A_k\right|}$$

$$A = \sum_{k}^{nTriangle} A_k$$

b) Volume

The computation of volume follows the same principle. If the volume is constituted of four faces (i.e. tetrahedron, by four vertices), the volumes can be exactly determined.

If more than four faces form the volume, the volume must be split into tetrahedrons.

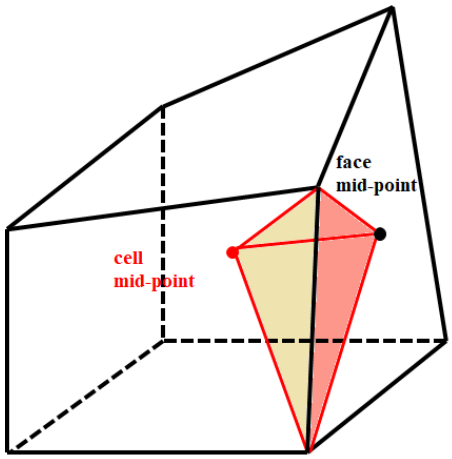

First, the mid-point of the cell is determined by averaging the vertices coordinates. Secondly, it is checked if the faces are triangles or not (if they possess three vertices or more). If yes, the volume of tetrahedron formed by the triangle as basis and the cell mid-point can be directly calculated. If not, the mid-point of the face is determined, and the face must be split into triangles (like presented above for the area calculation). Tetrahedrons are formed with these triangles as basis and the cell mid-point, like depicted on the figure right above. The whole cell volume is defined as the sum of all the tetrahedral sub-volumes.

$$V = \sum_{k}^{nTetrahedron} V_k$$

The cell centroid position is calculated as follows:

$$\vec{c} = \frac{\sum_{k}^{nTetrahedron} \vec{c}_k V_k}{\sum_{k}^{nTetrahedron} V_k}, \text{with } \vec{c}_k \text{ centroid of Tetrahedron } k$$

Appendix-E : Conduction and convection

a) Structured grid

The conductive fluxes of liquid, gas and solid at the face $\left(i+\frac{1}{2},j\right)$ is obtained by central difference of the temperatures and geometrical interpolation of the conductivities:

$$\dot{q}^{cond}_{i+\frac{1}{2},j} = -C^{cond}_{i+\frac{1}{2},j}\left(T_{i+1} - T_{i,j}\right) \tag{8-1}$$

With $C^{cond}_{i+\frac{1}{2},j} = A_{i+\frac{1}{2},j}\frac{2k^{eff}_{i,j}k^{eff}_{i+1,j}\Delta r_i \Delta r_{i+1}}{k^{eff}_{i,j}\Delta r_{i+1} + k^{eff}_{i+1,j}\Delta r_i}$ (8-2)

The interpolation for z-staggered faces $\left(i,j+\frac{1}{2}\right)$ follows analogously.

The convective fluxes of liquid and gas at the face $\left(i+\frac{1}{2},j\right)$ is obtained by up-wind interpolation:

$$\dot{q}^{conv}_{i+\frac{1}{2},j} = \begin{cases} \dot{m}_{i+\frac{1}{2},j} i_{i,j} & \text{if } \dot{m}_{i+\frac{1}{2},j} \geq 0 \\ \dot{m}_{i+\frac{1}{2},j} i_{i+1,j} & \text{if } \dot{m}_{i+\frac{1}{2},j} < 0 \end{cases} \tag{8-3}$$

The interpolation for z-staggered faces $\left(i,j+\frac{1}{2}\right)$ follows analogously.

b) Unstructured grid

The conductive fluxes of liquid, gas and solid at the face *j* is obtained by central difference of the temperatures and geometrical interpolation of the conductivities:

$$\dot{q}^{cond}_{j} = -C^{cond}_{j}\left(T_{cell2} - T_{cell1}\right) \tag{8-4}$$

With $C_j^{cond} = A_j \frac{2k_{cell1}^{eff} k_{cell2}^{eff}}{k_{cell1}^{eff} dr2 + k_{cell2}^{eff} dr1}$ (8-5)

And

$$k_{cell1}^{eff} = k_{x,cell1}^{eff} \cdot n_{xj}^2 + k_{y,cell1}^{eff} \cdot n_{yj}^2 + k_{z,cell1}^{eff} \cdot n_{zj}^2$$

$$k_{cell2}^{eff} = k_{x,cell2}^{eff} \cdot n_{xj}^2 + k_{y,cell2}^{eff} \cdot n_{yj}^2 + k_{z,cell2}^{eff} \cdot n_{zj}^2$$

$k_x^{eff}, k_y^{eff}\ k_z^{eff}$ being the *x*-,*y*- and *z*-components of k^{eff}, and n_{xj}, n_{yj} and n_{zj} the *x*-,*y*- and *z*-components of the normal vector of the face *j*.

The convective fluxes of liquid and gas at the face *j* is obtained by up-wind interpolation:

$$\dot{q}_j^{conv} = \begin{cases} \dot{m}_j i_{cell1} & \text{if } \dot{m}_j \geq 0 \\ \dot{m}_j i_{cell2} & \text{if } \dot{m}_j < 0 \end{cases} \quad (8\text{-}6)$$

c) Hybrid differencing

More realistic results can be reached by calculating additionally a so-called hybrid difference, with respect to the Peclet number, such as:

$$Pe_{i+\frac{1}{2},j} = \begin{cases} \dfrac{\left|\dot{m}_{i+\frac{1}{2},j}\left(i_{i+1,j} - i_{i,j}\right)\right|}{\left|\dot{q}_{i+\frac{1}{2},j}^{cond}\right|} & \text{if } T_{i+1,j} \neq T_{i,j} \\ \dfrac{\left|\dot{m}_{i+\frac{1}{2},j} c_{p,i,j}\right|}{C_{i+\frac{1}{2},j}^{cond}} & \text{if } T_{i+1,j} = T_{i,j} \end{cases} \quad (8\text{-}7)$$

at the face $\left(i + \frac{1}{2}, j\right)$.

If $Pe_{i+\frac{1}{2},j} > 2$, conduction can be neglected, and so:

$$\dot{q}_{i+\frac{1}{2},j} = \dot{q}_{i+\frac{1}{2},j}^{conv}$$

With $\dot{q}^{conv}_{i+\frac{1}{2},j}$ from (8-3).

If $Pe_{i+\frac{1}{2},j} \leq 2$:

$$\dot{q}_{i+\frac{1}{2},j} = \dot{q}^{cond}_{i+\frac{1}{2},j} + \dot{m}_{i+\frac{1}{2},j}\left(\frac{i_{i,j} + i_{i,j}}{2}\right)$$

with $\dot{q}^{cond}_{i+\frac{1}{2},j}$, $C^{cond}_{i+\frac{1}{2},j}$ and $\dot{q}^{conv}_{i+\frac{1}{2},j}$ from (8-1), (8-2) and (8-3) respectively.

Hybrid differencing for z-staggered faces $\left(i, j+\frac{1}{2}\right)$ and unstructured faces *j* follows analogously.

Appendix-F : Particles to fluid heat transfer

Heat flux between the solid porous medium and gas $Q_{s,g}$ or water $Q_{s,l}$ can be both expressed as follows:

$$\mathrm{Q_{s,k}} = \mathrm{a_{s,k}} \mathrm{h_{s,k}} (\mathrm{T_s} - \mathrm{T_k}) \text{ , with k=l,g} \tag{8-8}$$

With the interfacial area density:

$$\mathrm{a_{s,k}} = \mathrm{F(s_k)} \cdot \frac{6 \cdot (1 - \varepsilon)}{\mathrm{D_p}}$$

And $F(s_k)$, correction factor defined as follows:

$$\mathrm{F(s_k)} = \begin{cases} 0\,, & \text{if } \mathrm{s_k} < 0.7 \\ \dfrac{\mathrm{s_k} - 0.7}{0.3}\,, & \text{if } \mathrm{s_k} \geq 0.7 \end{cases}$$

The heat transfer coefficient $h_{s,k}$ is obtained by calculating the Nusselt number $Nu_{s,k}$:

$$\mathrm{h_{s,k}} = \frac{\mathrm{Nu_{s,k}}\, \lambda_\mathrm{k}}{\mathrm{D_P}}$$

With $\mathrm{Nu_{s,k}} = 2 + 0.6\sqrt{\mathrm{Re_k}}$

And the Reynolds number defined as: $\mathrm{Re_k} = \frac{\|\vec{w}_\mathrm{k} \rho_\mathrm{k} \mathrm{D_P}\|}{\eta_\mathrm{k}}$

Appendix-G : Simulation of DEBRIS quench tests (results for an initial temperature of 500°C)

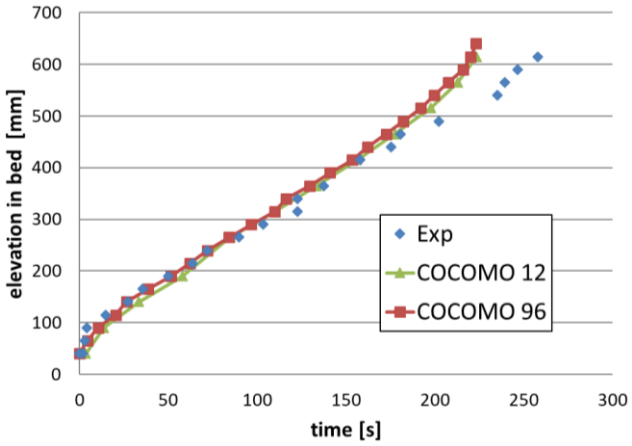

Figure 74 : Axial quench front progression in DEBRIS (gravity-driven injection)

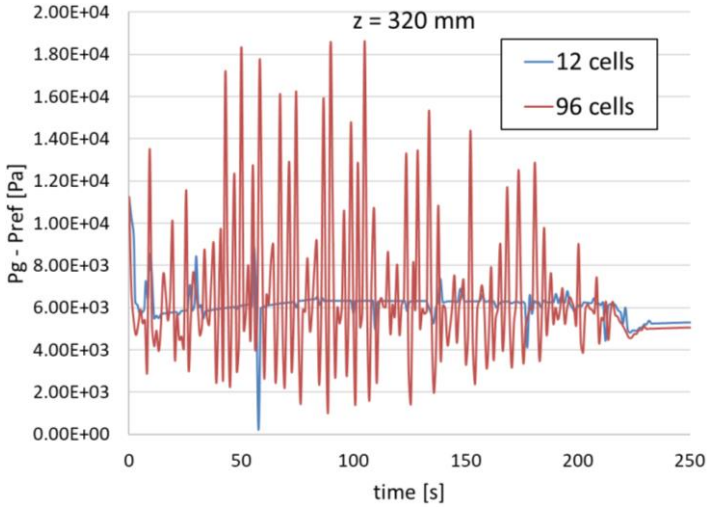

Figure 75 : Gas pressure in debris bed at elevation 320 mm (gravity-driven injection)

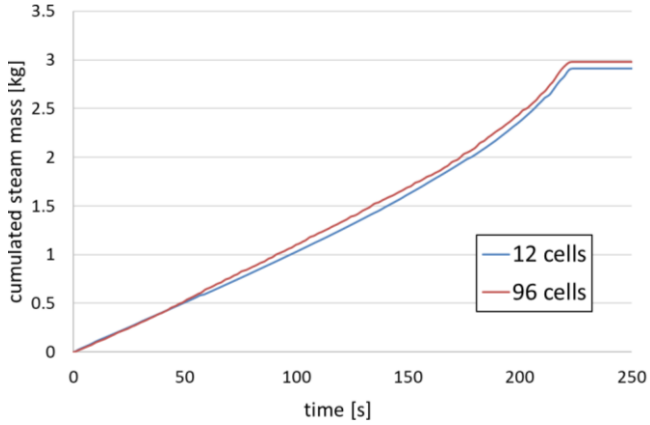

Figure 76 : Mass of steam generated over the whole quenching (gravity-driven injection)

Appendix-H: Value averaging at grid nodes of an unstructured meshing

This section shows approaches to estimate a mean value of a parameter Ψ at a grid node, from the values of Ψ in the cells (values of Ψ at cell centroid) sharing the node.

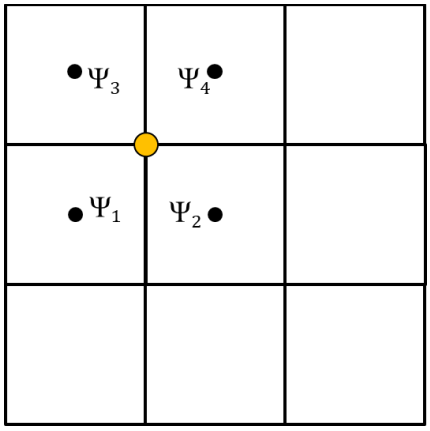

Figure 77 : Averaging of the variable Ψ at a node (yellow point) on a uniform orthogonal grid

For a regular orthogonal meshing, such like the 2D example depicted on Figure 77, the mean value of Ψ at the grid node in yellow is easy to calculate. A basic averaging of the four neighbouring values Ψ_1, Ψ_2, Ψ_3 and Ψ_4 (respectively, in 3D eight neighbouring values) suffices:

$$\Psi_{\text{node}} = \frac{\sum_{\text{k}}^{4} \Psi_{\text{k}}}{4}$$

However, for an unstructured meshing, such like the 2D example depicted on Figure 78, the mean value of Ψ at the grid node in yellow should be estimated by weighted averaging. The smaller is a cell, the nearer is its centroid from the concerned node, the nearer will also be its value of Ψ to the node.

Considering *n* cells sharing the concerned node, an interesting averaging approach would be to weight each value Ψ_k of centroid *k*, with the inverse of its absolute distance to the node, i.e. $\frac{1}{\|\vec{x}_k\|}$:

$$\Psi_{node} = \frac{\sum_k^n \Psi_k \frac{1}{\|\vec{x}_k\|}}{\sum_k^n \frac{1}{\|\vec{x}_k\|}}$$

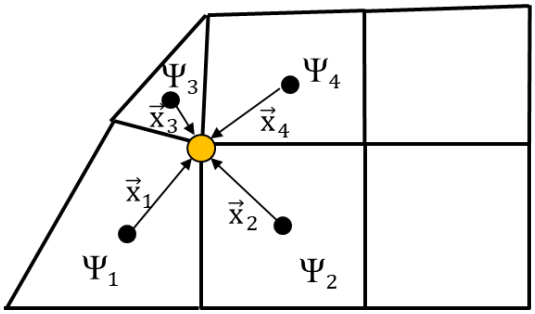

Figure 78 : Averaging of the variable Ψ at a node (yellow point) on an irregular grid

Appendix-I : Linearization of velocities with respect to saturations and pressure gradients

As seen in section 4.4.3, the velocities are obtained from an iterative solution procedure by finding the values of u'_g and u'_l for which the residuals of the momentum equations, $Resi_g^{mo}$ and $Resi_l^{mo}$, vanish. The velocities are only implicitly given as functions of pressure gradient and liquid saturation, thus the partial derivatives of the velocities with respect to pressure and liquid saturation cannot be calculated directly. However, one can calculate the partial derivatives of the residuals of the momentum equations, $Resi_g^{mo}$ and $Resi_l^{mo}$, with respect to velocities, pressure gradient and saturation, either analytically or by finite differences. For a better legibility, $Resi_g^{mo}$ and $Resi_l^{mo}$ are henceforth denoted R_g and R_l respectively.

First, R_g and R_l must be formally seen as functions of ∇p , s'_l, u'_g and u'_l. The velocities u'_g and u'_l are themselves functions of ∇p and s'_l, i.e.:

$$\mathrm{R_g} = \mathrm{R_g}(\nabla \mathrm{p}, \mathrm{s'_l}, \mathrm{u'_g}(\nabla \mathrm{p}, \mathrm{s'_l}), \mathrm{u'_l}(\nabla \mathrm{p}, \mathrm{s'_l})) \tag{8-9}$$

$$\mathrm{R_l} = \mathrm{R_l}(\nabla \mathrm{p}, \mathrm{s'_l}, \mathrm{u'_g}(\nabla \mathrm{p}, \mathrm{s'_l}), \mathrm{u'_l}(\nabla \mathrm{p}, \mathrm{s'_l})) \tag{8-10}$$

Applying the chain rule, the total differentials of R_g and R_l can be expressed as

$$\begin{aligned} \mathrm{dR_g} = \frac{\partial \mathrm{R_g}}{\partial \mathrm{u'_g}}\left(\frac{\partial \mathrm{u'_g}}{\partial \mathrm{s'_l}}\mathrm{ds'_l} + \frac{\partial \mathrm{u'_g}}{\partial \nabla \mathrm{p}}\mathrm{d}\nabla \mathrm{p}\right) + \frac{\partial \mathrm{R_g}}{\partial \mathrm{u'_l}}\left(\frac{\partial \mathrm{u'_l}}{\partial \mathrm{s'_l}}\mathrm{ds'_l} + \frac{\partial \mathrm{u'_l}}{\partial \nabla \mathrm{p}}\mathrm{d}\nabla \mathrm{p}\right) \\ + \frac{\partial \mathrm{R_g}}{\partial \mathrm{s'_l}}\mathrm{ds'_l} + \frac{\partial \mathrm{R_g}}{\partial \nabla \mathrm{p}}\mathrm{d}\nabla \mathrm{p} = 0 \end{aligned} \tag{8-11}$$

and

$$\begin{aligned} \mathrm{dR_l} = \frac{\partial \mathrm{R_l}}{\partial \mathrm{u'_g}}\left(\frac{\partial \mathrm{u'_g}}{\partial \mathrm{s'_l}}\mathrm{ds'_l} + \frac{\partial \mathrm{u'_g}}{\partial \nabla \mathrm{p}}\mathrm{d}\nabla \mathrm{p}\right) + \frac{\partial \mathrm{R_l}}{\partial \mathrm{u'_l}}\left(\frac{\partial \mathrm{u'_l}}{\partial \mathrm{s'_l}}\mathrm{ds'_l} + \frac{\partial \mathrm{u'_l}}{\partial \nabla \mathrm{p}}\mathrm{d}\nabla \mathrm{p}\right) \\ + \frac{\partial \mathrm{R_l}}{\partial \mathrm{s'_l}}\mathrm{ds'_l} + \frac{\partial \mathrm{R_l}}{\partial \nabla \mathrm{p}}\mathrm{d}\nabla \mathrm{p} = 0 \end{aligned} \tag{8-12}$$

Besides, it is worth mentioning that, because of $R_g = 0$ and $R_l = 0$, also the total derivatives have to satisfy $dR_g = 0$ and $dR_l = 0$.

Now, setting for instance ∇p to 0 in equation (8-11), one can determine the partial derivative of R_g with respect to saturation:

$$\mathrm{dR_g} = \frac{\partial \mathrm{R_g}}{\partial \mathrm{u'_g}} \frac{\partial \mathrm{u'_g}}{\partial \mathrm{s'_l}} \mathrm{ds'_l} + \frac{\partial \mathrm{R_g}}{\partial \mathrm{u'_l}} \frac{\partial \mathrm{u'_l}}{\partial \mathrm{s'_l}} \mathrm{ds'_l} + \frac{\partial \mathrm{R_g}}{\partial \mathrm{s'_l}} \mathrm{ds'_l} = 0 \tag{8-13}$$

Thus:

$$\left.\frac{\mathrm{dR_g}}{\mathrm{ds'_l}}\right|_{\mathrm{d\nabla p=0}} = \frac{\partial \mathrm{R_g}}{\partial \mathrm{u'_g}} \frac{\partial \mathrm{u'_g}}{\partial \mathrm{s'_l}} + \frac{\partial \mathrm{R_g}}{\partial \mathrm{u'_l}} \frac{\partial \mathrm{u'_l}}{\partial \mathrm{s'_l}} + \frac{\partial \mathrm{R_g}}{\partial \mathrm{s'_l}} = 0 \tag{8-14}$$

Similarly, one obtains

$$\left.\frac{\mathrm{dR_l}}{\mathrm{ds'_l}}\right|_{\mathrm{d\nabla p=0}} = \frac{\partial \mathrm{R_l}}{\partial \mathrm{u'_g}} \frac{\partial \mathrm{u'_g}}{\partial \mathrm{s'_l}} + \frac{\partial \mathrm{R_l}}{\partial \mathrm{u'_l}} \frac{\partial \mathrm{u'_l}}{\partial \mathrm{s'_l}} + \frac{\partial \mathrm{R_l}}{\partial \mathrm{s'_l}} = 0 \tag{8-15}$$

$$\left.\frac{\mathrm{dR_g}}{\mathrm{d\nabla p}}\right|_{\mathrm{ds'_l=0}} = \frac{\partial \mathrm{R_g}}{\partial \mathrm{u'_g}} \frac{\partial \mathrm{u'_g}}{\partial \mathrm{\nabla p}} + \frac{\partial \mathrm{R_g}}{\partial \mathrm{u'_l}} \frac{\partial \mathrm{u'_l}}{\partial \mathrm{\nabla p}} + \frac{\partial \mathrm{R_g}}{\partial \mathrm{\nabla p}} = 0 \tag{8-16}$$

$$\left.\frac{\mathrm{dR_l}}{\mathrm{d\nabla p}}\right|_{\mathrm{ds'_l=0}} = \frac{\partial \mathrm{R_l}}{\partial \mathrm{u'_g}} \frac{\partial \mathrm{u'_g}}{\partial \mathrm{\nabla p}} + \frac{\partial \mathrm{R_l}}{\partial \mathrm{u'_l}} \frac{\partial \mathrm{u'_l}}{\partial \mathrm{\nabla p}} + \frac{\partial \mathrm{R_l}}{\partial \mathrm{\nabla p}} = 0 \tag{8-17}$$

At this point it must be recalled, that $\frac{\partial R_g}{\partial u'_g}$, $\frac{\partial R_l}{\partial u'_g}$, $\frac{\partial R_g}{\partial u'_l}$ and $\frac{\partial R_l}{\partial u'_l}$ have already been calculated in the frame of the iterative resolution of the momentum equations. Further, one can calculate $\frac{\partial R_g}{\partial \nabla p}$, $\frac{\partial R_l}{\partial \nabla p}$, $\frac{\partial R_g}{\partial s'_l}$ and $\frac{\partial R_l}{\partial s'_l}$ by finite differences, similarly to equations (4-35) to (4-40).

Afterwards, one can solve

(8-14) to (8-17) for the partial derivatives of the velocities with respect to saturation and pressure difference:

$$\left.\frac{\mathrm{du'_g}}{\mathrm{d\nabla p}}\right|_{\mathrm{ds'_l=0}} = \frac{\frac{\partial \mathrm{R_l}}{\partial \mathrm{\nabla p}} \frac{\partial \mathrm{R_g}}{\partial \mathrm{u'_l}} - \frac{\partial \mathrm{R_g}}{\partial \mathrm{\nabla p}} \frac{\partial \mathrm{R_l}}{\partial \mathrm{u'_l}}}{\frac{\partial \mathrm{R_g}}{\partial \mathrm{u'_g}} \frac{\partial \mathrm{R_l}}{\partial \mathrm{u'_l}} - \frac{\partial \mathrm{R_g}}{\partial \mathrm{u'_l}} \frac{\partial \mathrm{R_l}}{\partial \mathrm{u'_g}}} \tag{8-18}$$

$$\left.\frac{\mathrm{du'_l}}{\mathrm{d\nabla p}}\right|_{\mathrm{ds'_l=0}} = \frac{\frac{\partial \mathrm{R_g}}{\partial \mathrm{\nabla p}} \frac{\partial \mathrm{R_l}}{\partial \mathrm{u'_g}} - \frac{\partial \mathrm{R_l}}{\partial \mathrm{\nabla p}} \frac{\partial \mathrm{R_g}}{\partial \mathrm{u'_g}}}{\frac{\partial \mathrm{R_g}}{\partial \mathrm{u'_g}} \frac{\partial \mathrm{R_l}}{\partial \mathrm{u'_l}} - \frac{\partial \mathrm{R_g}}{\partial \mathrm{u'_l}} \frac{\partial \mathrm{R_l}}{\partial \mathrm{u'_g}}} \tag{8-19}$$

$$\left.\frac{\mathrm{du'_g}}{\mathrm{ds'_l}}\right|_{\mathrm{d\nabla p=0}} = \frac{\frac{\partial \mathrm{R_l}}{\partial \mathrm{s'_l}}\frac{\partial \mathrm{R_g}}{\partial \mathrm{u'_l}} - \frac{\partial \mathrm{R_g}}{\partial \mathrm{s'_l}}\frac{\partial \mathrm{R_l}}{\partial \mathrm{u'_l}}}{\frac{\partial \mathrm{R_g}}{\partial \mathrm{u'_g}}\frac{\partial \mathrm{R_l}}{\partial \mathrm{u'_l}} - \frac{\partial \mathrm{R_g}}{\partial \mathrm{u'_l}}\frac{\partial \mathrm{R_l}}{\partial \mathrm{u'_g}}} \tag{8-20}$$

$$\left.\frac{\mathrm{du'_l}}{\mathrm{ds'_l}}\right|_{\mathrm{d\nabla p=0}} = \frac{\frac{\partial \mathrm{R_g}}{\partial \mathrm{s'_l}}\frac{\partial \mathrm{R_l}}{\partial \mathrm{u'_g}} - \frac{\partial \mathrm{R_l}}{\partial \mathrm{s'_l}}\frac{\partial \mathrm{R_g}}{\partial \mathrm{u'_g}}}{\frac{\partial \mathrm{R_g}}{\partial \mathrm{u'_g}}\frac{\partial \mathrm{R_l}}{\partial \mathrm{u'_l}} - \frac{\partial \mathrm{R_g}}{\partial \mathrm{u'_l}}\frac{\partial \mathrm{R_l}}{\partial \mathrm{u'_g}}} \tag{8-21}$$

The partial derivatives of the gas velocity in the dry sub-cell *up*, u''_g and of the quench front velocity u_{QF} with respect to saturation s'_l and pressure difference ∇p are also needed. Recalling that u''_g and u_{QF} can be calculated from known values of u'_g and u'_l, they can be expressed as follows:

$$\mathrm{u''_g} = \mathrm{u''_g}(\nabla \mathrm{p}, \mathrm{s'_l}, \mathrm{u'_g}(\nabla \mathrm{p}, \mathrm{s'_l}), \mathrm{u'_l}(\nabla \mathrm{p}, \mathrm{s'_l})) \tag{8-22}$$

$$\mathrm{u_{QF}} = \mathrm{u_{QF}}(\nabla \mathrm{p}, \mathrm{s'_l}, \mathrm{u'_g}(\nabla \mathrm{p}, \mathrm{s'_l}), \mathrm{u'_l}(\nabla \mathrm{p}, \mathrm{s'_l})) \tag{8-23}$$

Then, applying the chain rule again, the partial derivatives are calculated as

$$\left.\frac{\mathrm{du''_g}}{\mathrm{ds'_l}}\right|_{\mathrm{d\nabla p=0}} = \frac{\partial \mathrm{u''_g}}{\partial \mathrm{u'_g}}\frac{\partial \mathrm{u'_g}}{\partial \mathrm{s'_l}} + \frac{\partial \mathrm{u''_g}}{\partial \mathrm{u'_l}}\frac{\partial \mathrm{u'_l}}{\partial \mathrm{s'_l}} + \frac{\partial \mathrm{u''_g}}{\partial \mathrm{s'_l}} \tag{8-24}$$

$$\left.\frac{\mathrm{du''_g}}{\mathrm{d\nabla p}}\right|_{\mathrm{ds'_l=0}} = \frac{\partial \mathrm{u''_g}}{\partial \mathrm{u'_g}}\frac{\partial \mathrm{u'_g}}{\partial \nabla \mathrm{p}} + \frac{\partial \mathrm{u''_g}}{\partial \mathrm{u'_l}}\frac{\partial \mathrm{u'_l}}{\partial \nabla \mathrm{p}} + \frac{\partial \mathrm{u''_g}}{\partial \nabla \mathrm{p}} \tag{8-25}$$

$$\left.\frac{\mathrm{du_{QF}}}{\mathrm{ds'_l}}\right|_{\mathrm{d\nabla p=0}} = \frac{\partial \mathrm{u_{QF}}}{\partial \mathrm{u'_g}}\frac{\partial \mathrm{u'_g}}{\partial \mathrm{s'_l}} + \frac{\partial \mathrm{u_{QF}}}{\partial \mathrm{u'_l}}\frac{\partial \mathrm{u'_l}}{\partial \mathrm{s'_l}} + \frac{\partial \mathrm{u_{QF}}}{\partial \mathrm{s'_l}} \tag{8-26}$$

$$\left.\frac{\mathrm{du_{QF}}}{\mathrm{d\nabla p}}\right|_{\mathrm{ds'_l=0}} = \frac{\partial \mathrm{u_{QF}}}{\partial \mathrm{u'_g}}\frac{\partial \mathrm{u'_g}}{\partial \nabla \mathrm{p}} + \frac{\partial \mathrm{u_{QF}}}{\partial \mathrm{u'_l}}\frac{\partial \mathrm{u'_l}}{\partial \nabla \mathrm{p}} + \frac{\partial \mathrm{u_{QF}}}{\partial \nabla \mathrm{p}} \tag{8-27}$$

The partial derivatives $\frac{\partial u'_g}{\partial s'_l}$, $\frac{\partial u'_g}{\partial \nabla p}$, $\frac{\partial u'_l}{\partial s'_l}$ and $\frac{\partial u'_l}{\partial \nabla p}$ are given by (8-18) to (8-21) above. The further partial derivatives on the right hand sides of (8-24) to (8-27), $\frac{\partial u''_g}{\partial u'_g}$, $\frac{\partial u''_g}{\partial u'_l}$, $\frac{\partial u''_g}{\partial s'_l}$ and $\frac{\partial u''_g}{\partial \nabla p}$ as well as $\frac{\partial u_{QF}}{\partial u'_g}$, $\frac{\partial u_{QF}}{\partial u'_l}$, $\frac{\partial u_{QF}}{\partial s'_l}$ and $\frac{\partial u_{QF}}{\partial \nabla p}$, can be calculated alongside with the partial derivatives of R_g and R_l by finite differences.